Title
Ferrosomes: Iron Storage Organelles Found in Diverse Anaerobic Bacteria

Author
Grant, Carly Rae

Publication Date
2019

Peer reviewed|Thesis/dissertation

Ferrosomes: Iron Storage Organelles Found in Diverse Anaerobic Bacteria

By

Carly Rae Grant

A dissertation submitted in partial satisfaction of the

requirements for the degree of

Doctor of Philosophy

in

Microbiology

in the

Graduate Division

of the

University of California, Berkeley

Committee in charge:

Professor Arash Komeili, Chair
Professor John D. Coates
Professor David F. Savage
Professor Gloria A. Brar

Spring 2019

Abstract

Ferrosomes: Iron Storage Organelles Found in Diverse Anaerobic Bacteria

by

Carly Rae Grant

Doctor of Philosophy in Microbiology

University of California, Berkeley

Professor Arash Komeili, Chair

Though small in size, there is a growing appreciation for the complex ultrastructure of bacteria and archaea. This complexity and beauty is exemplified by the diverse protein- and lipid-bounded organelles that have been discovered. The first chapter of this dissertation, a published review article, introduces different lipid-bounded organelles that have been found in bacteria and archaea. The best-studied lipid-bounded organelles in bacteria are the magnetosomes of magnetotactic bacteria. This chapter discusses, in depth, the mechanism of magnetosome formation in two *Magnetospirillum* spp. that make cubooctahedral-shaped magnetite crystals within the magnetosome lumen. This chapter also discusses what is known about other, more mysterious, organelles, including bullet-shaped magnetosomes, anammoxosomes, and nucleus-like organelles in archaea.

Tools for genome editing are a major limiting factor when attempting to elucidate the structure and function of organelles. As such, there are few model systems for studying organelle formation. The second chapter of this dissertation, a published primary research article, describes a method for genome editing in *Desulfovibrio magneticus* RS-1. This work is the first example of gene editing for an anaerobic bacterium that makes bullet-shaped magnetosomes and marks a major step in magnetosome research.

In addition to making magnetosomes, *D. magneticus* makes ferrosomes, which are membrane-bounded organelles that contain iron, oxygen, and phosphorus. Ferrosomes were discovered serendipitously when former Komeili lab postdoctoral scholar, Dr. Meghan Byrne, observed that *D. magneticus* cells transitioning out of iron starvation are full of electron-dense granules, now named ferrosomes. The third chapter of this dissertation uncovers the genetic basis of ferrosomes. Using the genetic method we developed for *D. magneticus*, we show that ferrosomes require a set of genes that encode proteins associated with isolated ferrosomes. In addition to *D. magneticus*, diverse bacteria, and perhaps archaea, require a similar set of genes to make ferrosomes. Finally, we show that ferrosomes likely have an important role in iron homeostasis during anaerobic metabolism. Future research on bullet-shaped magnetosomes and ferrosome formation, function, and regulation are introduced in the final chapter of this dissertation.

TABLE OF CONTENTS

Chapter 1

Organelle Formation in Bacteria and Archaea

Carly R. Grant, Juan Wan, and Arash Komeili

Department of Plant and Microbial Biology
University of California, Berkeley

The work presented in this chapter is a slightly modified version from that published in *Annual Reviews of Cell & Developmental Biology* (2018).

ABSTRACT
Uncovering the mechanisms that underlie the biogenesis and maintenance of eukaryotic organelles is a vibrant and essential area of biological research. In comparison, little attention has been paid to the process of compartmentalization in bacteria and archaea. This lack of attention is in part due to the common misconception that organelles are a unique evolutionary invention of the “complex” eukaryotic cell and are absent from the “primitive” bacterial and archaeal cells. Comparisons across the tree of life are further complicated by the nebulous criteria used to designate subcellular structures as organelles. Here, with the aid of a unified definition of a membrane-bounded organelle, we present some of the recent findings in the study of lipid-bounded organelles in bacteria and archaea.

INTRODUCTION
Membrane-bounded organelles, tasked with the compartmentalization of biochemical reactions, are one of the hallmarks of the eukaryotic cell plan. By extension, most cell biologists would argue that such subcellular organelles are absent from the architecturally simple cells of bacteria and archaea. Stanier & van Niel (1962) formalized this cytological classification system in their seminal and elegantly written work, “The Concept of a Bacterium,” which laid out several criteria for distinguishing bacteria from other microscopic entities, such as viruses and eukaryotic algae. Key among their arguments was that:

> Within the enclosing cytoplasmic membrane of the eucaryotic cell, certain smaller structures, which house subunits of cellular function are themselves surrounded by individual membranes, interposing a barrier between them and other internal regions of the cell. In the prokaryotic cell, there is no equivalent structural separation of major subunits of cellular function; the cytoplasmic membrane itself is the only major bounding element which can be structurally defined.

Stanier & van Niel were, rather specifically, referring to major eukaryotic organelles such as the nucleus, mitochondria, and chloroplasts. In the intervening years, their definition has been extended to include all organelles as unique inventions that supported the emergence of the complex eukaryotic cell and, eventually, multicellular organisms. In this review, we present a challenge to this widely held view of cellular evolution and revisit the possibility that bacteria and archaea also contain membrane-bounded organelles. To do this, we must first ask: What exactly is an organelle?

Organelles can be, and have been, defined in many different ways. Commonly, microscopy has been used to define large macromolecular structures as organelles. Additionally, functional and mechanistic studies have grouped organelles on the basis of the common molecular machinery needed for their biogenesis and maintenance. As a result, many functionally and structurally distinct structures have been classified as organelles over the years. These include membraneless entities such as lipid droplets and ribosomes; organelles acquired through ancient symbiotic events such as

mitochondria and chloroplasts; and the canonical lipid-bounded organelles of the endomembrane system such as the nucleus, the endoplasmic reticulum, and the Golgi apparatus. If applied to bacteria, similarly expansive criteria would reveal numerous examples of unique compartments that have been studied for more than a century. For instance, in a series of groundbreaking studies in the 1880s, Sergei Winogradsky showed that subcellular compartments of *Beggiatoa* are key routes for storage and transformation of sulfur compounds (2, 3). His experiments, carried out by observing the subcellular changes in uncultured bacteria kept alive for days under simple microscopes, would resonate with any modern cell biologist. In addition to these sulfur globules, many bacteria contain protein-bounded compartments, such as carboxysomes and encapsulins, as well as lipid-bounded compartments, such as the varieties of photosynthetic membrane systems found in diverse bacterial phyla (4–8).

The vast majority of these compartments do not have analogs in the eukaryotic world. As such, it may be argued that bacteria and archaea do not have eukaryotic organelles. This biased interpretation of cellular compartmentalization creates an artificial barrier that prevents meaningful comparisons of organelles across the domains of life. Thus, for the purposes of this review, we define an organelle as any subcellular membrane-bounded structure with a defined protein content that provides a unique environment for execution and sequestration of biochemical reactions. More specifically, we focus on compartments that are bounded by a lipid bilayer membrane, since a coherent set of mechanisms defines their formation in eukaryotes. This broader definition imposes a set of mechanistic challenges for the formation of an organelle in any cell type. To construct a defined lipid-enclosed compartment, cells must be able to deform and shape cellular membranes, target proteins to these compartments, and segregate them to ensure inheritance of important activities to their progeny.

With this new and more flexible concept of an organelle in hand, we present some of the latest advances in the study of lipid-bounded organelles in bacteria and archaea. We focus primarily on the magnetosome, a bacterial organelle studied extensively at the molecular level in recent years. In addition, we describe several other exotic lipid-bounded organelles that highlight the complexity of the bacterial and archaeal cell plans and blur the lines of the prokaryotic-eukaryotic divide. We hope to spark the imagination of scientists, young and old, to look to the bacterial and archaeal world for exciting new challenges in studying the mechanisms and evolution of subcellular compartmentalization.

THE MAGNETOSOME: A LIPID-BOUNDED BACTERIAL ORGANELLE

The magnetosomes of magnetotactic bacteria (MTB) are the best-studied examples of lipid-bounded organelles in bacteria (9). These diverse organisms are unified by their ability to align in and navigate along magnetic fields (10, 11). A chain of magnetic particles, ranging in size from 50 to 120 nm and consisting of the iron oxide mineral magnetite Fe_3O_4 and/or the iron sulfide mineral greigite Fe_3S_4, mediates the interaction of MTB with magnetic fields. Species of MTB can be found in nearly any aquatic

environment where they localize in or at the borders of anoxic habitats (12). In most locations, the earth's magnetic field provides a reliable path through the vertically stratified oxygen gradient. As a result, MTB are thought to combine alignment with the earth's magnetic field with aerotaxis to find zones with favorable oxygen and redox concentrations. Magneto-aerotaxis, in its most idealized form, turns the biased random three-dimensional tactic behavior of non-MTB into a more efficient one-dimensional search strategy (13).

The first cultured MTB were microaerophilic α-Proteobacteria, which have served as model organisms for understanding magnetosome formation (14–16). Early electron microscopy images of these MTB showed that a lipid-like membrane surrounds each magnetic particle in the chain (Figure 1a,b). As a result, the combined unit of the membrane and its enclosed mineral was termed a magnetosome (17). The magnetosome membrane was hypothesized to be the site of biomineralization since empty membranes as well as those with various size minerals were observed in individual cells (18). Definitive proof for the role of the membrane came through studies in which *Magnetospirillum magneticum* strain AMB-1 (hereafter AMB-1) cells grown in iron-limited conditions were imaged by electron microscopy (19). In these cells, chains of empty magnetosome membranes are readily observed. Within these empty magnetosomes, biomineralization is initiated soon after the addition of iron to the growth medium. High-resolution imaging of whole cells of AMB-1, as well as *Magnetospirillum gryphiswaldense* strain MSR-1 (hereafter MSR-1), under near-native conditions by cryo-electron tomography (CET), has shown that the magnetosome membrane is either continuous with or derived from the inner cell membrane (Figure 1a,b) (20, 21). Despite a lipid composition similar to that of the cell membrane, the magnetosome membrane has a unique profile of proteins, many of which are predicted to contain one or more transmembrane domains (18, 22–24). Additionally, as detailed below, a network of actin-like filaments surrounds and organizes the magnetosome chain (Figure 2) (20, 21). Thus, the lipid bilayer magnetosome membrane—with its unique protein content, associated cytoskeleton, and dedicated function in biomineralization—has all the hallmarks of an organelle.

Like all organelles, the formation and function of magnetosomes are driven by a distinct set of genes. Proteomic, genetic, and comparative genomic studies have shown that a large number of proteins encoded by conserved genes of a magnetosome gene island (MAI) control nearly every aspect of magnetosome formation (9). In AMB-1 and MSR-1 MAIs, the *mamAB* gene cluster contains the most important elements for the early steps of magnetosome biogenesis (25–27). Deletions of various *mamAB* genes result in significant defects in magnetosome membrane formation and protein sorting, chain alignment, initiation of biomineralization, and crystal maturation (26). Expression of the *mamAB* gene cluster in the absence of all other MAI genes allows for the formation of magnetosome membranes that can form immature magnetic particles (27). In addition, several other MAI gene clusters such as the *mms6*, *mamCDFG*, and *mamXYZ* operons participate in regulating the size, shape, and conditional production of magnetite in both

AMB-1 and MSR-1 (27–30). In a significant achievement, the Schüler group showed that approximately 35 genes of the MSR-1 MAI are sufficient to form magnetosomes in the non-MTB *Rhodospirillum rubrum*, proving that a subset of the MAI genes are necessary and sufficient for magnetosome formation (31).

Here, we focus on the most recent studies on the mechanisms of magnetosome membrane formation, protein sorting, and subcellular organization. For more detailed information on the environmental relevance and phylogenetic diversity of MTB, the mechanisms of biomineral formation, and biotechnological uses of magnetosomes, we refer the interested reader to several excellent review articles (9, 32–37).

Magnetosome Membrane Formation

The first challenge in building a magnetosome is to reshape the cell membrane into a spherical vesicle-like compartment. Comprehensive genetic analyses had implicated four genes (*mamB*, *mamI*, *mamL*, and *mamQ*) as essential factors in the biogenesis of the magnetosome membrane (26). Subsequently, more detailed CET imaging has shown that the Δ*mamB* mutant is the only strain that completely lacks magnetosome membranes, while deletions of *mamI*, *mamL*, or *mamQ* yield fewer immature magnetosomes (38). MamB, a cation transporter, performs its essential role in membrane biogenesis with the help of other magnetosome proteins. For instance, in MSR-1 the expression of 7 of the 18 genes in the *mamAB* gene cluster (*mamI*, *mamL*, *mamQ*, *mamB*, *mamE*, *mamO*, and *mamM*) is enough to induce membrane formation; however, membrane formation by this synthetic operon still requires other MAI genes, such as the *mamXYZ* operon (38). Point mutations in the gene encoding MamB that block its iron transport function prevent biomineralization but still allow for membrane formation (39). In addition, MamB forms a complex with a homologous transporter, MamM, and interacts with MamE, a protease that helps control protein sorting to magnetosomes (40–43). On the basis of these collective genetic and biochemical observations, a protein crowding model for magnetosome membrane formation has been proposed (Figure 1d). In this model, MamB interacts with a subset of proteins, such as MamM and MamE, at the inner cell membrane. These proteins then recruit other interaction partners and form a large protein complex that generates lateral pressure to induce membrane curvature (38, 44).

Dynamics of Magnetosome Membrane Growth

These studies address the genetic requirements of magnetosome membrane formation but say little about the dynamics and regulation of the process. Wild-type MTB contain magnetosome membranes at all times, making it difficult to study the dynamics of membrane formation in a synchronous natural setting. Thus, an artificial system was developed to genetically induce membrane formation in an AMB-1 mutant incapable of forming wild-type magnetosomes (45). Observations of magnetosome size in this inducible system as well as wild-type AMB-1 lead to a model in which individual magnetosomes bud from the inner cell membrane and grow gradually in size over time. Furthermore, membrane size is controlled by the biomineralization status of individual

magnetosomes: Empty magnetosome membranes are always smaller than 55 nm, while those containing magnetite crystals can grow to approximately 80 nm (45). These findings suggest that at least one checkpoint must be in place to stop membrane growth if biomineralization has not occurred. Upon initiation of mineral formation, the magnetosome membrane undergoes a second stage of growth. The utility of such a checkpoint and its universality among MTB are currently unclear. Perhaps limiting the volume of the magnetosome allows for accumulation of iron to supersaturating levels, which would promote magnetite nucleation. Under this model, premature magnetosome membrane growth or a failure to undergo a second stage expansion may lead to defects in the shape and size of the resulting mineral.

Magnetosome Protein Sorting

The protein crowding model indicates that a core complex of factors can work with interchangeable subgroups of other magnetosome proteins to promote membrane formation. By definition, then, membrane biogenesis occurs concurrently with protein sorting for these founder magnetosome proteins (Figure 1d). In addition, other magnetosome proteins may localize to the organelle after the membrane formation step. For example, Mms6, a protein that binds to magnetite and controls geometry of the resulting crystal, is diffusely localized around the cell membrane under nonbiomineralizing growth conditions in which only empty magnetosome membranes are formed (46). In contrast, correlated fluorescence microscopy and electron microscopy show that Mms6 is found only at magnetosomes that contain a magnetite particle under biomineralizing conditions (46). It has also been suggested that other proteins, such as MamY, localize to magnetosomes at select stages of biomineralization (47). These proteins may dynamically sample the entire inner cell membrane space and become trapped in magnetosomes via their interactions with the biomineral (Figure 1d). Alternatively, other factors, such as MamE and MamA, a soluble protein that interacts with the cytoplasmic face of the magnetosome membrane, may conditionally recruit proteins to magnetosomes after their formation (42, 48, 49). This selective recruitment of proteins may account for the biomineralization-dependent growth of the magnetosome membrane.

Diversity of Magnetosome Membrane Formation

AMB-1 and MSR-1 magnetosome membranes, despite their overwhelming similarities, are distinguished by one significant architectural feature. In AMB-1, magnetosome membranes are permanent invaginations of the inner cell membrane, while in MSR-1 magnetosome membranes eventually separate into distinct intracellular vesicles (Figure 1a,b) (20, 21, 38). Additionally, the biomineralization-dependent checkpoint for membrane growth in AMB-1 cells has not been seen in MSR-1 cells (38). Thus, in AMB-1, mechanisms must be in place to balance membrane growth with biomineralization, to maintain sharp angles at the neck of the magnetosome, and to prevent the intrusion of unwanted periplasmic materials into the magnetosome lumen. Meanwhile, MSR-1 cells must have a way to promote the fission of the growing magnetosome membrane to become an intracellular vesicle.

The variety of magnetosome formation processes becomes even more bewildering when more diverse species of MTB are examined. Anaerobic MTB belonging to the δ-Proteobacteria, Nitrospira, and OP3 phyla form elongated bullet-shaped magnetite or greigite crystals in an unknown process that is likely different from what occurs in the microaerophilic MSR-1 and AMB-1 (37). For instance, in the δ-Proteobacterium *Desulfovibrio magneticus* strain RS-1, mature magnetic particles do not seem to be surrounded by a lipid bilayer membrane (Figure 1c) (50). However, *D. magneticus* contains an MAI with several homologs of the AMB-1 and MSR-1 *mam* genes and many *mad* genes that are found only in the MTB in the δ-Proteobacteria and Nitrospira lineages (51). Recently, a classical chemical and UV mutagenesis approach was combined with whole-genome resequencing to find nonmagnetic mutants of *D. magneticus* (52). This genetic screen yielded mutations in *mam* and *mad* genes, indicating the participation of both conserved and group-specific genes in biomineralization. Since many of these genes encode proteins with one or more transmembrane domains, a membrane must be involved at some point during the biomineralization process. Thus, a magnetosome factory model has been proposed in which a membrane-bounded compartment produces a mineral that is subsequently released and recruited into a growing magnetosome chain (52). This sequential magnetite production and release are fundamentally different from the simultaneous mineralization in multiple magnetosome membranes that is seen in AMB-1 and MSR-1. The utility of this mode of biomineralization, its prevalence among MTB, and the specific mechanisms of biomineralization in *D. magneticus* remain to be uncovered.

Magnetosome Chain Formation

To orient the cell in geomagnetic fields, individual magnetosomes need to be assembled into a chain. In both AMB-1 and MSR-1, chain alignment is achieved, in part, by filaments that most likely consist of MamK, a homolog of the bacterial actin-like protein MreB (53, 54). MamK is expressed from and conserved in the *mamAB* gene cluster of all MTB, and its deletion results in the disappearance of the magnetosome-associated filaments and in noticeable disorganization of the magnetosome chain. In Δ*mamK* mutants of AMB-1, large gaps separate clusters of magnetosomes that are loosely organized across the long axis of the cell (Figure 2a) (20). Similarly, when *mamK* is deleted in MSR-1, the magnetosome chains are shorter, fragmented, and located randomly along the entire length of the cell (53, 55). Similar to other actin-like proteins, purified MamK is capable of forming filaments in the presence of ATP; these filaments are dynamically depolymerized via the MamK ATPase activity (56). In a recent breakthrough, a nonpolymerizing mutant of MamK was used to obtain the protein's crystal structure, revealing a domain organization and structure for MamK monomers that are similar to those of actin and its bacterial homologs (Figure 2c) (57). However, once these monomers polymerize, the resulting filaments have a unique architecture distinct from that of eukaryotic actin and its bacterial relatives (Figure 2d) (56–58).

Recent studies have elucidated a conserved role for MamK in coordinating the even segregation of the magnetosome chain during cell division. In MSR-1, the magnetosome

chain is centered within the cell but does not run from pole-to-pole. During cell division, the magnetosome chain splits down the middle, and the segregated chains are positioned asymmetrically at newly formed poles of daughter cells (55). The newly segregated chains undergo a rapid pole-to-midcell repositioning in the daughter cells before the completion of cytokinesis (59). FRAP (fluorescence recovery after photobleaching) assays indicate that new MamK monomers enter the filaments at cell poles and undergo treadmilling growth in an ATPase-dependent manner. When an ATPase-dead version of MamK is introduced into Δ*mamK* cells, magnetosome chains are inherited unevenly by the two daughter cells, and no pole-to-midcell repositioning is observed (Figure 2b) (59).

In contrast to the case for MSR-1, magnetosome chains of AMB-1 are organized from pole-to-pole in the cell. As a result, after cell division the daughter cells inherit chains that run the entire length of the cell and, as a result, do not need to be centered to midcell. In the early time points of the inducible experiments described above, several short clusters of magnetosomes that are separated by large gaps are formed. These clusters are still aligned across the length of the cell independently of the presence of MamK. At later time points, MamK filaments are needed to either repair or fill these gaps to form a continuous chain (45). The dynamic movements of magnetosomes have also been tracked using fluorescently tagged magnetosome proteins as markers. In wild-type AMB-1 cells, the magnetosome chain is static throughout the cell cycle (60). However, in the Δ*mamK* mutant, magnetosomes are highly dynamic, and the fluorescent protein markers form foci that move randomly throughout the cell at a rate that is consistent with simple diffusion of a large macromolecular complex (60). Wild-type MamK, but not the ATPase-dead variant, is able to restore the static pole-to-pole arrangement of the magnetosome chain. These results support a model in which newly formed magnetosomes can move around the long axis of the cell until they are captured by the MamK filament network into a chain. MamK then restricts the movement of magnetosomes and ensures their stable positioning for even segregation to daughter cells during cytokinesis. Thus, through two seemingly different mechanisms, MamK controls the positioning of the magnetosome chain in AMB-1 and MSR-1.

In addition to MamK, other proteins have been linked to chain alignment. The loss of MamJ, an acidic magnetosome membrane protein, results in collapse of the chain structure and in dramatic clumping of magnetosomes in MSR-1 (21). The AMB-1 MAI contains *mamJ* as well as a homologous gene, *limJ* (like *mamJ*), that have a redundant function in maintaining MamK filament dynamics. In contrast to MSR-1, the magnetosome chains of the AMB-1 Δ*mamJ*Δ*limJ* mutant retain their long-range chain alignment, and a few large gaps lacking magnetosomes, filled with bundles of filaments presumed to be MamK, appear in the chain (61). Yeast two-hybrid experiments suggest that MamJ interacts with MamK filaments and may recruit them to magnetosomes (62). These observations invoke a model in which MamJ links magnetosomes to MamK filaments. Then, natural treadmilling of MamK filaments drives the magnetosomes toward the center of the cell and ensures even segregation of the chain upon cell division (59).

AMB-1, but not MSR-1, also contains a second highly degenerate magnetosome gene island that may have been acquired through a horizontal gene transfer event. This so-called magnetosome islet contains homologs of *mamK* (*mamK-like*) and *mamJ* (*mamJ-like*) (63). MamK-like retains many of the properties of MamK, including the ability to bind nucleotides and form filaments *in vitro* and *in vivo* (63). MamK and MamK-like also interact and most likely form mixed filaments consisting of both proteins (64). Interestingly, MamK-like has a mutation that should block ATPase activity and slow down the dynamic turnover of mixed MamK–MamK-like filaments *in vivo*. However, MamK-like, even with its active site mutated, is able to hydrolyze ATP *in vitro* and control MamK dynamics *in vivo* (64). The structural basis for the unexpected enzymatic activity of MamK-like remains to be determined. Regardless, these findings raise the possibility that in some MTB the acquisition of the magnetosome islet, or duplications of genes like *mamK* and *mamJ*, may result in divergent behaviors for MamK and other magnetosome proteins. Accordingly, a few other MTB also contain more than one MamK homolog. MamK is also found in many non-MTB and some species of archaea in which its function remains a mystery.

The control of organelle positioning via MamK is reminiscent of the participation of cytoskeletal proteins in the movement and segregation of membrane-bounded organelles in eukaryotes. This conserved traffic function most likely reflects a case of convergent evolution in which the ATPase-driven dynamics and long-range reach of a filament-forming protein can be adapted to the movement and positioning of diverse cargo in eukaryotes, bacteria, and perhaps archaea.

EXOTIC BACTERIAL ORGANELLES

As a whole, the magnetosome formation process bears little mechanistic or functional similarity to the eukaryotic endomembrane system. In the following sections, we feature several unusual bacterial lipid-bounded organelles that reside in relative obscurity and, yet, may hold potential ancestral links to eukaryotic organelles.

The Planctomycetes: Compartmentalized or Not?

Planctomycetes, a group of bacteria comprising a deep-branching phylum, were long thought to have a cell plan far different from canonical Gram-negative bacteria. Early studies indicated that Planctomycetes lacked a periplasmic space and instead had a cytoplasm divided into two distinct compartments (Figure 3a) (65). The innermost compartment contained the nucleoid and ribosomes and was named the riboplasm. The region void of ribosomes between the outer and inner membranes, referred to as the paryphoplasm, often appeared to contain vesicles. Planctomycetes are the only bacteria that encode for proteins with structural similarity to eukaryotic membrane-coat (MC) proteins. Tantalizingly, these MC-like proteins localize within the paryphoplasm and at the vesicle membranes (66). This finding, in addition to the apparent uptake of proteins into the paryphoplasm, supported an endocytosis-like uptake of macromolecules and led to the hypothesis that similar mechanisms might control membrane dynamics in eukaryotes and the Planctomycetes (67). In the special case of *Gemmata obscuriglobus*, the riboplasm appeared to be divided into an additional third compartment by a double

membrane that contained the nucleoid (65, 68). The appearance of this nuclear body as well as genomic and microscopic findings of nuclear pore–like structures raised the possibility of a common evolutionary origin with the eukaryotic nucleus (69).

These findings of Planctomycete compartmentalization were based on two-dimensional microscopy of sectioned cells. However, recent three-dimensional reconstruction and CET have revealed that all internal membranes of *G. obscuriglobus* are interconnected (66, 70, 71). Furthermore, Planctomycetes do have an outer membrane, a peptidoglycan cell wall, and an inner cytoplasmic membrane that—by virtue of housing the F_1F_0-ATPase—is likely the site of ATP synthesis (72–75). Therefore, Planctomycetes, like all Gram-negative bacteria, have a periplasm and cytoplasm divided by a cytoplasmic membrane (Figure 3a). Unlike the case for most Gram-negative bacteria, the cytoplasmic membrane of Planctomycetes can be heavily invaginated, often growing up to three times the surface area of the outer membrane (76). The purpose of the extensive cytoplasmic membrane, and the resulting large periplasmic space, remains unknown. In addition, the method for macromolecule uptake into the periplasm of Planctomycetes has yet to be elucidated, although it has been suggested that crateriform structures and pili-like fibers, and not MC-like proteins, may play a role (70). Instead, MC-like proteins may generate or stabilize the extensive endomembrane structures. While Planctomycetes may not be compartmentalized as previously thought, the extensive and dynamic cytoplasmic membrane may resemble early evolutionary steps in the development of eukaryotic organelles. Recent and future advances in genetic techniques in Planctomycetes will help to understand their unique ultrastructure (77–79).

Anammoxosome: An Energy-Conserving Bacterial Organelle

In addition to an unusual cell ultrastructure, some Planctomycetes have an organelle termed the anammoxosome within their cytoplasm (Figure 3b). The anammoxosome is the key conductor of the unique anaerobic ammonium oxidation (anammox) metabolism of some chemolithoautotrophic bacteria (80). While no anammox bacteria are in pure culture, some enrichment cultures have been established, including that of *Candidatus* Brocadia fulgida and *Candidatus* Kuenenia stuttgartiensis. The anammoxosome is a large organelle enclosed by a single lipid bilayer that occupies approximately 60% of the total cell volume (81). The anammoxosome, cytoplasmic, and outer membranes are enriched in ladderane lipids, which have a ladder-like arrangement of fused cyclobutane rings in their hydrocarbon tails (82). The unusual ladderane lipid structure is thought to decrease membrane permeability and thus limit energy loss from passive diffusion of protons during the slow anammox metabolism (83). Unlike the cytoplasmic and outer membranes, the anammoxosome membrane is highly curved. When isolated from cells, anammoxosomes lose their curved shape, suggesting that osmotic pressure or a cytoskeleton is involved in shaping the anammoxosome (Figure 3b) (83).

Why do anammox bacteria dedicate most of their cell volume to this unusual organelle? The answer lies in the unique function of the anammoxosome. Within the

anammoxosome matrix, anammox catabolism occurs via key enzymes that convert ammonium and nitrite to N_2 with nitric oxide and highly reactive hydrazine intermediates (Figure 3b) (84–86). Once hydrazine oxidation to N_2 is complete, electrons carried by cytochromes within the anammoxosome matrix may flow through an electron transport chain at the anammoxosome membrane, thereby establishing a proton-motive force (87, 88). Importantly, an F-type ATPase has been shown to localize to the anammoxosome membrane, suggesting that the organelle is the site of ATP production (89, 90). In this context, the highly curved membranes of the anammoxosome may allow for a greater number of metabolic enzymes and thus greater energy generation and conservation, analogous to the inner membranes of mitochondria in eukaryotic cells (83).

In addition to the anammox reaction proteins, many additional enzymes localize to the anammoxosome matrix (65, 84). Among these are hydrazine/hydroxylamine oxidoreductases, which may help keep inhibitory intermediates, such as nitric oxide and hydroxylamine levels, low. At least one enzyme, nitrite oxidoreductase (NXR), specifically localizes to tubule-like structures within the anammoxosome matrix (Figure 3b) (84). This localization may facilitate high local concentrations of NXR, an enzyme that may be important for both electron transport and carbon fixation (91, 92). It is thought that all of the enzymes localized in the anammoxosome are specifically targeted via signal peptides for the *sec* or *tat* translocation systems (65, 84); however, further experiments are needed to test this hypothesis.

Also within the anammoxosome matrix are electron-dense iron-containing granules that resemble encapsulins found to store iron in *Myxococcus xanthus* (Figure 3b) (81, 93). Encapsulins are nanocompartments that are formed by a linocin-like protein shell and function in oxidative stress in coordination with cargo proteins (8, 94, 95). Indeed, genomes of anammox bacteria encode for linocin-like proteins, such as Kuste2478 in *Ca.* K. stuttgartiensis. Kuste2478 has a C-terminal linocin domain; an N-terminal signal sequence that may target it out of the cell or into the anammoxosome matrix; and a diheme cytochrome *c* domain that could function in iron encapsulation together with the cargo protein Kuste2479, a hydroxylamine oxidoreductase and copper nitrite reductase fusion protein (87, 96, 97). If these proteins do form encapsulins within the anammoxosome matrix, then the iron granules observed may function as a detoxification system.

Future studies aimed at how anammoxosomes form and divide equally between daughter cells will aid in the understanding of membrane remodeling and organelle partitioning (98). In addition, only one F-type ATPase has been found to be highly expressed and localized to the anammoxosome membrane. Anammox bacteria encode other ATPases that may drive alternative metabolisms that are not possible in current enrichment cultures. Evidence for such metabolic versatility includes organic acid oxidation and respiration of both iron and manganese by anammox bacteria (86, 99). Pure cultures of anammox bacteria and the development of genetic systems will immensely aid future research efforts.

Membrane-Bounded Storage Granules: A Diversity of Organelles

Polyphosphate granules enclosed within an intracellular membrane have been found in bacteria as well as eukaryotes. In unicellular eukaryotes, polyphosphate granules were named acidocalcisomes for their acidic nature and their ability to accumulate high amounts of calcium (100, 101). Many pumps, channels, and cation exchangers are located on the acidocalcisome membrane in addition to polyphosphate-synthesizing and -degrading enzymes within the compartment (102). In bacteria, polyphosphate granules formed by *Agrobacterium tumefaciens* and *R. rubrum* are the best characterized. Both *A. tumefaciens* and *R. rubrum* typically make one larger granule (~200 nm in diameter) in addition to smaller granules in different regions of the cells (Figure 4a,b) (103, 104). These granules are acidic, with proton pyrophosphatase activity, and they may take in high amounts of calcium. Isolated *A. tumefaciens* granules have a material surrounding the granule that was presumed to be a membrane (Figure 4a), although the membrane was less visible in thin-sectioned cells (103). In *R. rubrum*, an electron-dense ring was observed surrounding the empty compartments where membrane-bound proton pyrophosphatases (H^+-PPases) localize (Figure 4b) (104). All of these features are strikingly similar to those in eukaryotic acidocalcisomes. However, despite genetic tools in both *A. tumefaciens* and *R. rubrum*, no membrane transporters or polyphosphate-synthesizing and -degrading enzymes have been shown to be directly involved in forming the bacterial acidocalcisomes. Moreover, absence of H^+-PPase expression in *R. rubrum* does not correlate with observations of acidocalcisomes under aerobic conditions (104, 105). Thus, genetic and biochemical studies are necessary to elucidate how bacterial acidocalcisomes are formed.

In addition to acidocalcisomes, smaller lipid-bounded granules have been found in some other bacterial species. Both *D. magneticus* and *Shewanella putrefaciens* form electron-dense granules that are 30–50 nm in diameter. These small granules are bound by membranes and contain high amounts of phosphorus, oxygen, and mixed-valence iron (Figure 4c,d) (50, 52, 106, 107). While *D. magneticus* forms the granules when transitioning from iron-limited to iron-replete conditions, *S. putrefaciens* forms the granules when respiring on ferrihydrite and, to a lesser extent, when respiring Fe^{3+} or fumarate supplemented with Fe^{2+}. Although *D. magneticus* and *S. putrefaciens* are phylogenetically and metabolically diverse, work from our group shows that homologous proteins, encoded by a distinct operon, control the formation and function of the iron-accumulating granules in both organisms (C.R. Grant & A. Komeili, unpublished). We have proposed to name this organelle the ferrosome and hypothesize that it is widespread among bacteria as well as some archaeal species.

ORGANELLES IN ARCHAEA

Given the growing evidence that eukaryotic cells emerged from an archaeal lineage, it may not be surprising that organelle-like features have also been described in some archaeal species. One intriguing example is that of the hyperthermophilic crenarchaeal *Ignicoccus* species. At first glance, the large, vesicle-containing periplasmic

space of these organisms, divided by the outer and innermost membranes, resembles the complex endomembrane system of the Planctomycetes (Figure 3c) (108, 109). *Ignicoccus* species also lack a cell wall. Both of these features are unique traits, as archaea typically have a single membrane and an S-layer cell wall (108, 109). *Ignicoccus hospitalis* has been the focus of much research, as this archaeon is also the host of *Nanoarchaeum equitans* (110, 111). Intriguingly, *I. hospitalis* does not have a typical energized cytoplasmic membrane. Rather, the inner membrane encloses the DNA and ribosomes, while the outer membrane houses ATP synthases and oxidoreductases for sulfur respiration (112). Thus, energy conservation is spatially separated from information processing and protein biosynthesis. In addition, some ATP-consuming pathways, such as that of acetyl-CoA synthesis, are located in the intermembrane compartment, indicating that it may be the site of CO_2 fixation (113). How do ATP and other substrates enter the cytoplasm for the energy-consuming and essential processes of DNA replication, transcription, and translation? How do proteins, synthesized in the cytoplasm, localize to the outer membrane? It has recently been shown that cytoplasmic protrusions, initially thought to be membrane vesicles, come into close contact with the outer membrane (Figure 3c) (114). At this interface, docking sites and eukaryotic-like tethering complexes may assist in the transfer of proteins to the outer membrane and ATP to the inner membrane, while a matrix of filaments may support the dynamic inner cytoplasmic membrane (112, 114). In addition to these focused studies of *Ignicoccus*, metagenomic analyses have identified the Asgard archaea, an uncultivated group of organisms with an unusually close phylogenetic association with the eukaryotes. The genomes of these archaea encode numerous proteins that are homologous to eukaryotic membrane trafficking components (115). It would be fascinating to isolate and image the subcellular organization of the Asgard archaea. Perhaps we will discover a cell plan with intimate similarities to that of eukaryotic cells.

CONCLUSION

In this review, we present a missing perspective in cell biology: that lipid-bounded organelles are not limited to eukaryotes and are an important component of many bacterial and archaeal lifestyles. At a fundamental level, the discovery and study of bacterial and archaeal organelles mirror the practices established through decades of work on eukaryotic cells. For instance, all organelles described in this review, from magnetosomes to the sulfur globules studied by Winogradsky, were first discovered through microscopy-based approaches. However, several distinct challenges impede the study of bacterial and archaeal organelles. First, these organisms are small, and their organelles are even smaller. We predict that many bacterial cells contain organelles, such as the ferrosomes, that have been generally ignored since they are difficult to visualize with traditional electron microscopy techniques. Broader adoption of high-resolution electron microscopy, such as whole-cell CET, and super-resolution fluorescence microscopy techniques is likely to accelerate the discovery and full exploration of these compartments. Indeed, recent imaging by CET has shown that diverse bacterial species contain many unidentified structures, some of which bear the cytological hallmarks of membrane-bounded organelles (116). Second, many interesting bacterial and archaeal

organelles are found in either uncultured organisms or those that are difficult to manipulate genetically. For instance, *Candidatus* Ovobacter propellens is a unique bacterium, with its DNA-containing cytoplasm surrounding a large central vacuole (117). Even more fascinating are the hundreds of flagella rooted in a groove on one side of the cell under which are rectangular-shaped organelles made up of stacked membranes. Are these organelles coordinating motions of its flagella with external stimuli or, perhaps, generating the localized pockets of energy needed to achieve the high-speed movement of the organism? More focused efforts to cultivate microbes and develop molecular genetic tools would be a significant boost in understanding the mechanisms of compartmentalization in diverse organisms. A final, and perhaps most significant, challenge is the far-too-prevalent view that compartments of bacteria and archaea are not true organelles. Presenting bacterial and archaeal compartments as organelles is likely to attract a more diverse cohort of scientists and to divert research power to the development of tools for the study of cellular biology in small bacterial cells. As a result, we may begin to uncover evolutionary ancestors of the proteins that establish and maintain the eukaryotic endomembrane system. We may also discover new modes of cell regulation and novel physiological pathways used by bacteria and archaea. Finally, by leveraging the simplicity of bacterial and archaeal organelles and their unique products, we may be able to devise powerful biomedical applications. A glimpse of this promising future can be seen in the recent use of magnetotactic bacteria for hyperthermic treatment of cancers and targeted drug delivery to tumors in animal models (32, 118). Bacterial and archaeal model systems are normally coveted for their simplicity. The time has come to investigate, and celebrate, the mysteries of their complex cell plans.

FIGURES

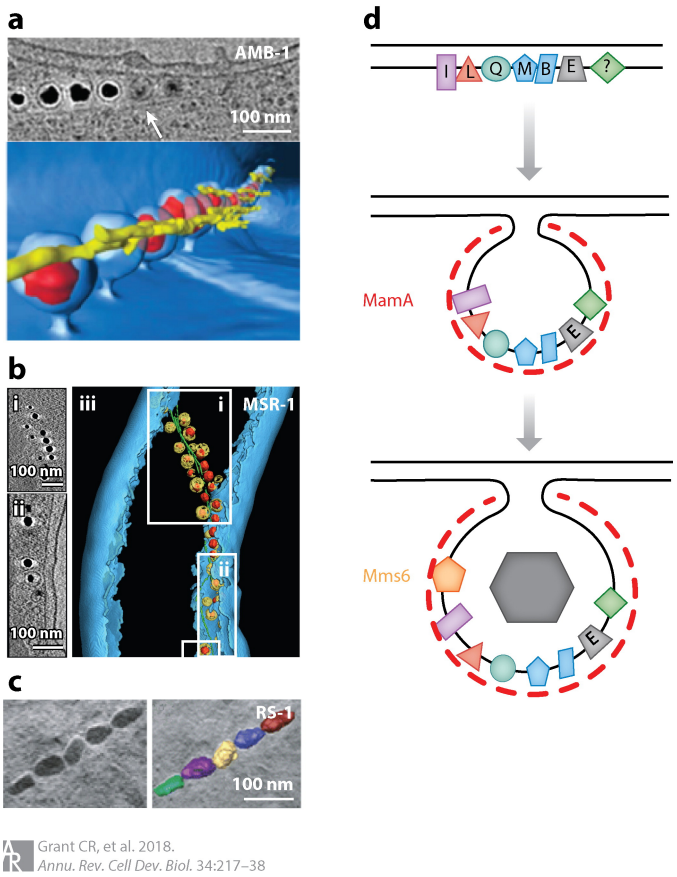

Figure 1. Single tomograms and three-dimensional models show the magnetosome chains in (*a*) AMB-1 (*b*) MSR-1, and (*c*) *Desulfovibrio magneticus* RS-1. (*a,b*) In AMB-1, most magnetosomes are continuous with the cell membrane, whereas in MSR-1 most magnetosomes are separated. The crystals in AMB-1 and MSR-1 are colored in red. The filaments in AMB-1 and MSR-1 are colored in yellow and green, respectively. The arrow in panel *a* points to the magnetosome-associated filaments. (*b*) Subpanels *I* and *ii* are tomographic sections corresponding to the white-boxed portions of the three-dimensional model of magnetosomes in subpanel *iii*. Panel *a* reproduced from Komeili et al. (2006) with permission from the American Association for the Advancement of Science. Panel *b* adapted from Raschdorf et al. (2016) with permission from the Public Library of Science. (*c*) The mature magnetite crystals of *D. mangeticus* RS-1 are not surrounded by a membrane. Panel *c* reproduced from Rahn-Lee et al. (2015) with permission from the Public Library of Science. (*d*) Model for membrane formation and protein sorting. MamB forms a complex with MamM and MamE, which may help to recruit other proteins (*green diamond*). This complex of core proteins induces membrane formation by a proposed protein crowding model. The soluble protein MamA (*red dashes*) interacts with the cytoplasmic face of the magnetosome membranes after their formation and the initiation of biomineralization.

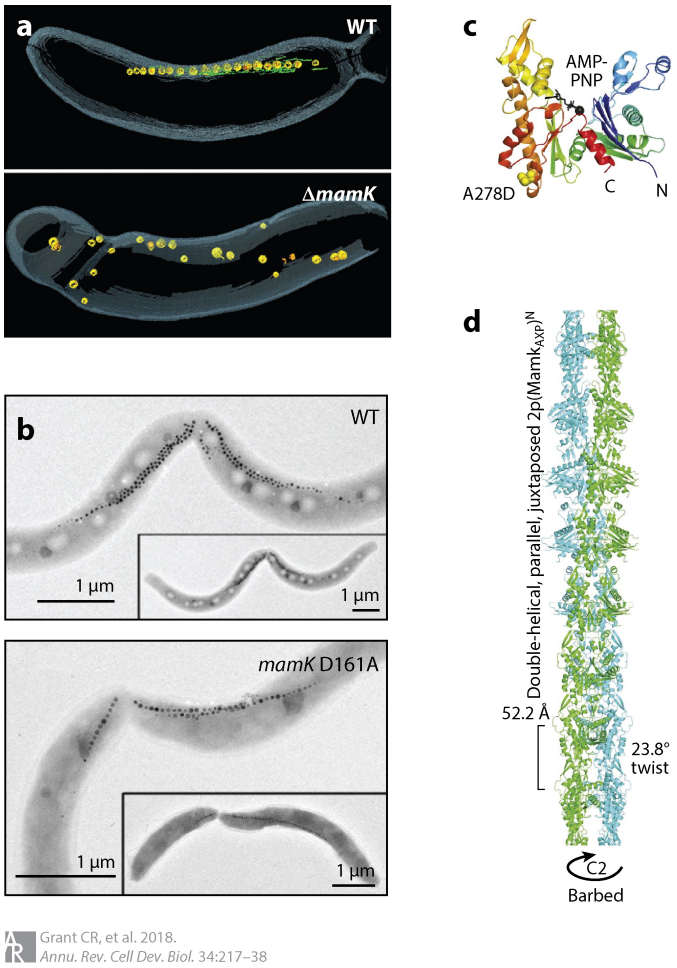

Figure 2. Magnetosome chain organization. (a) Electron cryotomography–generated three-dimensional models of AMB-1 wild-type (WT) and mamK deletion strains. Filaments (green) flank the magnetosome chain (yellow) in WT. The filaments are absent and the magnetosomes are disorganized in the mamK mutant. Panel a reproduced from Komeili et al. (2006) with permission from the American Association for the Advancement of Science. (b) TEM images show the distribution of the magnetosome chain during cell division in MSR-1 WT and mamK ATPase dead mutation (D161A) strains. Panel b reproduced from Toro-Nahuelpan et al. (2016) with permission from the BioMed Central (United Kingdom). (c) Crystal structure of a nonpolymerizing AMB-1 MamK mutant protein (A278D) at 1.8-A˚ resolution. The cocrystallized AMP-PNP nucleotide is shown in black, and the protein is colored indigo to red, like a rainbow, from the N terminus to the C terminus. (d) Refined atomic model of the MamK filament. Unlike most actin-like proteins, MamK monomers in neighboring strands are in register with each other, creating an additional C2 symmetry axis along the filament axis. Panels c and d reproduced from Löwe et al. (2016) with permission from the US National Academy of Sciences.

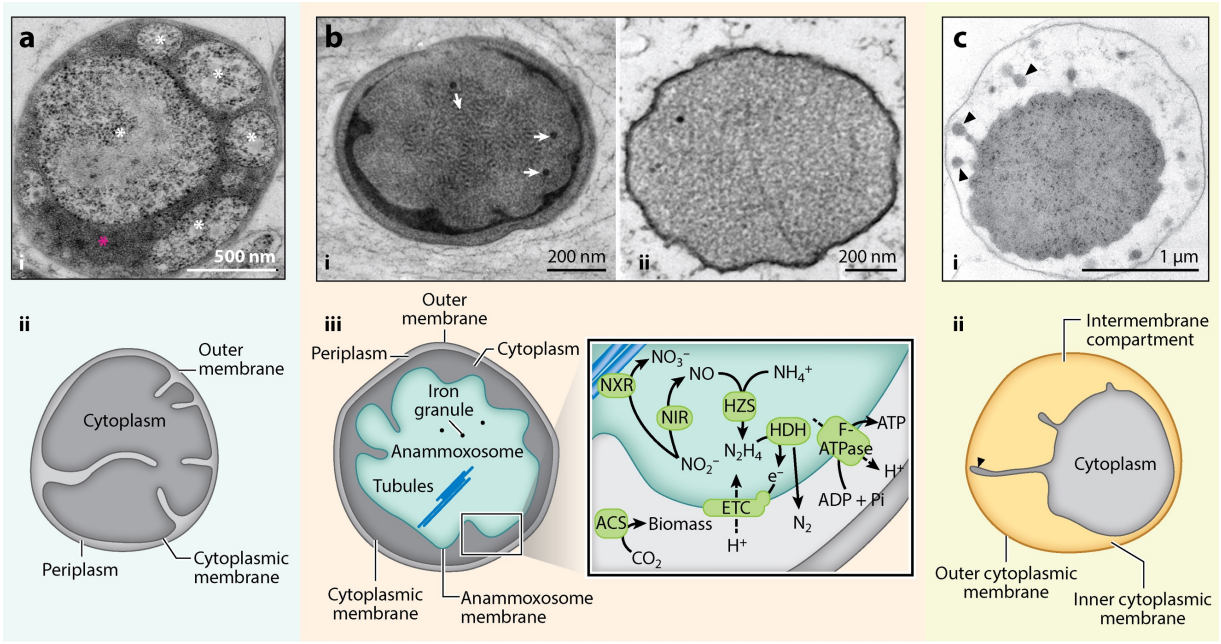

Grant CR, et al. 2018.
Annu. Rev. Cell Dev. Biol. 34:217–38

Figure 3. Organelles in Planctomycetes and Crenarchaeota. (a) (i) Highly invaginated cell membranes of *Gemmata obscuriglobus* and other Planctomycetes create a periplasm (pink asterisk) and cytoplasm (white asterisks) that appear as compartments and vesicles in two-dimensional cross sections. Electron micrograph from Santarella-Mellwig et al. (2010) and reproduced with permission from the Public Library of Science. (ii) Schematic of the Planctomycetes cell plan depicts cell membrane invaginations reaching into the cytoplasm. (b) (i) The anammoxosome, containing tubules and iron granules (white arrows), is visible by electron microscopy in *Candidatus* Brocadia fulgida cells. Image from van Niftrik et al. (2008b) and reproduced with permission from Elsevier. (ii) Isolated anammoxosomes from *Candidatus* Kuenenia stuttgartiensis lose their highly curved shape. Image from Neumann et al. (2014) and reproduced with permission from John Wiley and Sons. (iii) The anammoxosome houses the anammox reaction, which proceeds by three main steps (inset): nitrite reduction to nitric oxide by nitrite reductase (NIR), hydrazine production from nitric oxide and ammonium by hydrazine synthase (HZS), and hydrazine oxidation by hydrazine dehydrogenase (HDH). The electrons released from the anammox reaction flow through an electron transport chain (ETC), which creates a proton-motive force and drives ATP synthesis. Nitrite oxidation by nitrite oxidoreductase (NXR) may be coupled to nitrite oxidation to nitric oxide by NIR or may generate reducing equivalents for CO2 fixation by acetyl-CoA synthetase (ACS). (c) (i) Electron micrograph of Ignicoccus hospitalis shows two clearly distinguished compartments with vesicle-like structures (black carets) in the outermost compartment. Subpanel i image from National Academy of Sciences (2008), copyright 2008, National Academy of Sciences. (ii) The schematic of the Ignicoccus cell plan shows cytoplasmic protrusions extending toward the outer cytoplasmic membrane that are observed as vesicles in two-dimensional cross sections of cells.

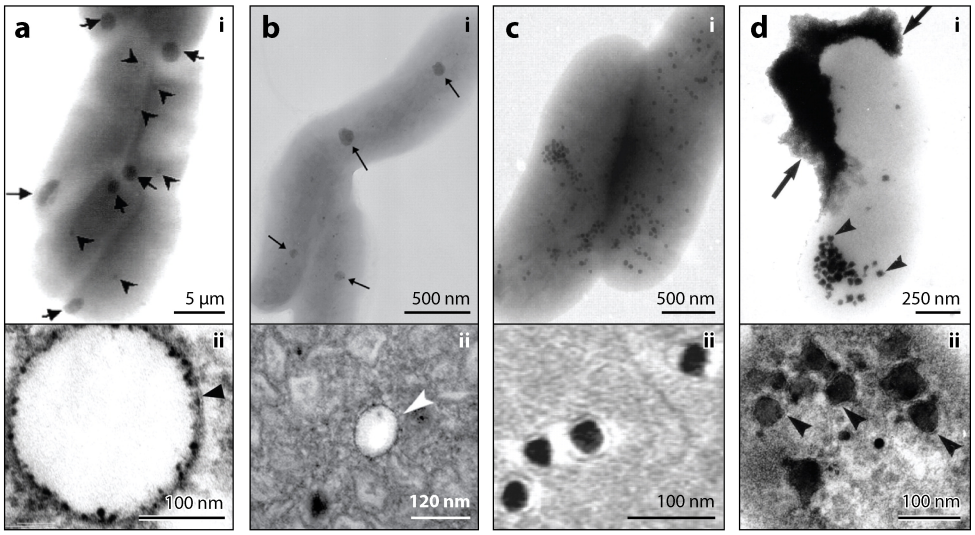

Grant CR, et al. 2018.
Annu. Rev. Cell Dev. Biol. 34:217–38

Figure 4. (a) (i) Large granules (arrows), identified as acidocalcisomes, as well as smaller granules (arrowheads) are observed by electron microscopy in *Agrobacterium tumefaciens*. (ii) Isolated acidocalcisomes appear to be membrane-bounded, as indicated by the caret. Panel a from Seufferheld et al. (2003) and reproduced with permission from The American Society for Biochemistry and Molecular Biology. (b) *Rhodospirillum rubrum* forms acidocalcisomes (arrows) (i) that appear to be surrounded by a membrane (arrowhead) in sectioned cells (ii). Panel b from Seufferheld et al. (2004) and reproduced with permission from The American Society for Biochemistry and Molecular Biology. (c) (i) Electron-dense granules are apparent in *Desulfovibrio magneticus* after transitioning out of iron starvation. (ii) Cryo-electron microscopy revealed a membrane surrounding the iron-containing granules. Panel c from Byrne et al. (2010) and reproduced with permission from The National Academy of Sciences. (d) (i) *Shewanella putrefaciens* forms electron-dense granules (arrowheads) when respiring on ferrihydrite (arrows). (ii) A cross section shows a membrane (arrowheads) surrounding the granules. Panel d from Glasauer et al. (2002) and reproduced with permission from The American Association for the Advancement of Science.

Chapter 2

Genome editing method for the anaerobic magnetotactic bacterium *Desulfovibrio magneticus* RS-1

Carly R. Grant, Lilah Rahn-Lee, Kristen N. LeGault, Arash Komeili

Department of Plant and Microbial Biology
University of California, Berkeley

The work presented in this chapter has been published previously in *Applied and Environmental Microbiology* (2018).

ABSTRACT
Magnetosomes are complex bacterial organelles that serve as model systems for studying bacterial cell biology, biomineralization, and global iron cycling. Magnetosome biogenesis is primarily studied in two closely related *Alphaproteobacteria* of the genus *Magnetospirillum* that form cubooctahedral-shaped magnetite crystals within a lipid membrane. However, chemically and structurally distinct magnetic particles have been found in physiologically and phylogenetically diverse bacteria. Due to a lack of molecular genetic tools, the mechanistic diversity of magnetosome formation remains poorly understood. *Desulfovibrio magneticus* RS-1 is an anaerobic sulfate-reducing deltaproteobacterium that forms bullet-shaped magnetite crystals. A recent forward genetic screen identified 10 genes in the conserved magnetosome gene island of *D. magneticus* that are essential for its magnetic phenotype. However, this screen likely missed mutants with defects in crystal size, shape, and arrangement. Reverse genetics to target the remaining putative magnetosome genes using standard genetic methods of suicide vector integration have not been feasible due to the low transconjugation efficiency. Here, we present a reverse genetic method for targeted mutagenesis in *D. magneticus* using a replicative plasmid. To test this method, we generated a mutant resistant to 5-fluorouracil by making a markerless deletion of the *upp* gene that encodes uracil phosphoribosyltransferase. We also used this method for targeted marker exchange mutagenesis by replacing *kupM*, a gene identified in our previous screen as a magnetosome formation factor, with a streptomycin resistance cassette. Overall, our results show that targeted mutagenesis using a replicative plasmid is effective in *D. magneticus* and may also be applied to other genetically recalcitrant bacteria.

IMPORTANCE
Magnetotactic bacteria (MTB) are a group of organisms that form intracellular nanometer-scale magnetic crystals through a complex process involving lipid and protein scaffolds. These magnetic crystals and their lipid membranes, termed magnetosomes, are model systems for studying bacterial cell biology and biomineralization and are potential platforms for biotechnological applications. Due to a lack of genetic tools and unculturable representatives, the mechanisms of magnetosome formation in phylogenetically deeply branching MTB remain unknown. These MTB contain elongated bullet-/tooth-shaped magnetite and greigite crystals that likely form in a manner distinct from that of the cubooctahedral-shaped magnetite crystals of the genetically tractable MTB within the *Alphaproteobacteria*. Here, we present a method for genome editing in *Desulfovibrio magneticus* RS-1, a cultured representative of the deeply branching MTB of the class *Deltaproteobacteria*. This marks a crucial step in developing *D. magneticus* as a model for studying diverse mechanisms of magnetic particle formation by MTB.

INTRODUCTION
Magnetotactic bacteria (MTB) are a group of diverse microorganisms that align along magnetic fields via their intracellular chains of magnetic crystals (10, 119). Each magnetic crystal consists of either magnetite (Fe_3O_4) or greigite (Fe_3S_4) and is synthesized within a complex organelle called a magnetosome (9). The first cultured MTB were

microaerophilic *Alphaproteobacteria*, which form cubooctahedral-shaped magnetite crystals, and have served as model organisms for understanding magnetosome formation (14, 15, 120, 121). Early studies on *Magnetospirillum* spp. revealed a lipid-bilayer membrane, with a unique suite of proteins, surrounding each magnetite crystal (17–19). Development of genetic tools in *Magnetospirillum magneticum* AMB-1 and *Magnetospirillum gryphiswaldense* MSR-1 revealed a conserved magnetosome gene island (MAI) that contains the factors necessary and sufficient for the formation of the magnetosome membrane, magnetite biomineralization within the lumen of the magnetosome, and alignment of the magnetosomes in a chain along the length of the cell (9, 122). These molecular advances, along with the magnetic properties of magnetosomes, have made MTB ideal models for the study of compartmentalization and biomineralization in bacteria as well as a target for the development of biomedical and industrial applications.

Improvements in isolation techniques and sequencing have revealed that MTB are ubiquitous in many aquatic environments. On the basis of phylogeny and magnetosome morphology, MTB can be categorized into two subgroups. The first subgroup includes members of the *Alphaproteobacteria* and *Gammaproteobacteria*, such as *Magnetospirillum* spp., that synthesize cubooctahedral, elongated octahedral, or elongated prisms of magnetite (123). The second subgroup comprises MTB from more deep-branching lineages, including members of the *Deltaproteobacteria* class and the *Nitrospirae* and *Omnitrophica* phyla, which synthesize elongated bullet-/tooth-shaped magnetite and/or greigite crystals (37, 124). While all MTB sequenced to date have their putative magnetosome genes arranged in a distinct region of their genomes (9, 26, 27, 31), many of the genes essential for magnetosome biogenesis in *Magnetospirillum* spp. are missing from the genomes of deep-branching MTB (124). Likewise, a conserved set of *mad* (magnetosome associated *Deltaproteobacteria*) genes are only found in deep-branching MTB (51, 52, 124, 125). This suggests a genetic diversity underpinning the control of magnetosome morphology and physiology in nonmodel MTB that is distinct from the well-characterized *Magnetospirillum* spp.

Desulfovibrio magneticus RS-1, one of the few cultured MTB outside the *Alphaproteobacteria*, is an anaerobic sulfate-reducing member of the *Deltaproteobacteria* that forms irregular bullet-shaped crystals of magnetite (126, 127). As with the *Magnetospirillum* spp., the magnetosome genes of *D. magneticus* are located within a MAI and include homologs to some *mam* genes as well as *mad* genes (51, 124, 128). Recently, we used a forward genetic screen combining random chemical and UV mutagenesis with whole genome resequencing to identify mutations that resulted in nonmagnetic phenotypes. These included many mutants that had the entire MAI deleted (ΔMAI) as well as mutants with point mutations, frameshift mutations, and transposon insertions in ten *mam* and *mad* genes of the *D. magneticus* MAI that resulted in nonmagnetic phenotypes (52). However, this screen relied on a strict selection scheme for nonmagnetic mutants. As such, we likely missed magnetosome genes that are important for regulating the shape, size, and arrangement of magnetosomes. To elucidate

the degree of conservation between *mam* genes and determine the function of the proteins encoded by *mad* genes in *D. magneticus*, a reverse genetic method for targeted mutagenesis is necessary.

D. magneticus and other *Desulfovibrio* spp. have gained much attention for their importance in the global cycling of numerous elements, in biocorrosion, and in the bioremediation of toxic metal ions (129, 130). The development of genetic tools, such as expression vectors, transposons, and targeted genome editing systems, has enabled a more detailed examination of the important activities of a few *Desulfovibrio* spp. (131, 132). Targeted mutagenesis using a one-step double recombination method was first achieved in *Desulfovibrio fructosivorans* and, more recently, in *Desulfovibrio gigas* and *Desulfovibrio desulfuricans* ND132 (133–135). With this method, plasmids that are electroporated into the cell are thought to be rapidly linearized by endogenous restriction modification systems (135–137). The linearized plasmid DNA, carrying a selectable marker flanked by upstream and downstream regions of homology to a target gene, can then undergo double recombination into the chromosome in one step (Figure 1A). This efficient one-step method, which is dependent on electroporation of the plasmid (133–135), is unlikely to be applicable for *D. magneticus* because plasmid uptake has only been demonstrated using conjugal transfer (52). The second targeted mutagenesis method, used in *Desulfovibrio vulgaris* Hildenborough, is a two-step double recombination that makes use of a nonreplicative, or suicide, vector (136, 137). In the first step of this method, a suicide vector, with sequences upstream and downstream of the target gene, integrates into the genome upon the first homologous recombination event (Figure 1B). Next, a second recombination event occurs whereby the vector is excised from the genome, and cells with the desired genotype are selected with an antibiotic marker and/or a counterselection marker (136, 137) (Figure 1B). For many bacteria, including *D. magneticus*, plasmid uptake and integration occur at frequencies that are too low for genetic manipulation via suicide vectors (52).

Here, we describe the method we developed for targeted gene deletion using a replicative plasmid, thereby bypassing the need for suicide vector integration (Figure 1C). We generated a mutant resistant to 5-fluorouracil by making a markerless deletion of the *upp* gene, which encodes an enzyme in the pyrimidine salvage pathway that is nonessential under standard laboratory conditions. Additionally, we deleted *kupM*, a gene encoding a potassium transporter that acts as a magnetosome formation factor (52), via marker exchange with a streptomycin resistance cassette. The deletion of both *upp* and *kupM* conferred the expected phenotypes, which were subsequently complemented *in trans*. Overall, our results show that targeted mutagenesis using a replicative plasmid is possible in *D. magneticus.* It may also be suitable for other bacteria for which replicative plasmid uptake is possible, but at a rate too low for suicide vector integration.

RESULTS

Design of a replicative deletion plasmid using *sacB* counterselection. Targeted genetic manipulation in most bacteria requires a method to efficiently deliver foreign DNA

destined for integration into the chromosome. One commonly used method involves suicide vector uptake and integration prior to the first selection step (Figure 1B). In *D. magneticus*, plasmid transfer has only been achieved via conjugation at low efficiencies, making the uptake and subsequent integration of suicide vectors into its chromosome an unlikely event (52). As such, we attempted to bypass the use of suicide vectors and use a stable, replicative plasmid designed to delete specific genes via homologous recombination (Figure 1C). Two features of this method enable the isolation of desired mutants: (i) a selectable marker is used to identify double recombination events at the targeted site and (ii) a counterselectable marker distinguishes the desired mutant cells, which have lost all remaining copies of the plasmid.

sacB is a common counterselection marker that is effective in many bacteria. The *sacB* gene from *Bacillus subtilis* encodes levansucrase, which converts sucrose to levans that are lethal to many Gram-negative bacteria, including *D. vulgaris* Hildenborough (136, 138, 139). To test its functionality in *D. magneticus*, we inserted *sacB* under the expression of the *mamA* promoter of *D. magneticus* (described in reference 52) in a plasmid that replicates in both *Escherichia coli* and *D. magneticus* (Figure 2A). This plasmid (pAK914) and a control plasmid were then conjugated into *D. magneticus*. We found no growth inhibition for *D. magneticus* cells with the control plasmid in the presence of sucrose and kanamycin. In contrast, cells expressing *sacB* were unable to grow with kanamycin and sucrose concentrations of 1% (wt/vol) or higher (data not shown). To test if the plasmids could be cured, *D. magneticus* with pAK914 was passaged two times in liquid medium containing no antibiotic and plated on 1% sucrose. Individual sucrose-resistant (Suc^r) colonies were inoculated and screened for kanamycin sensitivity (Kan^s). All isolated colonies (n=16) were Kan^s, suggesting that the cells had lost the plasmid. These experiments demonstrate that *sacB* is a suitable counterselection marker in *D. magneticus*.

Construction of a Δ*upp* strain by markerless deletion. To test our replicative deletion method, we chose to target the *upp* gene, the mutation of which has a selectable phenotype. The *upp* gene encodes uracil phosphoribosyltransferase (UPRTase), a key enzyme in the pyrimidine salvage pathway that catalyzes the reaction of uracil with 5-phosphoribosyl-α-1-pyrophosphate (PRPP) to UMP and PP_i (140) (Figure 3A). When given the pyrimidine analog 5-fluorouracil (5-FU), UPRTase catalyzes the production of 5-fluoroxyuridine monophosphate (5-FUMP). 5-FUMP is further metabolized and incorporated into DNA, RNA, and sugar nucleotides resulting in eventual cell death (Figure 3A) (141, 142). Previous studies have shown that Δ*upp* mutants of *D. vulgaris* Hildenborough are resistant to 5-FU, while wild-type (WT) cells are effectively killed by the pyrimidine analog (137, 143). The *D. magneticus* genome has a homolog (*DMR_08390*) to the *D. vulgaris* Hildenborough *upp* gene that is likely functional, as detected by the sensitivity of *D. magneticus* to 5-FU (Figure 3B and Figure 4A). To show that the *upp* gene product confers 5-FU sensitivity and to validate our replicative deletion system, we chose to target the *D. magneticus upp* gene for markerless deletion.

To construct a *upp* deletion vector, a markerless cassette containing the regions upstream and downstream of the *upp* gene were inserted into plasmid pAK914 (Figure 2B). The resulting plasmid (pAK1126) was transferred to WT *D. magneticus* by conjugation and single kanamycin-resistant (Kan^r) colonies were isolated and passaged in growth medium containing no antibiotic. Since *D. magneticus* has interesting features independent of its magnetosomes, the same deletion procedure was also carried out in a nonmagnetic strain (ΔMAI) isolated in our previous genetic studies (52). After the third passage, *upp* mutants that had lost the vector backbone were selected for with 5-FU and sucrose. Compared with those obtained using a control plasmid (pAK914), >20-fold more 5-FU-resistant (5-FU^r) mutants were generated using pAK1126 at a frequency of approximately 10^{-6}. PCR of the region flanking the *upp* gene confirmed that the 5-FU^r colonies harboring pAK1126 resulted from a markerless deletion of *upp* (Δ*upp*), while 5-FU^r colonies from pAK914 were likely the result of point mutations (Figure 3B,D). Similar to the results obtained for *D. vulgaris* Hildenborough (137), the Δ*upp* mutant of *D. magneticus* grew in the presence of 5-FU (Figure 4B, Table 1). Complementation of the *upp* gene *in trans* restored UPRTase function, and the cells no longer grew with 5-FU (Figure 2C, Figure 4C, Table 1). These experiments demonstrate that a replicative plasmid can be used to directly edit the *D. magneticus* genome.

Construction of a Δ*kupM* strain by marker exchange mutagenesis. Because many genetic mutations do not confer a selectable phenotype, we sought to develop our replicative deletion plasmid for marker exchange mutagenesis. To test this system, we chose to replace a gene with a known phenotype, *kupM* (*DMR_40800*), with a streptomycin-resistance gene cassette (*strAB*). *kupM* is located in the *D. magneticus* MAI and encodes a functional potassium transporter (52). Mutant alleles in *kupM*, including missense, nonsense, and frameshift mutations, were previously identified in our screen for nonmagnetic mutants (52). These *kupM* mutations resulted in cells that rarely contained electron-dense particles and were unable to turn in a magnetic field, as measured by the coefficient of magnetism (C_{mag}) (52).

To mutate *kupM*, we inserted a marker exchange cassette, with regions upstream and downstream of *kupM* flanking *strAB*, into pAK914 (Figure 2D) to create the deletion plasmid pAK941. Following conjugation, single colonies of *D. magneticus* harboring pAK941 were isolated by kanamycin selection. After three passages in growth medium without selection, potential mutants were isolated at a frequency of approximately 10^{-6} on plates containing streptomycin and sucrose. Single colonies that were streptomycin resistant (Str^r) and Suc^r were inoculated in liquid medium and screened for Kan^s. Of the isolates screened (n = 48), 20% were Kan^s and 4% had the correct genotype (Δ*kupM*::*strAB*) as confirmed by PCR and sequencing (Figure 3C,E).

Similar to the phenotypes previously observed in *kupM* mutants (52), Δ*kupM*::*strAB* cells were severely defective in magnetosome synthesis (Figure 5). Although a slight C_{mag} was measured, few cells contained electron-dense particles or magnetosomes. Importantly, the WT phenotype was rescued by expressing *kupM* from a plasmid in the Δ*kupM*::*strAB*

mutant (Figure 5). These results confirm that the replicative deletion plasmid method described here can be used successfully for marker exchange mutagenesis.

DISCUSSION

In this study, we expand the genetic toolbox for *D. magneticus* to include a replicative plasmid method for targeted mutagenesis (Figure 1C). We show the utility of this method for markerless deletion of genes with a selectable phenotype and for marker exchange mutagenesis. Some of the earliest examples of targeted mutagenesis in Gram-negative bacteria used replicative plasmids, similar to the method described here (139, 144). These studies, which predated the application of suicide vectors, relied on plasmid instability by introducing a second plasmid of the same incompatibility group or by limiting nutrients in the growth medium (139, 144).

Because the *D. magneticus* genetic toolbox has a limited number of plasmids, antibiotic markers, and narrow growth constraints, we used a replicative plasmid and established *sacB* as a counterselection marker to generate and isolate mutants. While *sacB* counterselection was ultimately successful, a large number of false positives were also isolated at the sucrose selection step. Mutations in *sacB* have been found to occur at a high frequency in many bacteria (136, 145–148). Indeed, we found that deletions and mutations in P_{mamA}-*sacB* are abundant in the false-positive Suc^r Str^r isolates (data not shown). Alternative counterselection markers, including *upp*, have been shown to select for fewer false positives (137, 148–150). Since *D. magneticus* is sensitive to 5-FU only when the *upp* gene is present (Figure 4), the *upp* mutants generated in this study may be used as the parent strains for future targeted mutagenesis with *upp*, rather than *sacB*, serving as a counterselectable marker. Additionally, the combined use of *upp* and *sacB* for counterselection might reduce the false-positive background that results from the accumulation of mutations in these markers.

The replicative deletion plasmid described here was designed to replace a target gene with an antibiotic resistance marker. As such, the construction of strains with multiple directed mutations will be complicated by the need for additional antibiotic-resistance markers, which are limited in *D. magneticus*. These limitations may be overcome by removing the chromosomal antibiotic marker in subsequent steps (139, 151, 152). Ultimately, improvements in conjugation efficiency or methods for electroporation with high transformation efficiency are desired. Similar to the ongoing development of genetics in *D. vulgaris* Hildenborough, establishment of a suicide vector delivery system in *D. magneticus* will enable more high-throughput targeted mutagenesis and even the construction of markerless deletion mutants (131, 137).

Overall, we have demonstrated the utility of a replicative deletion plasmid to generate targeted mutants of *D. magneticus*. This method marks a crucial step in developing *D. magneticus* as a model for the study of anaerobic sulfate reduction and diverse mechanisms of magnetic particle formation by MTB. Both MTB and sulfate-reducing bacteria have been singled out for their role in the global cycling of numerous elements

and for potential applications, such as bioremediation (129, 130, 153, 154). *D. magneticus*, in particular, may be useful in the bioremediation of heavy metals and in the global cycling of iron, since it can form both magnetosomes and other iron-containing organelles (50, 155). Through genetic manipulation of *D. magneticus*, pathways of elemental cycling and heavy metal turnover may now be explored. Additionally, genetic manipulation of *D. magneticus* will further our understanding of magnetosome formation and provide answers to many longstanding questions for the deeply branching MTB. Which proteins regulate and control magnetosome formation? To what extent are lipid membranes involved in forming these crystals? How is the elongated and irregular crystal shape achieved? Finally, in addition to *D. magneticus*, the method described here may extend to other bacteria that are not amenable to targeted mutagenesis with suicide vectors but are able to accommodate replicative plasmids.

MATERIALS AND METHODS

Strains, media, and growth conditions. The bacterial strains used in this study are listed in Table 2. All *E. coli* strains were cultured aerobically with continuous shaking at 250 rpm at 37ºC in lysogeny broth (LB). *D. magneticus* strains were grown anaerobically at 30ºC in sealed Balch tubes with a N_2 headspace containing RS-1 growth medium (RGM) that was degassed with N_2, unless otherwise stated (50). Sodium pyruvate (10 mM) was used as an electron donor with fumaric acid disodium (10 mM) as the terminal electron acceptor. RGM was buffered with HEPES, and the pH was adjusted to 6.7 with NaOH (52). Before inoculating with cells, RGM was supplemented with 0.8% (vol/vol) Wolfe's vitamins, 100 μM ferric malate, and 285 μM cysteine-HCl (50). Solid agar plates were prepared by adding 1.5% agar (wt/vol) to LB and 1% agar (wt/vol) to RGM. Vitamins (0.8% [vol/vol]), ferric malate (20 μM), and cysteine (285 μM) as well as antibiotics and selective agents, were added to the molten RGM agar as needed. For *D. magneticus*, all plating steps were carried out aerobically, and the bacteria were transferred to an anaerobic jar and incubated at 30ºC for 10 to 14 days, as described previously (52). The antibiotics and selective agents used are as follows: kanamycin (50 μg/ml for *E. coli* strains, 125 μg/ml for *D. magneticus* strains), streptomycin (50 μg/ml for *E. coli* and *D. magneticus* strains), diaminopimelic acid (300 μM for *E. coli* WM3064), 5-FU (2.5 μg/ml for *D. magneticus* strains), and sucrose (1% for *D. magneticus* strains).

Plasmids and cloning. All plasmids used in this work are listed in Table 2. All cloning was performed in *E. coli* DH5α λpir using the Gibson method (156) or restriction enzyme ligation. For PCR amplification, KOD (EMD Millipore, Germany) and GoTaq (Promega, USA) DNA polymerases were used with the primers listed in Table 3. All upstream and downstream homology regions were amplified from *D. magneticus* genomic DNA. *strAB* and P_{npt} were amplified from pBMS6 and pLR6, respectively, and subcloned into pBMC7 to make pAK920, which served as the template for amplifying P_{npt}-*strAB* for the deletion vectors. *sacB* was amplified from pAK0 and inserted into pLR6 digested with SalI and XbaI to create pAK914. To construct a plasmid for the targeted deletion of *upp* (*DMR_08390*), 991 bp upstream and 1,012 bp downstream of *upp* were amplified and inserted into pAK914 digested with XbaI and SacI using a 3-piece Gibson assembly. To

create the *upp* complementation plasmid, pAK914 was digested with BamHI and SacI, and the *upp* gene, with its promoter, were PCR amplified from *D. magneticus* genomic DNA. To construct pAK941 for marker exchange mutagenesis of *kupM*, a cassette of 1,064 bp upstream region and 1,057 bp downstream region flanking P_{npt}-*strAB* was assembled using Gibson cloning. The cassette was amplified and inserted into pAK914 digested with XbaI using a two-piece Gibson assembly.

***upp* and *kupM* mutant generation and complementation.** Replicative deletion plasmids were transformed into *E. coli* WM3064 by heat shock and transferred to *D. magneticus* by conjugation, as described previously (52). Single colonies of Kan^r *D. magneticus* were isolated and inoculated in RGM containing no antibiotic. Cultures were passaged and, after the third passage, approximately 2×10^8 cells were spread on 1% agar RGM plates containing either 50 μg/ml streptomycin and 1% sucrose or 2.5 μg/ml 5-FU and 1% sucrose. $5FU^r$ Suc^r and Str^r Suc^r colonies harboring plasmids pAK1126 and pAK941, respectively, were recovered at a frquency of approximately 10^{-6}. Single colonies were screened for Kan^s and by PCR using the primers listed in Table 3. Successful *upp* and *kupM* mutants were confirmed by Sanger sequencing. The expression plasmids for the complementation of Δ*kupM::strAB* and Δ*upp*, as well as empty vectors for controls, were transferred to *D. magneticus* strains as described above. Transconjugants were inoculated into RGM containing kanamycin to maintain the plasmids.

Mutant phenotype and complementation analyses. The growth and coefficient of magnetism (C_{mag}) of *D. magneticus* strains were measured in a Spec20 spectrophotometer at an optical density of 650 nm (OD_{650}), as described previously (19, 50). For *upp* mutant and complementation analysis, RGM was supplemented with 5-FU (1.25 μg/ml in 0.01% dimethyl sulfoxide [DMSO]) or DMSO (0.01%) and the growth was measured for WT and Δ*upp* strains with an empty vector (pAK914) and for the Δ*upp* strain with the complementation plasmid pAK1127. For *kupM* mutant and complementation analysis, the C_{mag} was measured by placing a large bar magnet parallel or perpendicular to the sample to measure the maximum or minimum absorbance, respectively, as the *D. magneticus* strains rotate 90º with the magnetic field. The ratio of maximum to minimum absorbances was calculated as the C_{mag} (19). Whole-cell transmission electron microscopy (TEM) was performed as previously described (50). The C_{mag} calculations and TEM were performed for WT *D. magneticus* with an empty vector (pBMK7) and the Δ*kupM::strAB* with an empty vector (pBMK7) or complementation plasmid (pLR41). For all growth measurements, C_{mag} measurements, and TEM, plasmids were maintained in cells with 125 μg/ml kanamycin.

ACKNOWLEDGMENTS
This work was supported by grants from the National Institutes of Health (R01GM84122 and R35GM127114), the National Science Foundation (1504681), and the Office of Naval Research (N000141310421).

FIGURES

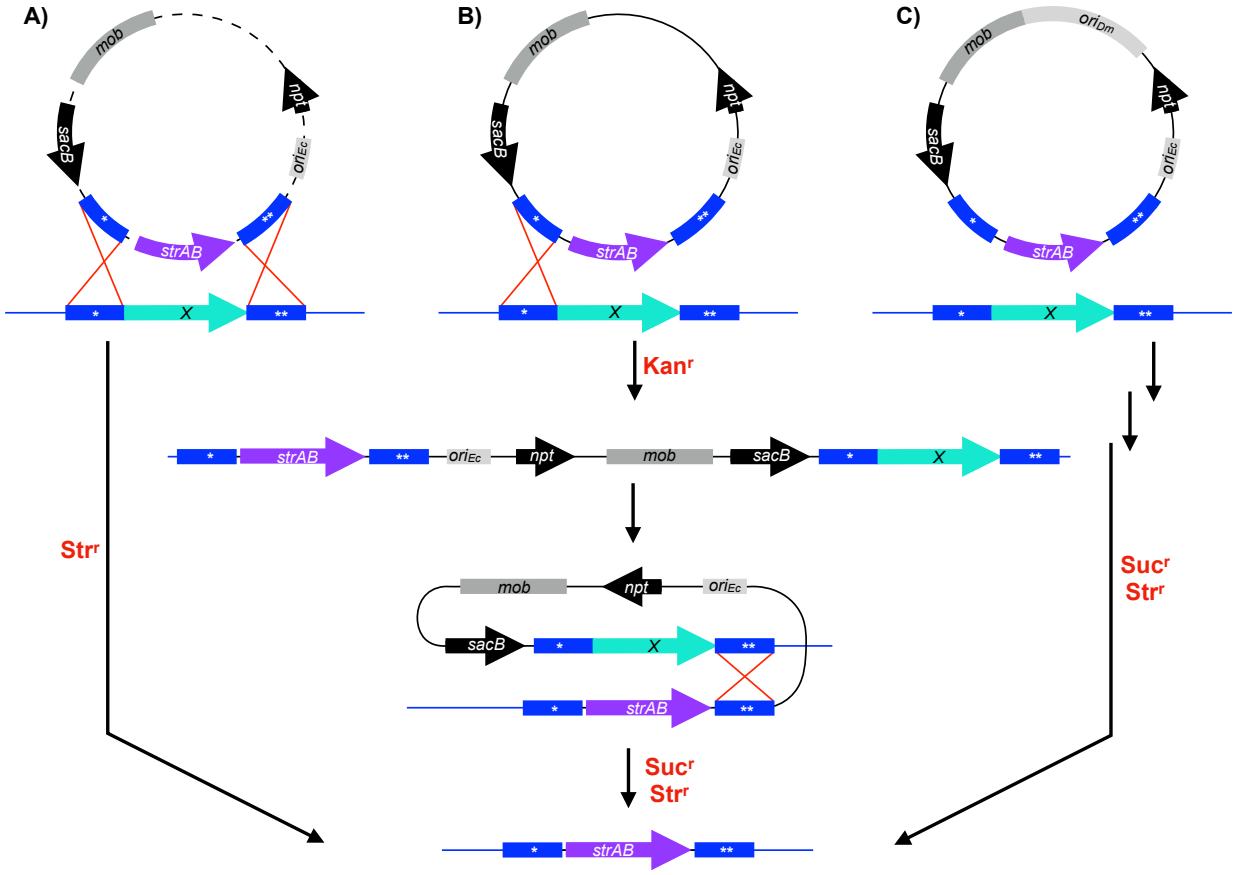

Figure 1. Schematic of deletion methods used in *Desulfovibrio* spp. Plasmids (black lines) are designed to replace a target gene (*X*, aqua arrows) in the chromosome (blue lines) with a streptomycin resistance cassette (*strAB*, purple arrows). Regions upstream (*) and downstream (**) of the target gene (blue boxes) on the chromosome undergo recombination (red lines) with homologous regions that are cloned into the deletion plasmid. Key steps, such as recombination events (red crosses), are indicated in the boxes, and the selection steps are labeled in red. (A) Double recombination can occur in one step after plasmids are linearized (dashed lines) by endogenous restriction enzymes. Mutants are selected using the marker (e.g., *strAB*) that was exchanged with the target gene. (B) Two-step double recombination is possible when suicide vectors integrate into the chromosome in the first homologous recombination event and then recombine out after the second homologous recombination event. The first step and second step are selected for with antibiotic resistance markers (e.g., *npt*) and counterselectable markers (e.g., *sacB*), respectively. (C) A replicative deletion plasmid designed to target genes for deletion may undergo double recombination in one or two steps as shown in panels A and B, respectively. After passaging the cells without antibiotic, the mutants are selected

with an antibiotic resistance cassette (e.g., *strAB*) and a counterselectable marker (e.g., *sacB*). mob, mobilization genes (*mobA′, mobB, mobC*); npt, kanamycin-resistance gene; ori_{Dm}, origin of replication for *D. magneticus*; ori_{Ec}, origin of replication for *E. coli*.

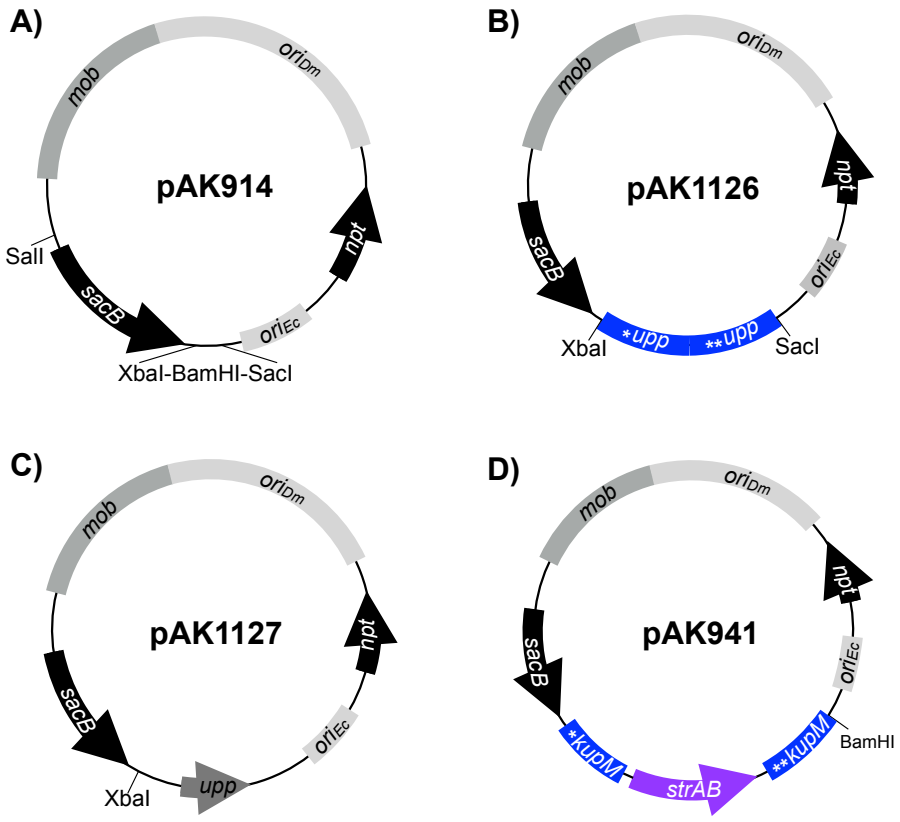

Figure 2. Plasmids constructed for the present study. (A) Expression plasmid pAK914 expresses *sacB* from the *mamA* promoter and is the parent vector for the deletion plasmids and *upp* expression plasmid described below. (B) Replicative deletion plasmid to target *upp* for markerless deletion. The *upp* deletion cassette was cloned into XbaI-SacI of pAK914. (C) Expression plasmid used for *upp* complementation. The *upp* gene and its promoter were cloned into BamHI-SacI of pAK914. (D) Replicative deletion plasmid to target *kupM* for marker exchange mutagenesis with *strAB*. The *kupM*::*strAB* deletion cassette was cloned into XbaI of pAK914. Labeling and colors correspond to those in Figure 1.

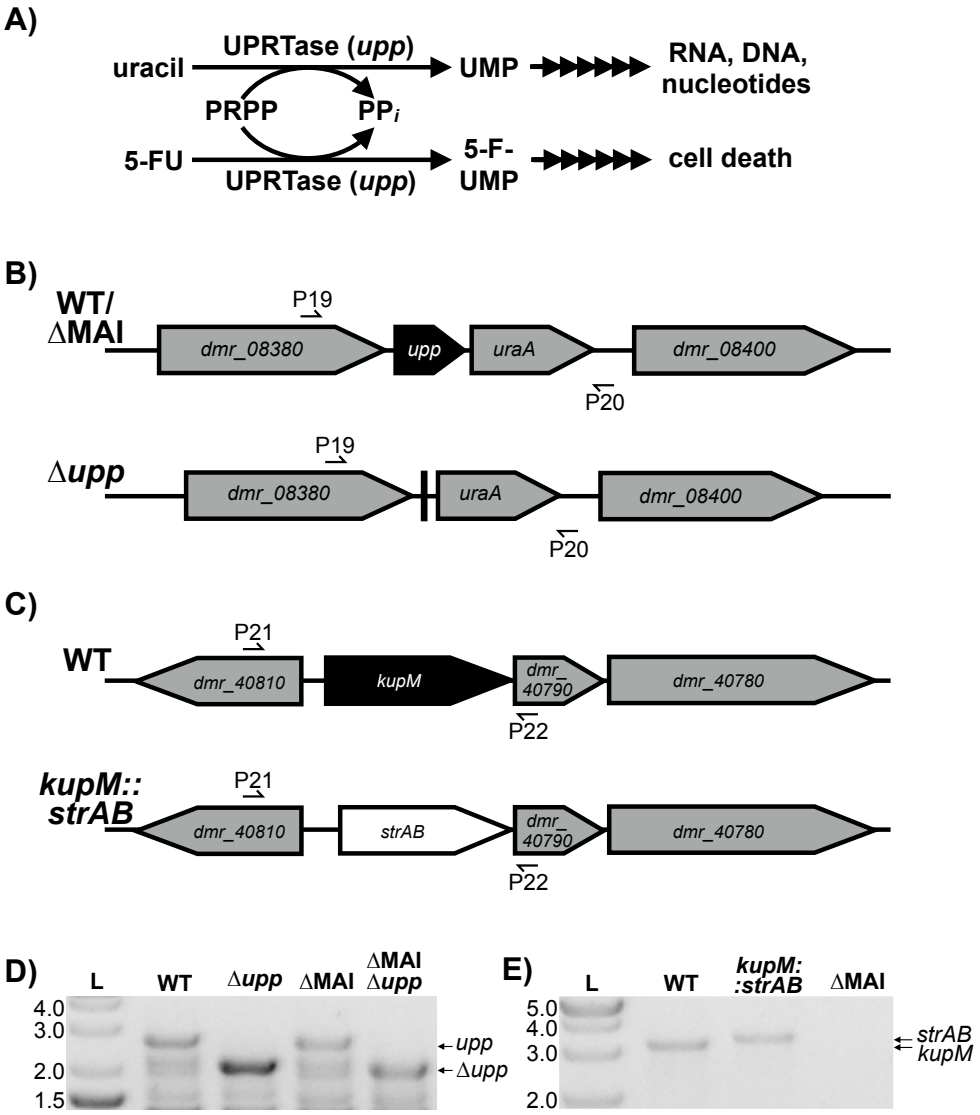

Figure 3. Confirmation of *upp* and *kupM* deletions. (A) The *upp* gene encodes UPRTase, which is a key enzyme in the uracil salvage pathway. The product of the UPRTase reaction, UMP, is processed by downstream enzymes in pathways for RNA, DNA, and sugar nucleotide synthesis. 5-FU causes cell death by incorporating into this pathway via UPRTase. (B) Schematic of genomic regions of *upp* in the WT or the ΔMAI mutant (top) and the Δ*upp* mutant (bottom). (C) Genomic region of *kupM* in WT (top) and *kupM*::*strAB* (bottom) strains. Primers used to screen for the correct genotype are indicated with half arrows. (D) Δ*upp* mutants in WT and ΔMAI backgrounds were confirmed by PCR using primers P19/P20 and agarose gel electrophoresis. WT and ΔMAI strains show a band corresponding to the *upp* gene (2,691 bp), while the Δ*upp* mutants have a smaller band corresponding to a markerless deletion of the *upp* gene (2,079 bp). The lower bands are likely nonspecific PCR products. (E) *kupM*::*strAB* genotype confirmation by PCR and agarose gel electrophoresis using primers P21/P22 (WT, 3,069 bp; *kupM*::*strAB*, 3,263 bp; ΔMAI, not applicable [NA]).

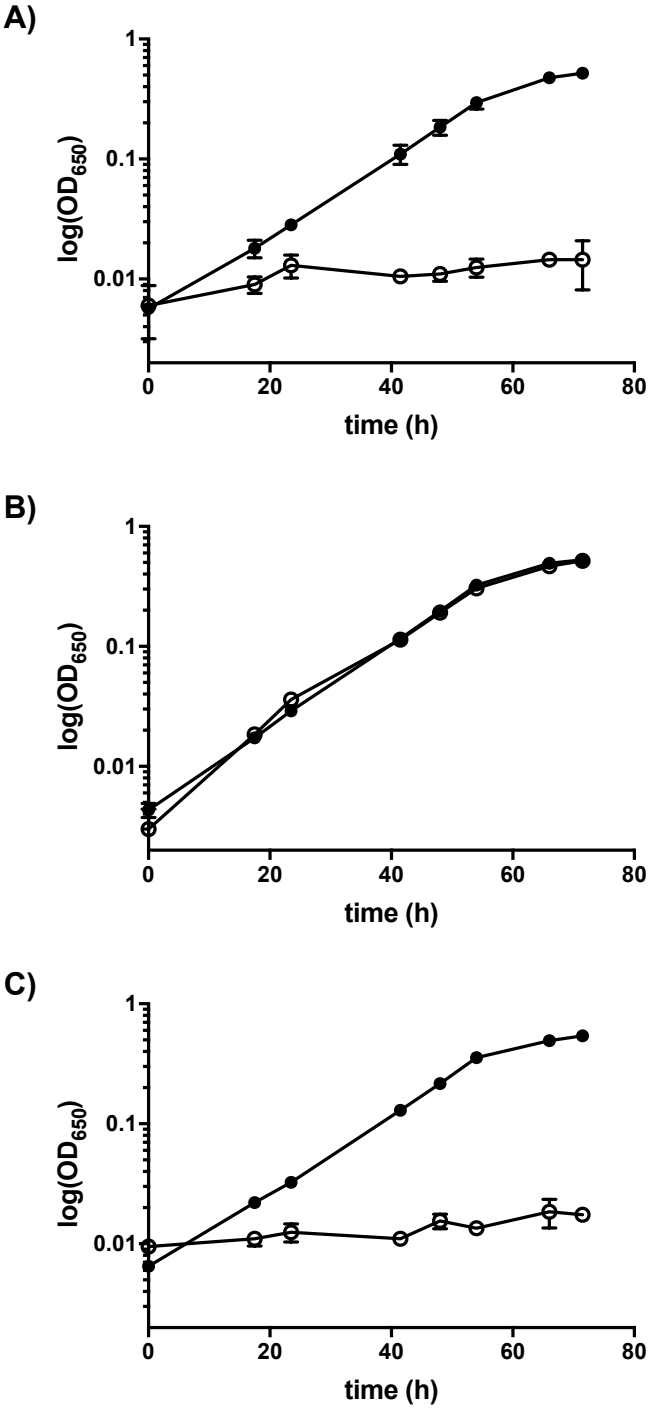

Figure 4. *upp* mutant and complementation phenotype. Growth of the parent strain (ΔMAI) (A), *upp* deletion (ΔMAI Δ*upp*) (B), and complementation of the *upp* deletion (ΔMAI Δ*upp*/*upp*$^{+}$) (C) when grown with 1.25 μg/ml 5-FU (○) or without 5-FU (●). Data presented are averages from 2 to 3 independent cultures; error bars indicate the standard deviations.

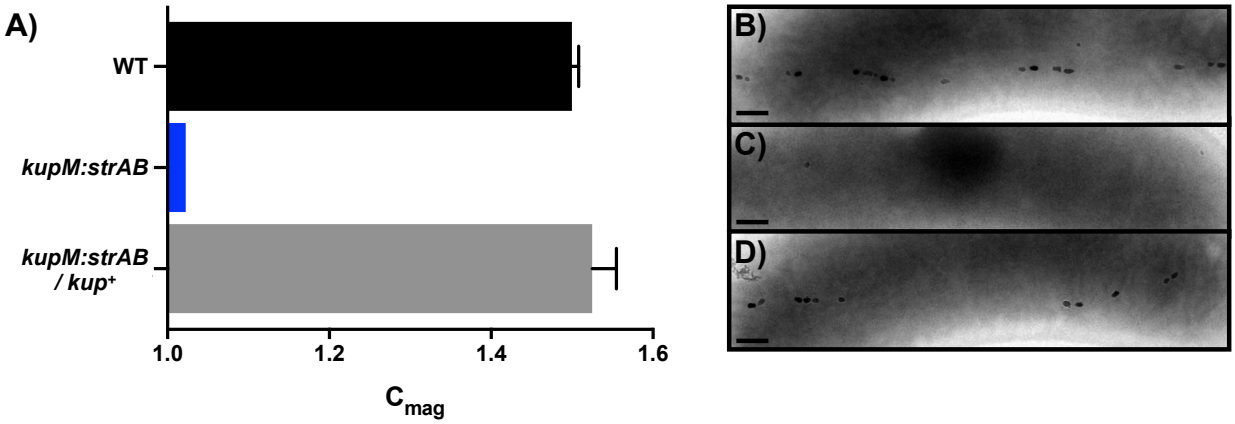

Figure 5. *kupM* mutant and complementation phenotype. C_{mag} values (A) and electron micrographs of WT (B), *kupM*::*strAB* (C), and Δ*kupM*::*strAB/kupM*$^{+}$ (D) strains. Scale bars, 200 nm. Data presented are averages from 4 independent cultures; error bars indicate the standard deviations.

Strain	Growth rate (h^{-1})		Generation time (h)	
	Without 5-FU	With 5-FU	Without 5-FU	With 5-FU
ΔMAI	0.077 ± 0.0017	NA[a]	9.1 ± 0.2	NA
ΔMAI Δ*upp*	0.079 ± 0.0017	0.070 ± 0.0040	8.8 ± 0.2	10.0 ± 0.6
ΔMAI Δ*upp*/*upp*$^+$	0.076 ± 0.0041	NA	9.1 ± 0.5	NA

[a]NA, not applicable.

Table 1. Growth rates and generation times of the parent strain (ΔMAI), Δ*upp* mutant, and *upp* complementation in *trans* with and without treatment with 5-FU.

Strain or plasmid	Genotype or relevant characteristics	Reference or source
Strains		
E. coli		
DH5α λpir	Cloning strain	Lab strain
WM3064	Conjugation strain; DAP auxotroph used for plasmid transfer	Lab strain
D. magneticus		
AK80	Non-motile mutant of *D. magneticus* strain RS-1, referred to as wild-type	(50)
AK201	ΔMAI	(52)
AK267	ΔMAI Δ*upp*	This study
AK268	Δ*upp*	This study
AK270	Δ*kupM*::*strAB*	This study
Plasmids		
pBMK7	Conjugative vector with pBG1 and pMB1 replicons; Kan^r	(157)
pBMC7	Conjugative vector with pBG1 and pMB1 replicons; Cm^r	(157)
pBMS6	Cloning vector; source of *strAB*; Str^r	(157)
pLR6	pBMK7 with P_{mamA} in HindIII-SalI; source of P_{npt}; Kan^r	(52)
pLR41	pLR6 with P_{mamA}-*kupM* in SalI; Kan^r	(52)
pAK0	Cloning vector, source of *sacB*; Kan^r	(19)
pAK914	pLR6 with *sacB* in SalI-XbaI; Kan^r	This study
pAK920	pBMC7 with P_{npt}-*strAB* inserted into SacI site; Cm^r Str^r	This study
pAK941	pAK914 with cassette of 1,064 bp upstream and 1,057 bp downstream of *kupM* flanking P_{npt}-*strAB* in XbaI; Kan^r Str^r	This study
pAK1126	pAK914 with cassette of 991 bp upstream and 1,012 bp downstream of *upp* in XbaI-SacI; Kan^r	This study
pAK1127	pAK914 with P_{upp}-*upp* in BamHI-SacI; Kan^r	This study

Table 2. Bacterial strains and plasmids used in this study.

Name	Sequence from 5' end	Description[a]
P1	aagccaagaaaaacgtcgccaacgtcgacatgaacatcaaaaagtttgca	F *sacB* for pAK914
P2	gctcggtacccggggatcctctagaggccaataggatatcggcattt	R *sacB* for pAK914
P3	cgactctagaggatccccgggtaccgtagcttcacgctgccgcaag	F P_{npt} for pAK920
P4	cccgaatgtgcatgcgaaacgatcctcatcctgtc	R P_{npt} for pAK920
P5	aggatcgtttcgcatgcacattcgggatatttctcta	F *strAB* for pAK920
P6	taatacgactcactatagggaattcgcccaggggataggagaagtc	R *strAB* for pAK920
P7	aaatgccgatatcctattggcctctagagagatcgcgaagcagagc	F *kupM* upstream for pAK941
P8	tgcggcagcgtgaagctacggtaccgccgtaatgcgtcagaaagt	R *kupM* upstream for pAK941
P9	cttctcctatcccctgggcgaattcagccgggtcatggaagtc	F *kupM* downstream for pAK941
P10	cgagctcggtacccggggatcctctagaggccagggaatggagttt	R *kupM* downstream for pAK941
P11	ggtaccgtagcttcacgctgccgca	F P_{npt}-*strAB* for pAK941
P12	gaattcgcccaggggataggagaagtcgct	R P_{npt}-*strAB* for pAK941
P13	gccgatatcctattggcctctagagcctcccagatcgaccagtc	F *upp* upstream for pAK1126
P14	ctatttggtgccggatcccatggacgcgctcctggg	R *upp* upstream for pAK1126
P15	agcgcgtccatgggatccggcaccaaataggggg	F *upp* downstream for pAK1126
P16	cgactcactatagggaattcgagctcgccaggcagacggcggtg	R *upp* downstream for pAK1126
P17	gccgatatcctattggcctctagagaagctcgccgaaaagacc	F P_{upp}-*upp* for pAK1127
P18	cgactcactatagggaattcgatgaaggcgaacgaggaac	R P_{upp}-*upp* for pAK1127
P19	gcccgcattgaggacgtg	To check *upp* deletion
P20	cagcgccccgagcttgcc	To check *upp* deletion
P21	cgtcagcaggcaaacgg	To check *kupM* deletion
P22	accgttgtctcccatgtctc	To check *kupM* deletion

[a]F, forward; R, reverse.

Table 3. Primers used in this study.

Chapter 3

Genetic Basis of an Iron Storage Organelle, the Ferrosome, in Diverse Anaerobic Bacteria

Carly R. Grant

ABSTRACT
Like eukaryotic cells, bacteria are highly organized and often contain subcellular membrane-enclosed structures, or organelles. Examples of bacterial organelles include both protein- and lipid-bounded structures and have a range of functions, including carbon fixation (e.g. carboxysomes (158)), cellular navigation (e.g. magnetosomes (9)), or preventing oxidative stress (e.g. encapsulins (8)). Other bacterial organelles have been observed; however, the genetic basis and function of these organelles has remained a mystery (159). Membrane-bounded iron-containing organelles—here named "ferrosomes" for "iron body"—have previously been observed in both *Desulfovibrio magneticus* RS-1 and *Shewanella putrefaciens* CN-32 (50, 106). Here, we report the discovery of "*fez*" gene clusters required for ferrosome formation in phylogenetically and metabolically diverse bacteria with anaerobic lifestyles, including *D. magneticus*, *S. putrefaciens*, *Rhodopseudomonas palustris* CGA009, and *Desulfovibrio alaskensis* G20. Moreover, recombinant expression of *S. putrefaciens fez* genes in *Escherichia coli* is sufficient for heterologous ferrosome formation. Finally, we provide evidence that ferrosomes play a role in anaerobic iron homeostasis. Fitness studies in *S. putrefaciens* suggest that ferrosomes act as an anaerobic iron reserve analogous to ferritin. Overall, this work sets the stage for studying ferrosome formation and structure in many bacteria as well as for future uses of ferrosomes in applications that leverage their metal-accumulating capabilities or for drug targeting in pathogenic bacteria.

MAIN
Iron is an essential element for nearly all organisms as it is an enzymatic cofactor, signaling molecule, and cellular respiration component. However, when intracellular iron concentrations are too high and oxygen is present, iron can act as a catalyst for reactive oxygen species, which damage DNA, proteins, and membrane lipids. Thus, cellular iron homeostasis is vital and is maintained through tightly regulated pathways involving import, efflux, storage, and detoxification (160–162). Examples of iron storage can be found in all domains of life and has mainly been studied in the context of aerobic respiration. The importance of iron storage during anaerobic metabolism is less understood.

Desulfovibrio magneticus RS-1 is an anaerobic bacterium and an emerging model organism for studying bullet-shaped magnetosomes (126, 163). Independent of magnetosomes, *D. magneticus* makes electron-dense granules rich in iron, phosphorus, and oxygen that are enclosed by a membrane (50, 52). These granules, here on called ferrosomes, are visible in *D. magneticus* cells by transmission electron microscopy (TEM) upon transitioning out of iron starvation to conditions with low to high concentrations of iron (Supplementary Fig. 1) (50, 52).

To understand the mechanistic basis of ferrosome formation, we used mass spectrometry to identify proteins associated with isolated *D. magneticus* ferrosomes (Supplementary Fig. 2a-c). Relative protein quantification of whole cell lysate and isolated ferrosomes revealed three proteins highly enriched in the ferrosome fraction, DMR_28330 ("FezP") DMR_28340 ("FezC"), and DMR_28320 ("FezA"), that are encoded by genes predicted

to be arranged in an operon (*fezAPC*) (Fig. 1a, b). FezP, an uncharacterized heavy metal-transporting P_{1B-6}-ATPase, belongs to a large protein family that transports metals across membranes using the energy of ATP hydrolysis (164). P_{1B-6}-ATPases have the functional motifs characteristic of the A-, P-, and N-domains of all P_{1B}-ATPases, unique motifs that align with the metal binding sites of characterized P_{1B}-ATPases, and putative transmembrane domains that are difficult to predict using prediction software (Fig. 1c, Supplementary Fig. 2d, 3, Supplementary Table 1). In addition, FezP has a conserved N-terminal $Hx_3GRxRxR$ (R-rich) motif located in the domain often responsible for metal binding and/or regulation (Fig. 1c, Supplementary Fig. 3). Similar motifs are found in other P_{1B}-ATPases, including CtpC, as well as proteins of unknown function, such as FezC (Fig. 1d). The sequence similarity of FezC and the N-terminal domain of FezP is reminiscent of the similarity between the N-terminal metal-binding site of copper metallochaperones and their cognate P_{1B}-ATPase which is well described in bacteria and eukaryotes (165). Unlike characterized copper metallochaperones, FezC has predicted transmembrane domains (Supplementary Fig. 4). Lastly, *fezA* encodes a small protein with a hydrophobic N-terminal region that contains a conserved GxxxG motif, which may facilitate protein-protein interactions in membranes (166, 167), and a conserved C-terminal domain (Supplementary Fig. 5). These characteristics of metal binding, transport, and membrane domains in FezP, FezA, and FezC led us to hypothesize that the *fez* operon is the genetic blueprint of ferrosomes.

To test this hypothesis, we replaced the *fezP* and *fezC* genes with a streptomycin-resistance cassette. The resulting mutant, Δ$fezPC_{Dm}$, was unable to form ferrosomes but could still form magnetosomes and complementing Δ$fezPC_{Dm}$ with $fezAPC_{Dm}$ in *trans* rescued the phenotype (Fig. 1e-j). In addition to forming visible ferrosomes upon release from iron starvation, both the WT and Δ$fezPC_{Dm}$ mutant expressing $fezAPC_{Dm}$ in *trans* made ferrosomes in iron replete medium with no effect on magnetosome formation (Supplementary Fig. 6). Overall, these results suggest that the *fez* operon is essential for ferrosomes in *D. magneticus*. Additionally, ferrosomes and magnetosomes have different genetic requirements and are therefore distinct organelles.

A maximum likelihood tree of *D. magneticus* FezP and its top BLAST hits revealed a clear clade of FezP homologs that can be further divided into two subgroups: $FezP_A$, to which *D. magneticus* FezP belongs, and $FezP_B$ (Fig. 2). FezP homologs are found in phylogenetically diverse bacteria and archaea, most of which are strict or facultative anaerobes (Fig. 2). For microorganisms in both subgroups, the gene that encodes FezP is in a gene cluster that also encodes one or more distinct proteins of unknown function that have a hydrophobic domain containing a GxxxG motif (Supplementary Fig. 5, 7). In addition, several proteins have motifs or putative domains that resemble FezC or copper chaperones (Supplementary Fig. 4, 7). Genes in some $fezP_B$ clusters encode proteins that have been characterized in other systems. All $FezP_B$ gene clusters encode a homolog of MamC, a magnetosome membrane protein that binds to magnetite within the magnetosome lumen (168), or a related protein, FezF (Supplementary Fig. 7, 8). Proteins with domains related to iron storage, uptake, and regulation are also encoded in some

fezP$_B$ gene clusters (Supplementary Fig. 7), supporting the hypothesis that FezP transports iron (164). Lastly, some bacteria with a FezP$_B$ have a second uncharacterized P$_{1B}$-ATPase (FezH) with an R-rich motif and putative metal-binding domains that are both similar and distinct from CtpC (Fig. 2, Supplementary Fig. 7, 9). Because of the differences in the *fez* gene clusters, we next questioned whether or not bacteria with a FezP$_B$ can make ferrosomes.

Shewanella putrefaciens CN-32 was previously shown to form membrane-enclosed electron-dense granules consisting of mixed-valence iron, phosphorus, and oxygen when respiring ferrihydrite or fumarate in anaerobic growth medium supplemented with iron (106, 107) (Fig. 3b-d). Because *S. putrefaciens* has a FezP$_B$ (Fig. 3a), we hypothesized that the iron-containing granules are ferrosomes. In addition to *S. putrefaciens*, we found that *Rhodopseudomonas palustris* CGA009, which has a similar *fez* gene cluster to *S. putrefaciens* (Fig. 4a), forms granules resembling ferrosomes when grown anaerobically in photoheterotrophic medium supplemented with iron (Fig. 4b, c). This is in accordance with a proteomics study that detected all but one of the proteins encoded by the *fez* genes when *R. palustris* was grown under various anaerobic conditions while none of the proteins were detected during aerobic growth (169). *Desulfovibrio alaskensis* G20 has a larger *fez* gene region that encodes three P$_{1B}$-ATPases: two copies of FezP$_B$ and FezH (Fig. 5a, b). Similar to *S. putrefaciens* and *R. palustris*, we found that *D. alaskensis* has granules when grown anaerobically (Fig. 5d).

To show that the granules in *S. putrefaciens* and *R. palustris* are ferrosomes, we made markerless deletions of their *fez* gene clusters (Δ*fez$_{Sp}$* and Δ*fez$_{Rp}$*, respectively). Mutants lacking the *fez* genes no longer made granules and complementation by expressing the *fez* genes on a plasmid rescued the phenotype (Fig. 3e-j, 4d, e). Next, we obtained transposon mutants of each of the *D. alaskensis* ferrosome P$_{1B}$-ATPases (170). We found that a *fezP1** mutant had significantly fewer ferrosomes than WT while a *fezP2** mutant did not (Fig. 5c-f). Conversely, the *fezH** mutant had significantly more ferrosomes than WT (Fig. 5c, g). These results suggest that FezP1 may be important for iron import while FezH may be important for iron export in *D. alaskensis*. Taken together, these results support the hypothesis that diverse microorganisms make ferrosomes via conserved *fez* genes.

We next sought to determine whether or not *fez* genes are sufficient for ferrosome formation. To test this hypothesis, the *S. putrefaciens fez* gene cluster was heterologously expressed from a plasmid in *Escherichia coli*. When grown anaerobically in minimal medium supplemented with iron, *E. coli* expressing *fez$_{Sp}$* had a visibly dark pellet whereas the *E. coli* control had a white pellet (Fig. 6a, b). TEM revealed electron-dense granules in the *E. coli / fez$_{Sp}^{+}$* that had a dark pellet (Fig. 6). The granules have a diameter of around 20 nm which is nearly double that of the iron storage proteins found naturally in *E. coli* (160). Therefore, we presume that these granules are ferrosomes and the dark color of the cell pellet is due to the iron stored within the ferrosomes.

Despite the dramatic iron-loading by ferrosomes upon release from iron deprivation in *D. magneticus*, we only observed a slight, though consistent, growth defect in iron-limited conditions (Supplementary Fig. 10). The slight phenotype, which could not be complemented, may be due to laboratory growth conditions, a secondary mutation, or functional redundancy in the iron homeostasis network in *D. magneticus*. Meanwhile, during anaerobic growth in iron-limited conditions elicited with the iron chelator EDTA, the Δ*fez*$_{Sp}$ mutant had a significantly longer lag time compared to WT *S. putrefaciens* (Fig. 7a). To show that this phenotype was due to iron limitation, we rescued the phenotype by adding equimolar concentrations of iron (Fig. 7b). The complementation strain, Δ*fez*$_{Sp}$ / *fez*$_{Sp}^{+}$, had a significantly shorter lag time than WT *S. putrefaciens* when grown with EDTA (Fig. 7a). Overall, these results mirror that of the ferritin mutant phenotype reported for *E. coli* during aerobic growth (171). Therefore, we propose that ferrosomes likely function to store iron during anaerobic metabolism.

In support of the hypothesis that ferrosomes function to store iron, we mined the literature and databases for references to *fez* genes. Transcriptomic and proteomic studies in multiple bacteria suggest that *fez* gene expression is upregulated in low iron environments, including during infection in *Clostridium difficile* (172–175). *D. vulgaris* Hildenborough *fez* gene expression is also induced by high hydrogen sulfide concentrations and oxygen exposure, both situations in which iron can be limiting for sulfate-reducing microorganisms (176–178). Similarly, in a *D. alaskensis* G20 transposon mutant pool, the *fezP1** mutant had attenuated growth in a sulfidogenic sediment community (179). For the facultative anaerobe *R. palustris*, *fez* genes are regulated by oxygen-sensing regulators in strains CGA009 and TIE-1 (180, 181). Based on these previous results and our results here, we propose that ferrosomes have a broad role in anaerobic iron homeostasis.

In summary, we have found the genetic requirement for ferrosomes and provide evidence that ferrosomes function as an iron storage organelle during anaerobic metabolism. Our finding that membrane proteins are associated with and required for ferrosomes supports two independent studies that found membranes surrounding ferrosomes (50, 106). While most P_{1B}-ATPases maintain metal homeostasis by exporting excess metals from the cytoplasm out of the cell, we propose that FezP has a unique function of transporting iron into ferrosomes. Further studies are needed to elucidate how and when ferrosome membranes form and the functions of the different ferrosome proteins. Finally, to determine if this class of organelles is conserved and not confined to iron storage, genes encoding proteins related to those identified in this study should be explored in other bacteria that make membrane-enclosed granules (182, 183).

METHODS

Strains, media, and, growth conditions

The bacterial strains used in this study are listed in Supplementary Table 2. All aerobic cultures were grown with continuous shaking at 250 rpm. Anaerobic cultures were grown at 30°C in an anaerobic glovebox or in sealed Balch tubes with a N_2 headspace containing

medium that was degassed with N_2, unless otherwise stated. Ferrous iron stocks were prepared by dissolving 1 M $FeSO_4$ in 0.1 N HCl and subsequently stored in an anaerobic glovebox. Stocks of ferric malate were prepared as 20 mM $FeCl_3$/60 mM malate. If needed, nitrilotriacetic acid (NTA) disodium salt was added to the ferrous iron to prevent precipitation of iron in the growth medium. NTA alone did not affect cellular growth.

D. magneticus strains were grown at 30°C anaerobically in RS-1 growth medium (RGM), as described previously (50, 52). For growth in iron replete medium, 100 μM ferric malate was added to RGM prior to inoculation. For growth in iron limited medium, iron was omitted from RGM and all glassware was washed with oxalic acid for 24 hours, as described previously (50). To induce ferrosome formation, cells were grown anaerobically in iron-limited RGM. When the cells were in log-phase (OD_{650} ~0.1), ferric malate was added to the cultures at a concentration of 100 μM, unless otherwise stated.

S. putrefaciens strains were grown aerobically at 30°C in Luria-Bertani (LB) broth or anaerobically at 30°C in LB broth supplemented with 10 mM lactate and 10 mM fumarate or 40 mM hydrous ferric oxide (HFO). HFO was prepared as described previously (106). As needed, 1 mM ferrous iron and 2 mM NTA, 100 μM ferrous iron, or 100 μM ferric malate was added to the anaerobic growth medium.

R. palustris strains were grown at 30°C aerobically in the dark in YP medium (0.3% yeast extract and 0.3% peptone) or anaerobically in photoheterotrophic medium (PM) supplemented with 10 mM succinate (PMS-10), as described previously (184). Anaerobic cultures were incubated in a growth chamber with constant light (100 μE of photosynthetically active radiation). As needed, 1 mM ferrous iron was added to the anaerobic growth medium. Because *R. palustris* can oxidize ferrous iron, 3.4 mM citrate trisodium dihydrate was also added to prevent ferric iron precipitates from accumulating in the growth medium.

D. alaskensis G20 strains were grown anaerobically at 37°C in MO basal medium with 60 mM lactate and 30 mM sulfate (MOLS), as described previously (185). The *D. alaskensis* G20 transposon mutants were selected on 1.5% MOLS agar plates containing 400 μg/ml G418. Transposon insertions were confirmed using the primers listed in Supplementary Table 4, as described previously (170).

E. coli strains were grown aerobically at 37°C in LB or anaerobically at 30°C in M9 minimal medium supplemented with 0.4% glucose and 10 mM fumarate. For anaerobic growth, 285 μM L-cysteine was added as a reducing agent. As needed, the anaerobic medium was supplemented 1 mM ferrous iron and 2 mM NTA or 2 mM NTA.

Antibiotics and selective reagents used are as follows: kanamycin (50 μg/mL for *E. coli* and *S. putrefaciens* strains, 125 μg/ml for *D. magneticus*, and 200 μg/ml for *R. palustris*), streptomycin (50 μg/ml for *E. coli* and *D. magneticus* strains), diaminopilmelic acid (DAP)

(300 μM for *E. coli* WM3064), G418 (400 μg/ml for *D. alaskensis* strains) and sucrose (10% for *R. palustris* and *S. putrefaciens*, 1% for *D. magneticus*).

Plasmids and cloning

Plasmids used in this study are listed in Supplementary Table 3. In-frame deletion vectors targeting fez_{Rp} and fez_{Sp} were constructed by amplifying upstream and downstream homology regions from *R. palustris* CGA009 and *S. putrefaciens* CN-32 genomic DNA, respectively, using the primers listed in Supplementary Table 4. The homology regions were then inserted into the SpeI site of pAK31 using the Gibson cloning method. The deletion vector for $fezPC_{Dm}$ was constructed by amplifying upstream and downstream homology regions from *D. magneticus* AK80 genomic DNA using the primers listed in Supplementary Table 4. The P_{npt}-*strAB* cassette was subsequently ligated between the upstream and downstream homology regions of the deletion vector via BamHI. Expression plasmids for fez_{Rp} and fez_{Sp} were constructed by amplifying the respective gene cluster using the primers listed in Supplementary Table 4. The amplified DNA was inserted into HindIII/SpeI-digested pAK22 via the Gibson cloning method. The Δ$fezPC_{Dm}$ complementation vector was constructed by amplifying the P_{fez}-*fezAPC* gene cluster from *D. magneticus* genomic DNA using the primers listed in Supplementary Table 4. The amplified DNA was then ligated into the SalI/XbaI sites of the expression vector pBMK7.

Plasmids were transformed into *E. coli* WM3064 and then transferred to *D. magneticus*, *S. putrefaciens*, or *R. palustris* via conjugation. For *D. magneticus*, the conjugations and gene deletion were performed as described previously (52, 163). Attempts to delete $fezAPC_{Dm}$ were unsuccessful. For conjugal transfer of plasmids to *R. palustris*, strains were streaked onto 1.5% YP agar plates and incubated aerobically at 30°C for 5 days. Two to three days prior to conjugation, single colonies were inoculated into YP medium and incubated aerobically at 30°C, until an OD_{660} of 0.2-0.7. Mid-log cultures of *E. coli* WM3064 carrying the plasmid to be transferred were mixed with *R. palustris* and spotted on 1.5% YP agar plates containing 0.3 mM DAP. After 2-3 days of incubation at 30°C, transconjugants were selected on 1.5% YP plates containing 200 μg/ml kanamycin. For conjugal transfer of plasmids to *S. putrefaciens*, overnight cultures of *E. coli* WM3064 carrying the plasmid to be transferred and *S. putrefaciens* were mixed and spotted on 1.5% LB containing 0.3 mM DAP and incubated aerobically at 30°C for 1 day. Transconjugants were selected with 50 μg/ml kanamycin. Δfez_{Rp} and Δfez_{Sp} candidates were selected on 10% sucrose plates, screened for kanamycin sensitivity, and deletions were confirmed by PCR.

Growth phenotype

For low iron growth, *D. magneticus* strains were inoculated in iron replete RGM, passaged 1:100 to iron limited RGM and then inoculated 1:400 into anaerobic bottles containing iron limited RGM. For iron replete growth, strains were inoculated in iron replete RGM and then passaged 1:100 into iron replete RGM. Growth was measured spectrophotometrically at an optical density of 650 nm (OD_{650}).

For *S. putrefaciens*, colonies were inoculated in anaerobic LB supplemented with lacate, fumarate, and 100 μM ferrous iron. Stationary phase cultures were then passaged 1:200 into anaerobic LB supplemented with lactate, fumarate, and 0 μM or 100 μM EDTA. For iron rescuing of the phenotype, the experiment was as above except that ferrous iron was omitted from the preculture and instead was supplemented to the anaerobic medium during the experiment. Cells were incubated at 30°C and growth was monitored in a Sunrise microplate reader (Tecan) inside the anaerobic glovebag.

Ferrosome isolation

D. magneticus was grown anaerobically in RGM containing no added iron. Cells were then passaged 1:400 in two liters of anaerobic iron limited RGM, as described above. When the culture reached an OD_{650} ~0.1, 100 μM ferric malate was added. After three hours, cells were pelleted at 8,000xg for 20 minutes and flash froze in liquid nitrogen before storing at -80°C. Samples were observed by TEM before and after the addition of iron to ensure ferrosomes had formed. We found that this method enriches for both ferrosomes and magnetosomes (Supplementary Figure 2a-c). In order to prevent contamination with magnetosomes and magnetosome proteins, we isolated ferrosomes from *D. magneticus* ΔMAI and prepared the samples for proteomics.

Cell pellets were thawed on ice and resuspended in LyA buffer (10 mM Tris HCl pH 8.0, 50 mM NaCl, and 1 mM EDTA) containing 250 mM sucrose, leupeptin, pepstatin, and PMSF. Cells were lysed by passing through a French press with a pressure of 1100 psi three times. The lysate was then passed through a 0.2 μm filter to remove unlysed cells. The filtered cell lysate was gently layered over a 65% sucrose cushion and centrifuged at 35,000 rpm at 4°C for 2h. The resulting pellet was resuspended in 1 ml of LyA supplemented with leupeptin, pepstatin, and PMSF, filtered through a 0.2 μM filter, and washed two times with LyA before resuspending in a final volume of 50 μl.

Liquid Chromatography-Electrospray Ionization-Mass Spectrometry

Isolated ferrosomes and whole cell lysate (50 μg) were prepared for liquid chromatography-electrospray ionization-mass spectrometry (LC-ESI/MS). Each sample was combined with 0.06% RapiGest SF surfactant (Waters Corporation, Milford, MA) and 12 mM NH_4CO_3 pH 7.5 at 80°C for 15 minutes. Samples were incubated with 2.9 mM dithiothreitol at 60°C for 30 minutes followed by addition of 7.9 mM iodoacetamide (Sigma-Aldrich, St. Louis, MO) at room temperature for 30 minutes. Samples were then digested with 1:50 trypsin-protein (Promega) at 37°C overnight in the dark. Following digestion, 0.5% trifluoroacetic acid (Sequanal Grade, Thermo Fisher Scientific) was added and incubated at 37°C for 90 minutes to hydrolyze the RapiGest. The samples were centrifuged at 14,000 rpm at 4°C for 30 minutes and the supernatant was tranfered to Waters Total Recovery vial (Waters Corporation, Milford, MA).

Trypsin-digested samples were analyzed using an Acquity M-class liquid chromatograph (LC) that was connected in-line with a Synapt G2-Si high-definition ion mobility mass spectrometer equipped with an electrospray ionization (ESI) source (Waters, Milford,

MA). Mass spectrometry data analysis was performed using Progenesis QI for Proteomics software (Nonlinear Dynamics/Waters, Milford, MA) for relative protein quantification using a label-free approach.

Electron microscopy

Whole-cell transmission electron microscopy was performed as described previously (50).

Multiple sequence alignments and tree construction

To construct the FezP maximum likelihood tree, unique protein sequences were obtained via iterative BLAST searches of DMR_28330 in the IMG Genome Browser. Amino acid sequences were aligned using MUSCLE (7.0.26) and the resulting alignment was trimmed using Gblocks (186). The trimmed alignment was used to generate a phylogeny using RAxML (187) with the LG+G+F model (determined using SMS (188)) and 100 bootstraps. The tree was rooted with a P_{1A}-ATPase, KdpB from *E. coli*, and was visualized and annotated using iTol (189).

Other proteins encoded by *fez* gene clusters were identified by searching the Uniprot database with JACKHMMER on the HMMER web server (190, 191). Three to four aligned sequences, with the ends trimmed if needed, were used for the JACKHMMER search until convergence, or until mosaics of large proteins dominated the returned sequences. The genes were mapped to the genomic regions containing *fezP* using GeneSpy (192). FezP, FezH, FezC, FezD, and FezJ sequences were aligned using Clustal Omega (1.2.4) to identify conserved domains. Hydrophobic domains were mapped using TOPCONS 1.0 (193). For the GxxxG motif-containing proteins, a Clustal Omega alignment was used to generate a logo to show the consensus sequence(s) of each protein (194). Because the FezF JACKHMMER search returned sequences that included MamC, we made a multiple sequence alignment using MUSCLE (7.0.26). This alignment was then used to generate a maximum likelihood phylogeny tree (model LG+G+F predicted using SMS (188)) in MEGA (195). The tree was rooted with a sequence that did not meet the threshold during the JACKHMMER search.

FIGURES

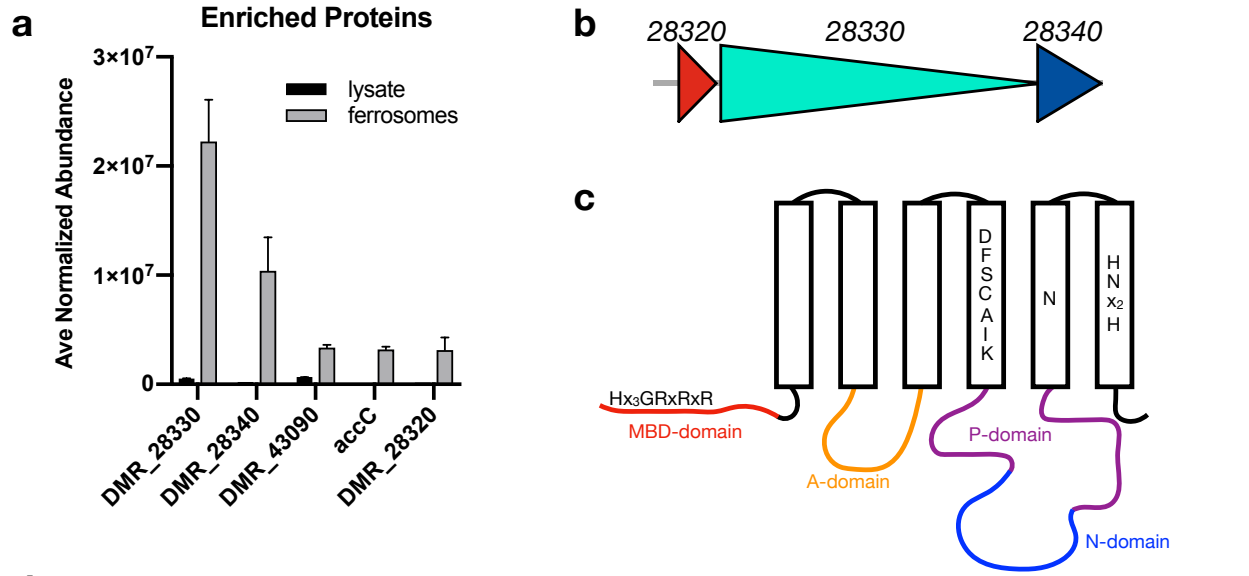

d

```
FezC (DMR_28340) MIASCIEGRIRFRHPALSDPEL-LEIVTSQLAAMPGITEIEANPRTGSVLVSHDASVATSDLVAMAEALAATHAE 74
FezP (DMR_28330) AIVHDIPGRMRLRFACAEAFSAQAPALAAAAVSLSGVAEVIPSPRTLGLLVLYSGDPVRLALLAMTKNGDSAKSA 84
CtpC (Rv3270)    EVVSDAAGRMRVKVDWVRCDSRRAVAVEEAVAKQNGVRVVHAYPRTGSVVVWYSPRRADRAAVLAAIKGAAHVAA 78
```

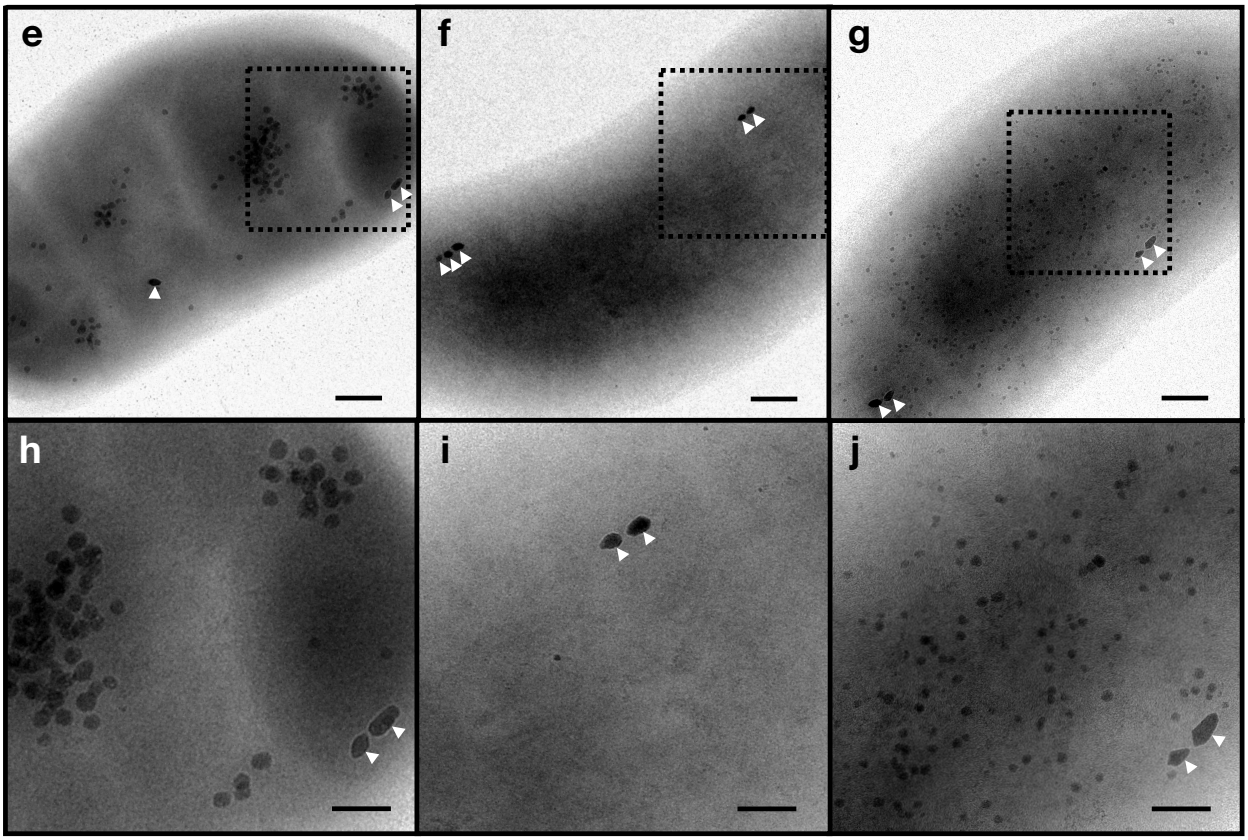

Figure 1. Proteins enriched with ferrosomes isolated from *D. magneticus* are essential for ferrosome formation. (a) Proteins enriched with ferrosomes were identified through comparison of the average normalized abundance of proteins associated with isolated ferrosomes with the whole cell lysate, as detected by LC-ESI/MS. (b) Three proteins that were highly enriched with isolated ferrosomes are encoded by genes that are arranged in a putative operon, *fezAPC*. (c) Schematic of FezP. FezP has the conserved A-, P-, and N-domains of all P_{1B}-ATPases and six putative transmembrane domains (rectangles), as predicted with TOPCONS 1.0. Conserved motifs found in the N-terminal domain and transmembrane domains 4-6, which may be involved in metal binding and transport, are shown. Details of this schematic are based on the alignments shown in Supplementary Figures 2 and 3. (d) The N-terminal domains of FezP, FezC, and CtpC have homology and contain a conserved R-rich motif. Residues conserved in the three sequences are highlighted green and residues conserved in two of the three sequences are highlighted gray. (e) Transmission electron micrographs of *D. magneticus* after transitioning out of iron starvation. WT *D. magneticus* (e, h) has visible ferrosomes that are not found in the Δ*fezPC*$_{Dm}$ strain (f, i). Complementation with *fezAPC* expressed in *trans* rescues the phenotype (g, j). Micrographs in h-j are insets of e-g. White carets indicate magnetosomes. Scale bars, 200 nm; insets, 100 nm.

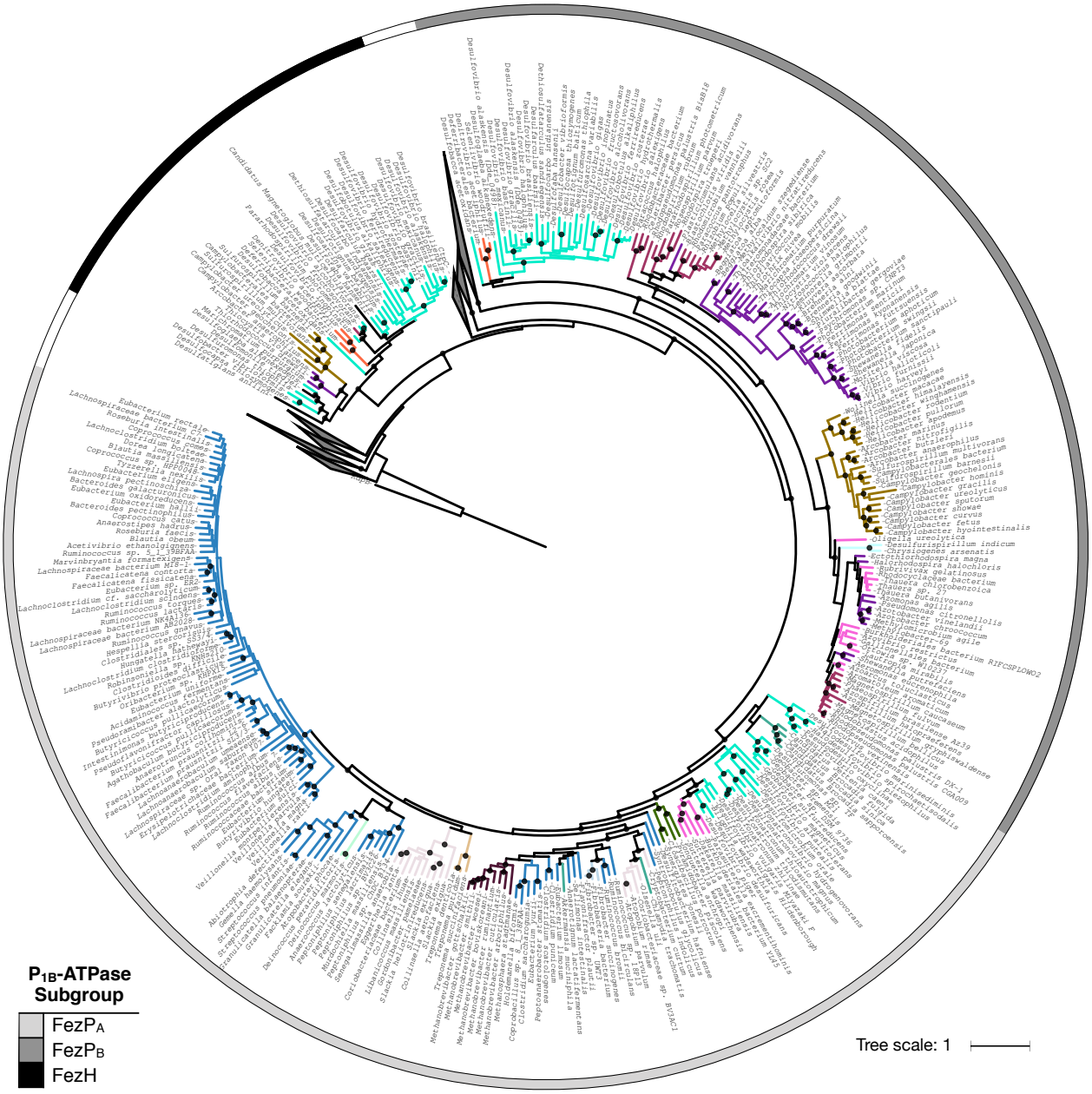
P1B-ATPase Subgroup
FezPA
FezPB
FezH
Tree scale: 1
Phylum
Gammaproteobacteria
Betaproteobacteria
Alphaproteobacteria
Epsilonproteobacteria
Spirochaetes
Deferribacteres
Chrysiogenetes
Deltaproteobacteria
PVC Superphylum
Fibrobacteres
Deinococcus-Thermus
Synergistetes
Firmicutes
Actinobacteria
Methanobacteria

Figure 2. Maximum likelihood tree of FezP and related proteins. FezP forms two clear clades that are depicted with the light gray color strip ($FezP_A$) and the dark grey color strip ($FezP_B$). FezH, which is most closely related to CtpC, is indicated with the black color strip. Branch colors indicate the phylum or superphylum of organisms that have a FezP homolog. Clades containing proteins that are not encoded in *fez* gene clusters are collapsed and have white color strips. The tree was rooted with a P_{1A}-ATPase, KdpB, from *E. coli*. Bootstraps >70% are indicated with black circles.

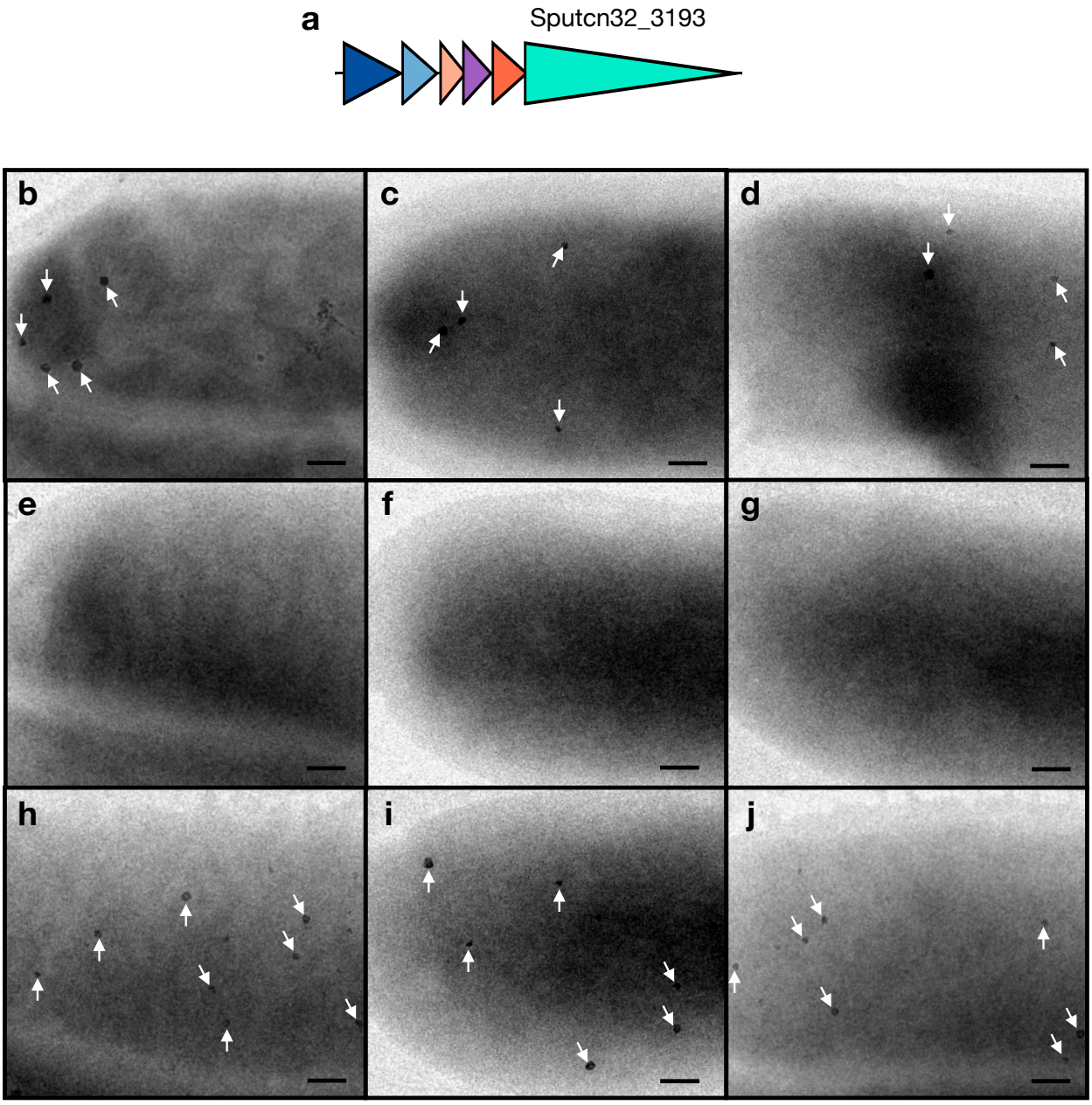

Figure 3. *fez* genes are essential for *S. putrefaciens* to make ferrosomes. (a) *S. putrefaciens* has a *fez* gene cluster that is distinct from *D. magneticus*. (b-j) Transmission electron micrographs of *S. putrefaciens* strains respiring hydrous ferric oxide (HFO) (b, e, h) or fumarate in medium supplemented with 100 μM ferric malate (c, f, i) or 1 mM ferrous iron (d, g, j). WT *S. putrefaciens* makes ferrosomes visible by TEM (b-d) that are not found in the Δfez_{Sp} strain (e-g). The complementation strain, Δfez_{Sp} / fez_{Sp}^{+}, makes visible ferrosomes (h-j). White arrows indicate ferrosomes. Scale bars, 100 nm.

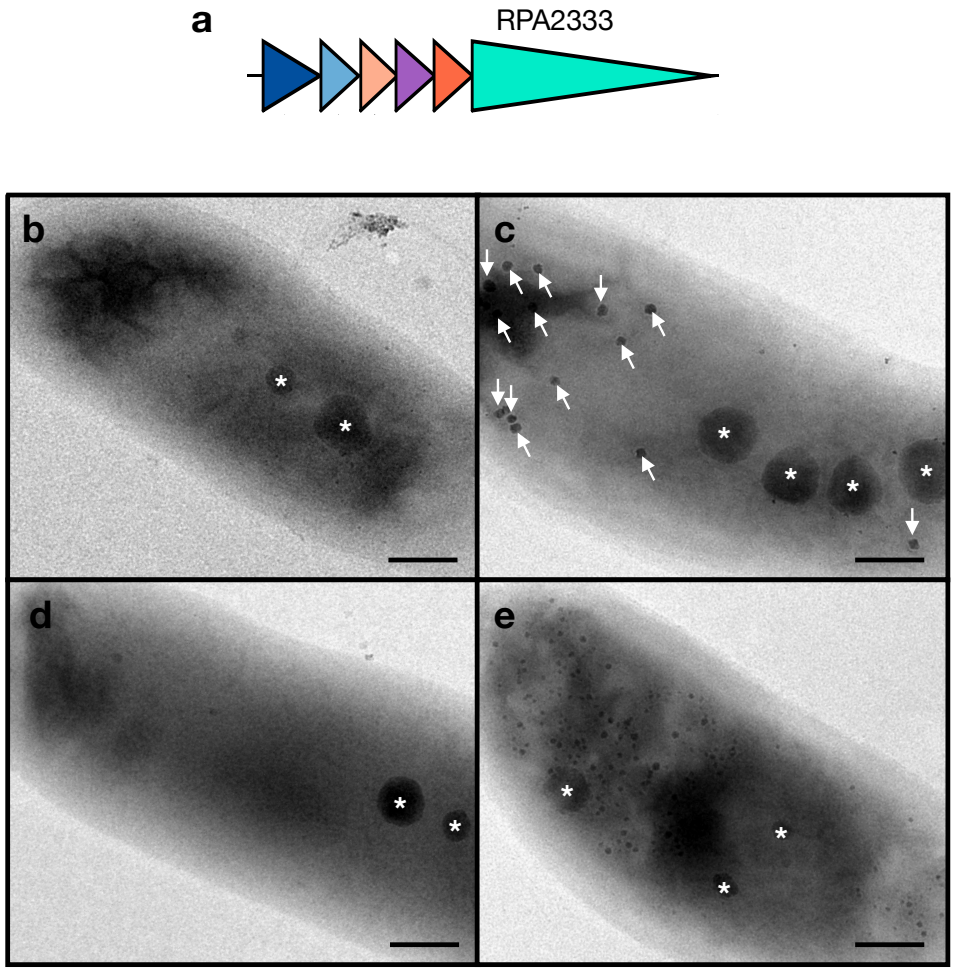

Figure 4. *fez* genes are essential for *R. palustris* to make ferrosomes. (a) *R. palustris* has a *fez* gene cluster that is similar to *S. putrefaciens*. (b-e) Transmission electron micrographs of *R. palustris* CGA009. *R. palustris* CGA009 forms ferrosomes (white arrows) when grown anaerobically (c) and not aerobically (b). Deletion of the fez_{Rp} gene cluster abolishes ferrosome formation (d), a phenotype that can be complemented (e). Polyphosphate granules are indicated with a white asterisk. Scale bars, 200 nm.

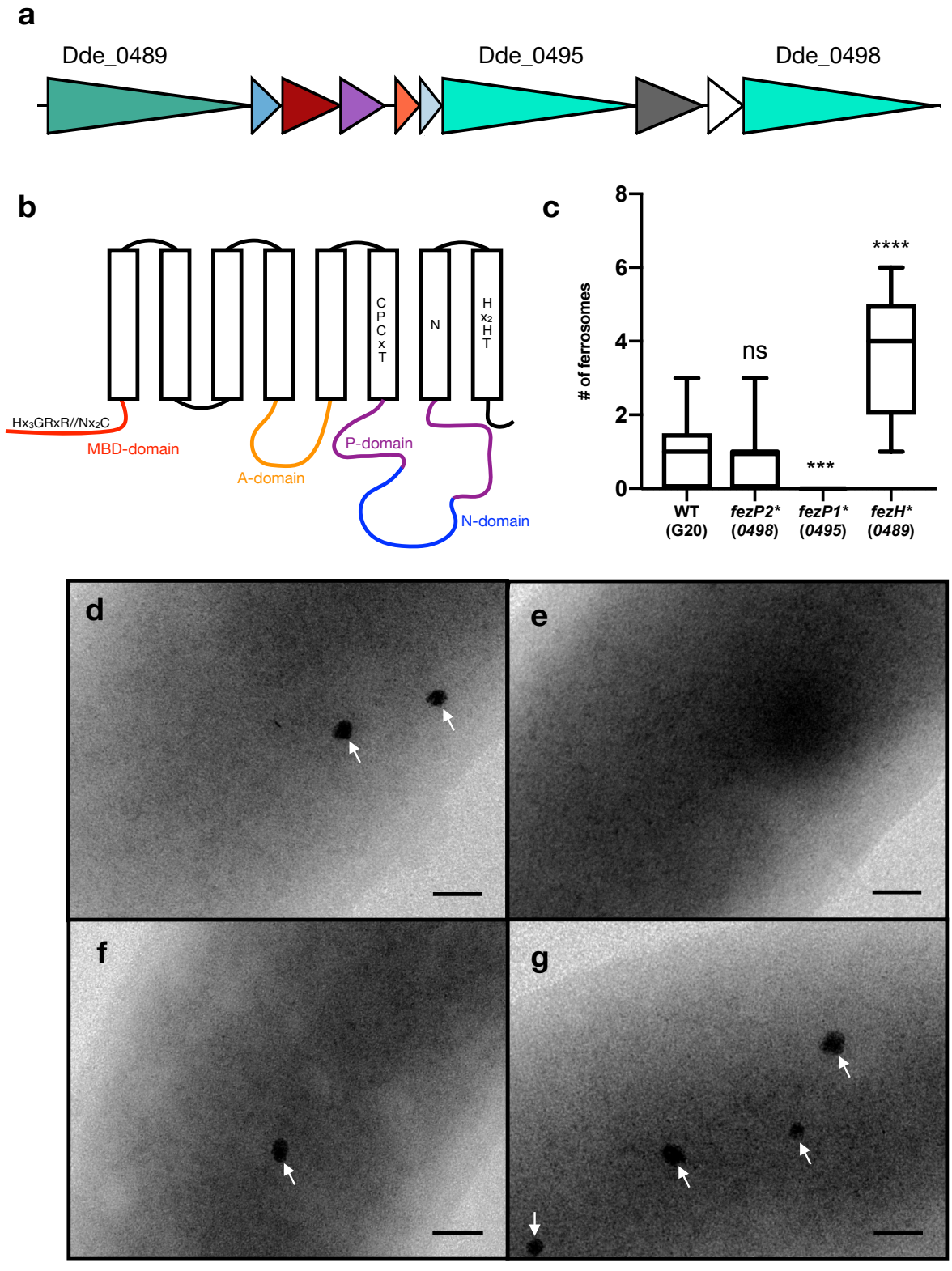
a
Dde_0489
Dde_0495
Dde_0498
b
CPCxT
N
Hx2HT
Hx3GRxR//Nx2C
MBD-domain
A-domain
P-domain
N-domain
c
# of ferrosomes
8
6
4
2
0
ns
***
****
WT (G20)
fezP2* (0498)
fezP1* (0495)
fezH* (0489)
d
e
f
g

Figure 5. FezP1 and FezH affect ferrosome formation in *D. alaskensis*. (a) *D. alaskensis* has a larger *fez* gene cluster with three P_{1B}-ATPases. (b) Schematic of FezH. Like FezP, FezH has the conserved domains of P_{1B}-ATPases. FezH has 8 putative transmembrane domains (rectangles), as predicted with TOPCONS 1.0. The N-terminal domain contains an R-rich motif, similar to FezP. Conserved motifs that may be involved in metal binding in transmembrane domains 6-8 are shown. Details of this schematic are based on the alignments shown in Supplementary Figure 9. (d-g) Transmission electron micrographs of *D. alaskensis* WT (d), *fezP1** (e), *fezP2** (f), and *fezH** (g). All strains make ferrosomes that are visible by TEM, except the *fezP1** mutant (c, e). The *fezH** mutant appears to make significantly more ferrosomes than WT (c, g). The box plot graph shows the number of ferrosomes per cell in each of the *D. alaskensis* strains: G20 (n=21), *fezP2** (Dde_0498) (n=23); *fezP1** (Dde_0495) (n=14); *fezH** (Dde_0489) (n=21). Statistical significance of the mutants compared to WT was determined using the Mann-Whitney test. ns, not significant; ***, p=0.0001; ****, p<0.0001. (B-E) White arrows indicate ferrosomes. Scale bars, 100 nm.

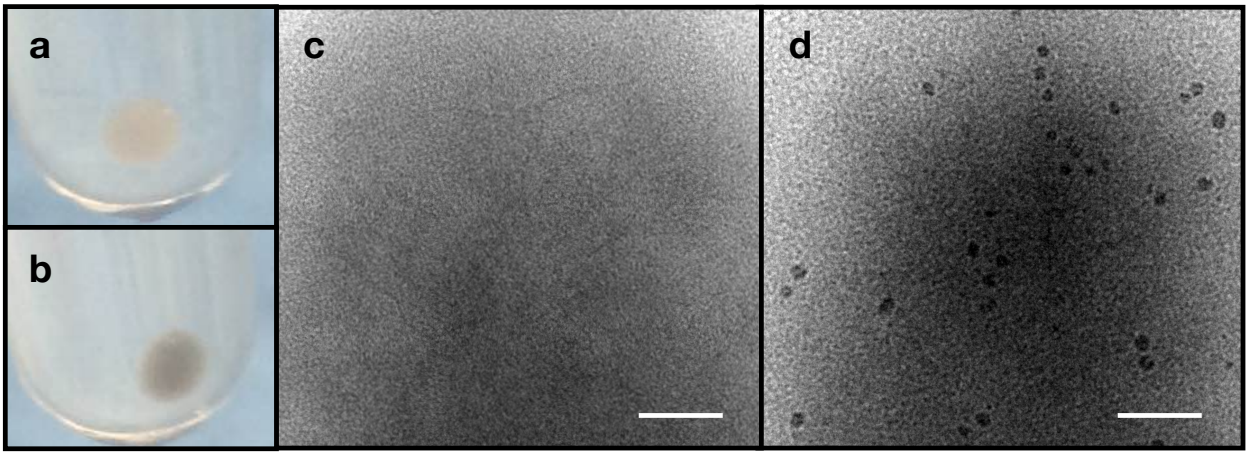

Figure 6. *E. coli* makes ferrosomes when expressing the *S. putrefaciens fez* genes heterologously. *E. coli* / fez_{Sp}^{+} has a visibly dark cell pellet when grown anaerobically in growth medium supplemented with iron (b). (c, d) Transmission electron micrographs of *E. coli* strains grown anaerobically in growth medium supplemented with iron show electron-dense granules in *E. coli* / fez_{Sp}^{+} (d). No granules are visible in *E. coli* harboring a control plasmid (c), which has a white cell pellet (a). Scale bars, 100 nm.

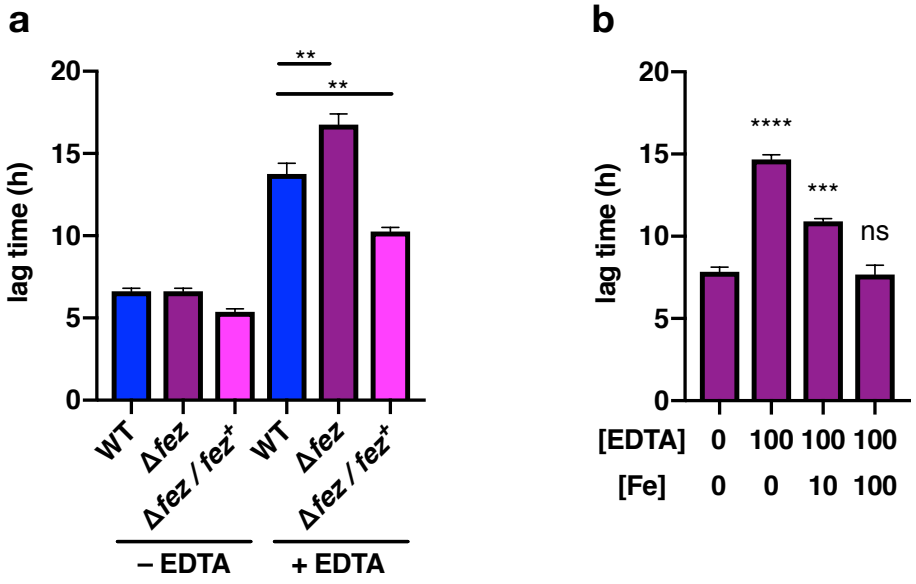

Figure 7. *S. putrefaciens Δfez*$_{Sp}$ mutant has a growth defect in iron limited medium. (a) The *S. putrefaciens Δfez*$_{Sp}$ mutant has a significant longer lag phase when grown in growth medium supplemented with the chelator EDTA (100 μM). Complementation of the mutant rescues the phenotype. (b) Adding back equimolar amounts of iron (100 μM ferrous iron) rescues the phenotype. EDTA (100 μM) and/or ferrous iron (10 μM or 100 μM) were added to the growth medium. Data presented are averages of 3 independent cultures; error bars indicate the standard deviations. Statistical significance determined using Welch's t-test. ns, not significant; **, $p<0.01$; ***, $p<0.001$; ****, $p<0.0001$.

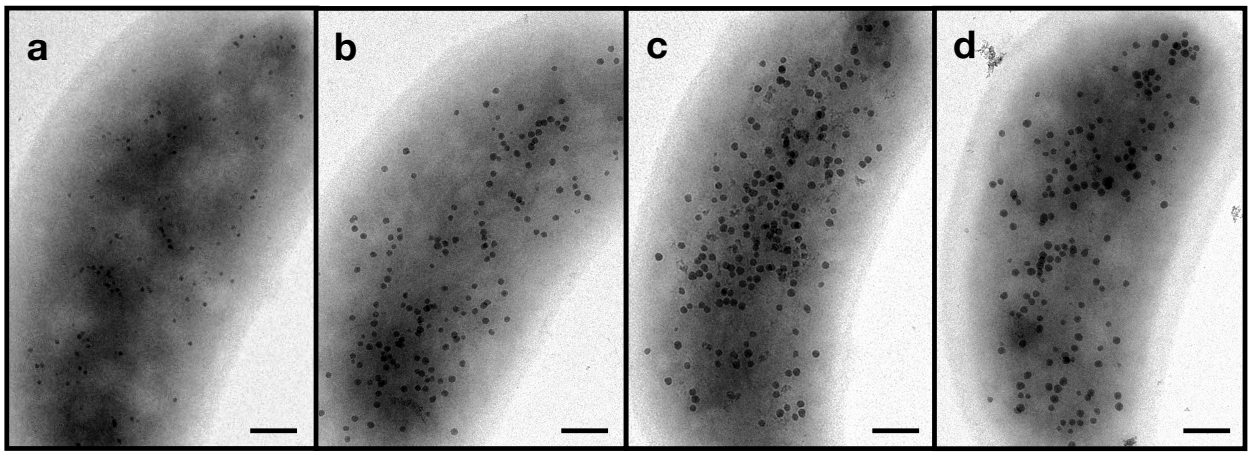

Supplementary Figure 1. Ferrosomes are visible by TEM in whole D. magneticus cells after transitioning from iron limited to iron replete conditions. In *D. magneticus*, ferrosomes are visible one hour after addition of 1 μM (a), 10 μM (b), 100 μM (c), and 1 mM (d) ferric malate to iron-starved cells. Scale bars, 200 nm.

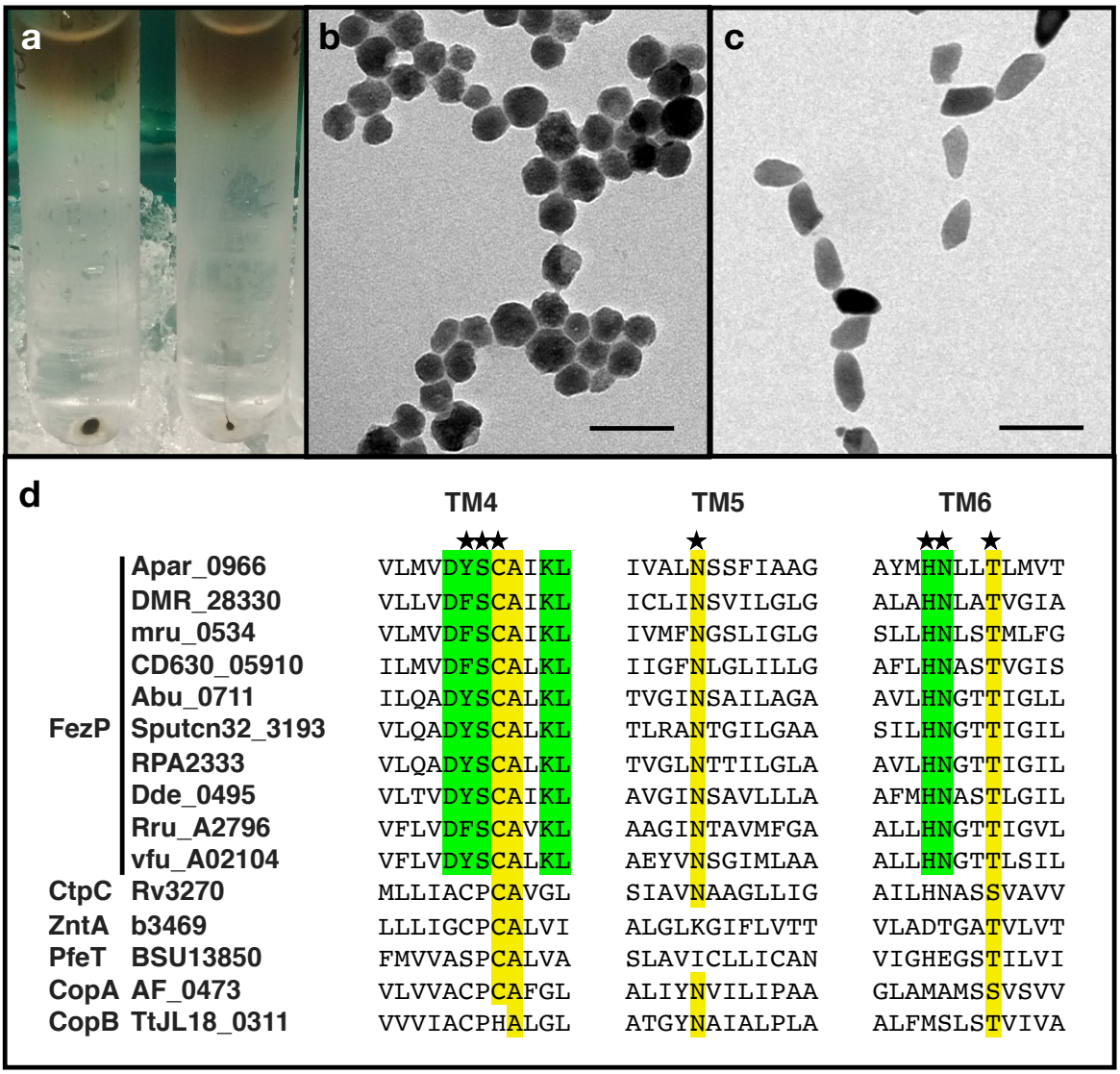

Supplementary Figure 2. Isolation of ferrosomes and unique metal-binding sites of FezP. (a) Ferrosomes were isolated from WT *D. magneticus* cells that had transitioned from iron limited to iron replete medium by filtering whole cell lysate through a 65% sucrose cushion (left). A pellet is visible at the bottom of the sucrose cushion that contains ferrosomes, as confirmed by TEM (b). Magnetosomes were isolated from WT *D. magneticus* cells grown in iron replete medium using the same procedure (a, right; c). (b, c) Scale bars, 100 nm. (d) FezP has a conserved DYSCAxKL motif in the fourth transmembrane domain (TM4). A previous study identified the P_{1B-6}-ATPase TM4 motif as SCA (164). Here, we note that [Y/F]SC aligns with the metal binding sites, CPC and CPH, of the characterized P_{1B}-ATPases. Additionally, a conserved HNxx[S/T] motif is found in TM6 that has not been identified previously. Black stars indicate residues that align with known metal coordinating residues. Residues conserved in FezP are highlighted green and residues conserved in most P_{1B}-ATPases are highlighted yellow.

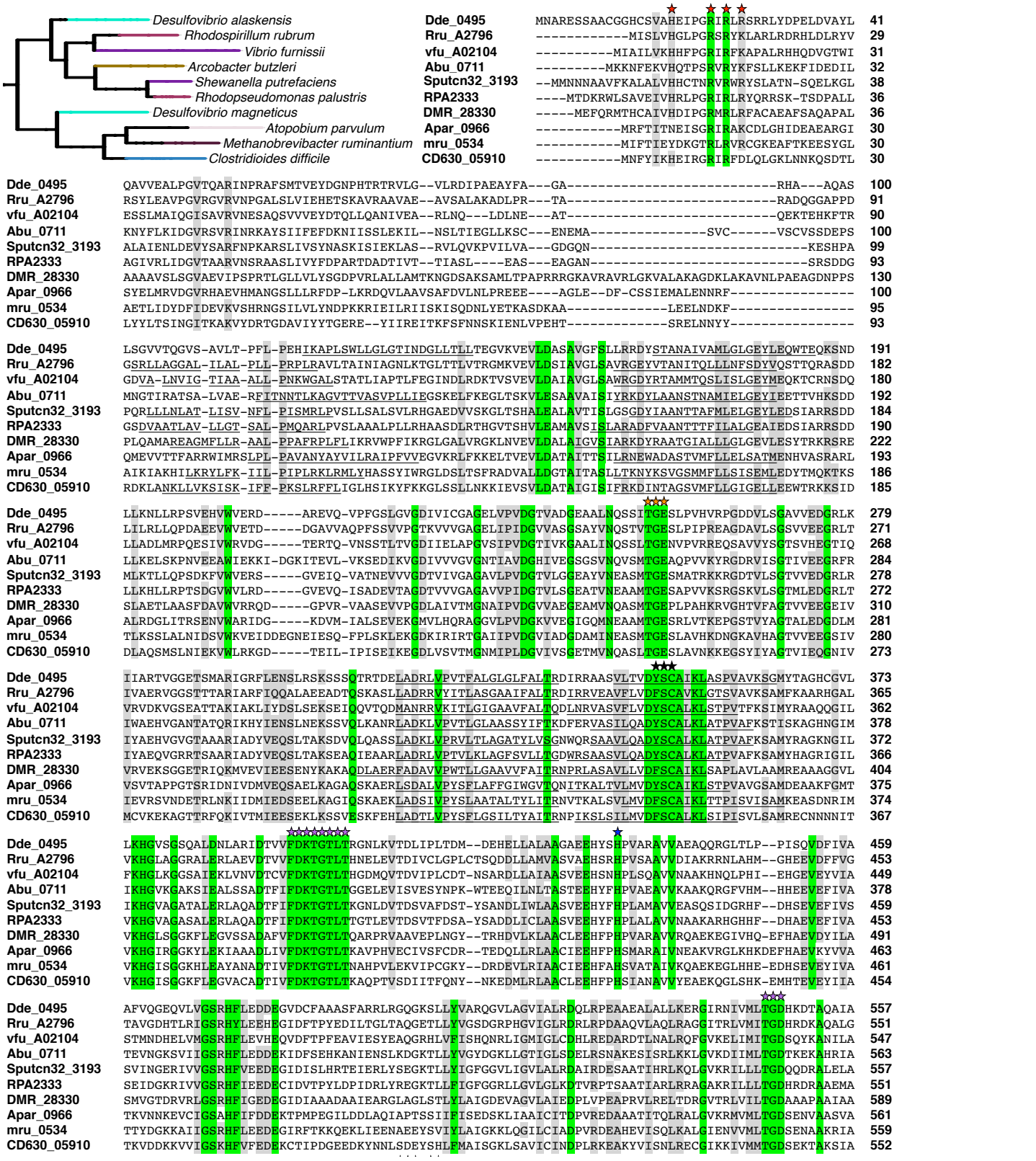
Desulfovibrio alaskensis
Rhodospirillum rubrum
Vibrio furnissii
Arcobacter butzleri
Shewanella putrefaciens
Rhodopseudomonas palustris
Desulfovibrio magneticus
Atopobium parvulum
Methanobrevibacter ruminantium
Clostridioides difficile
Dde_0495 MNARESSAACGGHCSVAHEIPGRIRLRSRRLYDPELDVAYL 41
Rru_A2796 ----------MISLVHGLPGRSRYKLARLRDRHLDLRYV 29
vfu_A02104 ----------MIAILVKHHFPGRIRFKAPALRHHQDVGTWI 31
Abu_0711 ---------MKKNFEKVHQTPSRVRYKFSLLKEKFIDEDIL 32
Sputcn32_3193 --MMNNNAAVFKALALVHHCTNRVRWRYSLATN-SQELKGL 38
RPA2333 ----MTDKRWLSAVEIVHRLPGRIRLRYQRRSK-TSDPALL 36
DMR_28330 -----MEFQRMTHCAIVHDIPGRMRLRFACAEAFSAQAPAL 36
Apar_0966 ----------MRFTITNEISGRIRAKCDLGHIDEAEARGI 30
mru_0534 ----------MIFTIEYDKGTRLRVRCGKEAFTKEESYGL 30
CD630_05910 ----------MNFYIKHEIRGRIRFDLQLGKLNNKQSDTL 30
Dde_0495 QAVVEALPGVTQARINPRAFSMTVEYDGNPHTRTRVLG--VLRDIPAEAYFA---GA----------RHA---AQAS 100
Rru_A2796 RSYLEAVPGVRGVRVNPGALSLVIEHETSKAVRAAVAE--AVSALAKADLPR---TA----------RADQGGAPPD 91
vfu_A02104 ESSLMAIQGISAVRVNESAQSVVVEYDTQLLQANIVEA--RLNQ---LDLNE---AT----------QEKTEHKFTR 90
Abu_0711 KNYFLKIDGVRSVRINRKAYSIIFEFDKNIISSLEKIL--NSLTIEGLLKSC---ENEMA----------SVC------VSCVSSDEPS 100
Sputcn32_3193 ALAIENLDEVYSARFNPKARSLIVSYNASKISIEKLAS--RVLQVKPVILVA---GDGQN----------KESHPA 99
RPA2333 AGIVRLIDGVTAARVNSRAASLIVYFDPARTDADTIVT--TIASL----EAS---EAGAN----------SRSDDG 93
DMR_28330 AAAAVSLSGVAEVIPSPRTLGLLVLYSGDPVRLALLAMTKNGDSAKSAMLTPAPRRRGKAVRAVRLGKVALAKAGDKLAKAVNLPAEAGDNPPS 130
Apar_0966 SYELMRVDGVRHAEVHMANGSLLLRFDP-LKRDQVLAAVSAFDVLNLPREEE----AGLE--DF-CSSIEMALENNRF---------- 100
mru_0534 AETLIDYDFIDEVKVSHRNGSILVLYNDPKKRIEILRIISKISQDNLYETKASDKAA----------LEELNDKF---------- 95
CD630_05910 LYYLTSINGITKAKVYDRTGDAVIYYTGERE--YIIREITKFSFNNSKIENLVPEHT----------SRELNNYY---------- 93
Dde_0495 LSGVVTQGVS-AVLT-PFL-PEHIKAPLSWLLGLGTINDGLLTLLTEGVKVEVLDASAVGFSLLRRDYSTANAIVAMLGLGEYLEQWTEQKSND 191
Rru_A2796 GSRLLAGGAL-ILAL-PLL-PRPLRAVLTAINIAGNLKTGLTTLVTRGMKVEVLDSIAVGLSAVRGEYVTANITQLLLNFSDYVQSTTQRASDD 182
vfu_A02104 GDVA-LNVIG-TIAA-ALL-PNKWGALSTATLIAPTLFEGINDLRDKTVSVEVLDAIAVGLSAWRGDYRTAMMTQSLISLGEYMEQKTCRNSDQ 180
Abu_0711 MNGTIRATSA-LVAE-RFITNNTLKAGVTTVASVPLLIEGSKELFKEGLTSKVLESAAVAISIYRKDYLAANSTNAMIELGEYIEETTVHKSDD 192
Sputcn32_3193 PQRLLLNLAT-LISV-NFL-PISMRLPVSLLSALSVLRHGAEDVVSKGLTSHALEALAVTISLGSGDYIAANTTAFMLELGEYLEDSIARRSDD 184
RPA2333 GSDVAATLAV-LLGT-SAL-PMQARLPVSLAAALPLLRHAASDLRTHGVTSHVLEAMAVSISLARADFVAANTTTFILALGEAIEDSIARRSDD 190
DMR_28330 PLQAMAREAGMFLLR-AAL-PPAFRPLFLIKRVWPFIKRGLGALVRGKLNVEVLDALAIGVSIARKDYRAATGIALLLGLGEVLESYTRKRSRE 222
Apar_0966 QMEVVTTFARRWIMRSLPL-PAVANYAYVILRAIPFVVEGVKRLFKKELTVEVLDATAITTSILRNEWADASTVMFLLELSATMENHVASRARL 193
mru_0534 AIKIAKHILKRYLFK-IIL-PIPLRKLRMLYHASSYIWRGLDSLTSFRADVALLDGTAITASLLTKNYKSVGSMMFLLSISEMLEDYTMQKTKS 186
CD630_05910 RDKLANKLLVKSISK-IFF-PKSLRFFLIGLHSIKYFKKGLSSLLNKKIEVSVLDATAIGISIFRKDINTAGSVMFLLGIGELLEEWTRKKSID 185
Dde_0495 LLKNLLRPSVEHVWVERD-----AREVQ-VPFGSLGVGDIVICGAGELVPVDGTVADGEAALNQSSITGESLPVHVRPGDDVLSGAVVEDGRLK 279
Rru_A2796 LILRLLQPDAEEVWVETD-----DGAVVAQPFSSVVPGTKVVVGAGELIPIDGVVASGSAYVNQSTVTGESLPIPREAGDAVLSGSVVEEGRLT 271
vfu_A02104 LLADLMRPQESIVWRVDG-----TERTQ-VNSSTLTVGDIIELAPGVSIPVDGTIVKGAALINQSSLTGENVPVRREQSAVVYSGTSVHEGTIQ 268
Abu_0711 LLKELSKPNVEEAWIEKKI-DGKITEVL-VKSEDIKVGDIVVVGVGNTIAVDGHIVEGSGSVNQVSMTGEAQPVVKYRGDRVISGTIVEEGRFR 284
Sputcn32_3193 MLKTLLQPSDKFVWVERS-----GVEIQ-VATNEVVVGDTVIVGAGAVLPVDGTVLGGEAYVNEASMTGESMATRKKRGDTVLSGTVVEDGRLR 278
RPA2333 LLKHLLRPTSDGVWVLRD-----GVEVQ-ISADEVTAGDTVVVGAGAVVPIDGTVLSGEATVNEAAMTGESAPVVKSRGSKVLSGTMLEDGRLT 272
DMR_28330 SLAETLAASFDAVWVRRQD-----GPVR-VAASEVVPGDLAIVTMGNAIPVDGVVAEGEAMVNQASMTGEPLPAHKRVGHTVFAGTVVEEGEIV 310
Apar_0966 ALRDGLITRSENVWARIDG-----KDVM-IALSEVEKGMVLHQRAGGVLPVDGKVVEGIGQMNEAAMTGESRLVTKEPGSTVYAGTALEDGDLM 281
mru_0534 TLKSSLALNIDSVWKVEIDDEGNEIESQ-FPLSKLEKGDKIRIRTGAIIPVDGVIADGDAMINEASMTGESLAVHKDNGKAVHAGTVVEEGSIV 280
CD630_05910 DLAQSMSLNIEKVWLRKGD-----TEIL-IPISEIKEGDLVSVTMGNMIPLDGVIVSGETMVNQASLTGESLAVNKKEGSYIYAGTVIEQGNIV 273
Dde_0495 IIARTVGGETSMARIGRFLENSLRSKSSSQTRTDELADRLVPVTFALGLGLFALTRDIRRAASVLTVDYSCAIKLASPVAVKSGMYTAGHCGVL 373
Rru_A2796 IVAERVGGSTTTARIARFIQQALAEEADTQSKASLLADRRVYITLASGAAIFALTRDIRRVEAVFLVDFSCAVKLGTSVAVKSAMFKAARHGAL 365
vfu_A02104 VRVDKVGSEATTAKIAKLIYDSLSEKSEIQQVTQDMANRRVKITLGIGAAVFALTQDLNRVASVFLVDYSCALKLSTPVTFKSIMYRAAQQGIL 362
Abu_0711 IWAEHVGANTATQRIKHYIENSLNEKSSVQLKANRLADKLVPVTLGLAASSYIFTKDFERVASILQADYSCALKLATPVAFKSTISKAGHNGIM 378
Sputcn32_3193 IYAEHVGVGTAAARIADYVEQSLTAKSDVQLQASSLADKLVPRVLTLAGATYLVSGNWQRSAAVLQADYSCALKLATPVAFKSAMYRAGKNGIL 372
RPA2333 IYAEQVGRRTSAARIADYVEQSLTAKSEAQIEAARLADRLVPTVLKLAGFSVLLTGDWRSAASVLQADYSCALKLATPVAFKSAMYHAGRIGIL 366
DMR_28330 VRVEKSGGETRIQKMVEVIEESENYKAKAQDLAERFADAVVPWTLLGAAVVFAITRNPRLASAVLLVDFSCAIKLSAPLAVLAAMREAAAGGVL 404
Apar_0966 VSVTAPPGTSRIDNIVDMVEQSAELKAGAQSKAERLSDALVPYSFLAFFGIWGVTQNITKALTVLMVDYSCAIKLSTPVAVGSAMDEAAKFGMT 375
mru_0534 IEVRSVNDETRLNKIIDMIEDSEELKAGIQSKAEKLADSIVPYSLAATALTYLITRNVTKALSVLMVDFSCAIKLTTPISVISAMKEASDNRIM 374
CD630_05910 MCVKEKAGTTRFQKIVTMIEESEKLKSSVESKFEHLADTLVPYSFLGSILTYAITRNPIKSLSILMVDFSCALKLSIPISVLSAMRECNNNNIT 367
Dde_0495 LKHGVSGSQALDNLARIDTVVFDKTGTLTRGNLKVTDLIPLTDM--DEHELLALAAGAEEHYSHPVARAVVAEAQQRGLTLP--PISQVDFIVA 459
Rru_A2796 VKHGLAGGRALERLAEVDTVVFDKTGTLTHNELEVTDIVCLGPLCTSQDDLLAMVASVAEHSRHPVSAAVVDIAKRRNLAHM--GHEEVDFFVG 453
vfu_A02104 FKHGLKGGSAIEKLVNVDTCVFDKTGTLTHGDMQVTDVIPLCDT-NSARDLLAIAASVEEHSNHPLSQAVVNAAKHNQLPHI--EHGEVEYVIA 449
Abu_0711 IKHGVKGAKSIEALSSADTFIFDKTGTLTGGELEVISVESYNPK-WTEEQILNLTASTEEHYFHPVAEAVVKAAKQRGFVHM--HHEEVEFIVA 378
Sputcn32_3193 IKHGVAGATALERLAQADTFIFDKTGTLTKGNLDVTDSVAFDST-YSANDLIWLAASVEEHYFHPLAMAVVEASQSIDGRHF--DHSEVEFIVS 459
RPA2333 VKHGVAGASALERLAQADTFIFDKTGTLTTGTLEVTDSVTFDSA-YSADDLICLAASVEEHYFHPLALAVVNAAKARHGHHF--DHAEVEFIVA 453
DMR_28330 VKHGLSGGKFLEGVSSADAFVFDKTGTLTQARPRVAAVEPLNGY--TRHDVLKLAACLEEHFPHPVARAVVRQAEKEGIVHQ-EFHAEVDYILA 491
Apar_0966 VKHGIRGGKYLEKIAAADLIVFDKTGTLTKAVPHVECIVSFCDR--TEDQLLRLAACIEEHFPHSMARAIVNEAKVRGLKHKDEFHAEVKYVVA 463
mru_0534 VKHGISGGKHLEAYANADTIVFDKTGTLTNAHPVLEKVIPCGKY--DRDEVLRIAACIEEHFAHSVATAIVKQAEKEGLHHE-EDHSEVEYIVA 461
CD630_05910 VKHGISGGKFLEGVACADTIVFDKTGTLTKAQPTVSDIITFQNY--NKEDMLRLAACLEEHFPHSIANAVVYEAEKQGLSHK-EMHTEVEYIIA 454
Dde_0495 AFVQGEQVLVGSRHFLEDDEGVDCFAAASFARRLRGQGKSLLYVARQGVLAGVIALRDQLRPEAAEALALLKERGIRNIVMLTGDHKDTAQAIA 557
Rru_A2796 TAVGDHTLRIGSRHYLEEHEGIDFTPYEDILTGLTAQGETLLYVGSDGRPHGVIGLRDRLRPDAAQVLAQLRAGGITRLVMITGDHRDKAQALG 551
vfu_A02104 STMNDHELVMGSRHFLEVHEQVDFTPFEAVIESYEAQGRHLVFISHQNRLIGMIGLCDHLREDARDTLNALRQFGVKELIMITGDSQYKANILA 547
Abu_0711 TEVNGKSVIIGSRHFLEDDEKIDFSEHKANIENSLKDGKTLLYVGYDGKLLGTIGLSDELRSNAKESISRLKKLGVKDIIMLTGDTKEKAHRIA 563
Sputcn32_3193 SVINGERIVVGSRHFVEEDEGIDISLHRTEIERLYSEGKTLLYIGFGGVLIGVLALRDAIRDESAATIHRLKQLGVKRILLLTGDQQDRALELA 557
RPA2333 SEIDGKRIVVGSRHFIEEDECIDVTPYLDPIDRLYREGKTLLFIGFGGRLLGVLGLKDTVRPTSAATIARLRRAGAKRILLLTGDHRDRAAEMA 551
DMR_28330 SMVGTDRVRLGSRHFIGEDEGIDIAAADAAIEARGLAGLSTLYLAIGDEVAGVLAIEDPLVPEAPRVLRELTDRGVTRLVILTGDAAAPAAIAA 589
Apar_0966 TKVNNKEVCIGSAHFIFDDEKTPMPEGILDDLAQIAPTSSIIFISEDSKLIAAICITDPVREDAAATITQLRALGVKRMVMLTGDSENVAASVA 561
mru_0534 TTYDGKKAIIGSRHFLEEDEGIRFTKKQEKLIEENAEEYSVIYLAIGKKLQGILCIADPVRDEAHEVISQLKALGIENVVMLTGDSENAAKRIA 559
CD630_05910 TKVDDKKVVIGSKHFVFEDEKCTIPDGEEDKYNNLSDEYSHLFMAISGKLSAVICINDPLRKEAKYVISNLRECGIKKIVMMTGDSEKTAKSIA 552

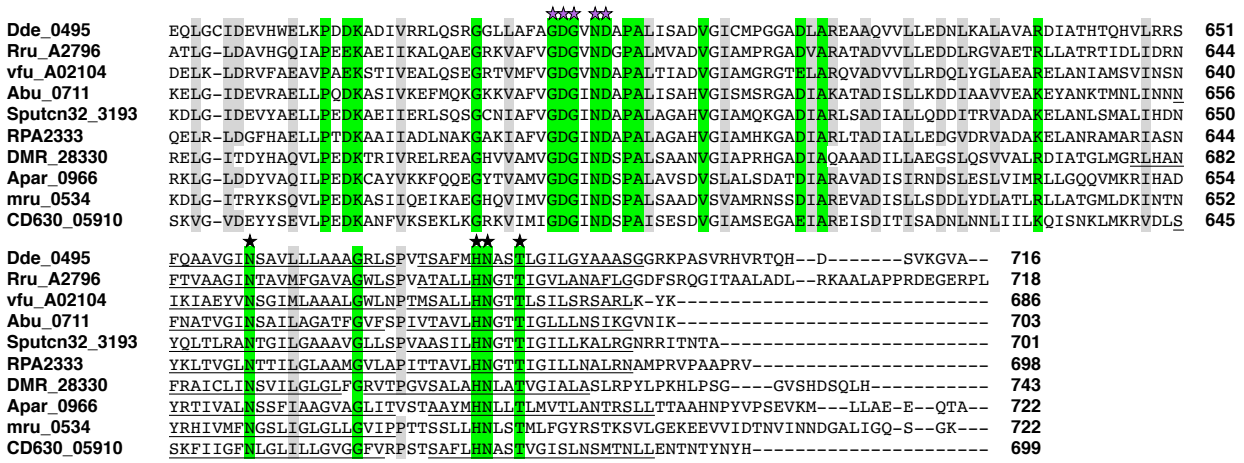

Supplementary Figure 3. Multiple sequence alignment of FezP. The tree, pruned from Fig. 2, shows the proteins from the two subgroups of FezP used for making the Clustal Omega alignment. Conserved functional motifs in the A-, P-, and N-domains are indicated with yellow, purple, and blue stars, respectively. Transmembrane regions, predicted using TOPCONS 1.0, are underlined for each amino acid sequence. Conserved residues in the R-rich motif in the N-terminal domain are indicated with red stars and putative metal-binding sites in transmembrane domains 4-6 are indicated with black stars. Highly conserved residues are highlighted in green and conserved residues are highlighted in gray.

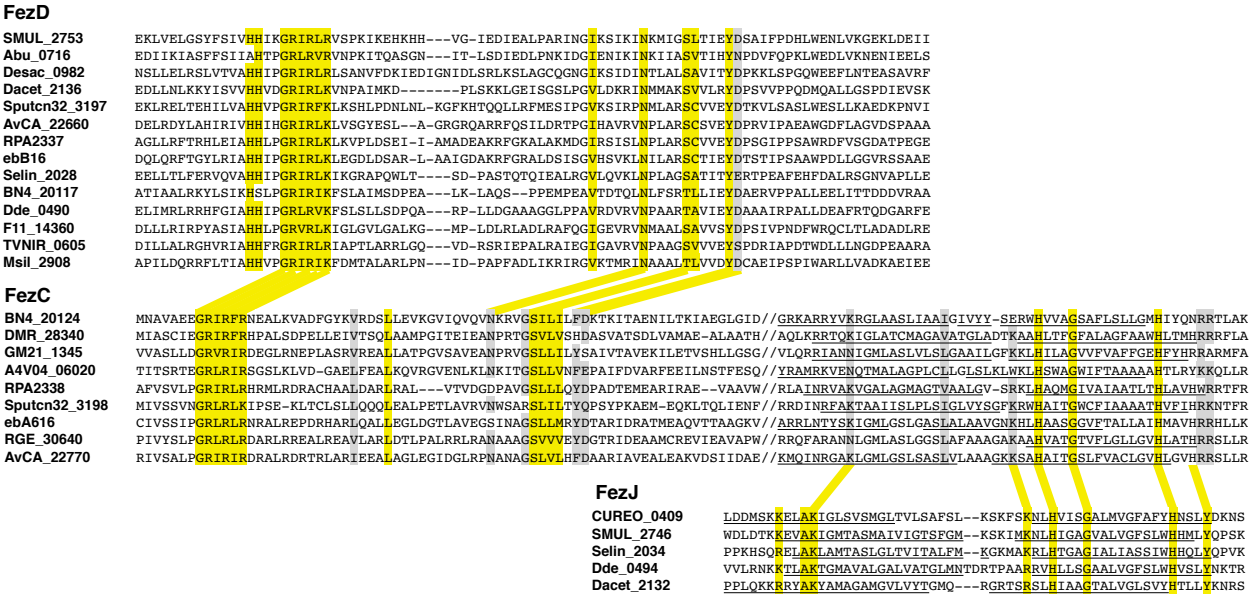

Supplementary Figure 4. Multiple sequence alignment of chaperone-like proteins, FezC, FezD, and FezJ. FezC has an N-terminal domain containing an R-rich motif and the C-terminal end of FezC has two putative transmembrane domains. FezD has an N-terminal domain with homology to FezC, but lacks transmembrane domains. Conversely, FezJ has transmembrane domains with homology to FezC but lacks the N-terminal domain of FezC. Highly conserved residues are highlighted in yellow and conserved residues are highlighted in gray. Yellow lines connect conserved residues between FezC and FezD or FezJ. Transmembrane regions predicted with TOPCONS 1.0 are underlined.

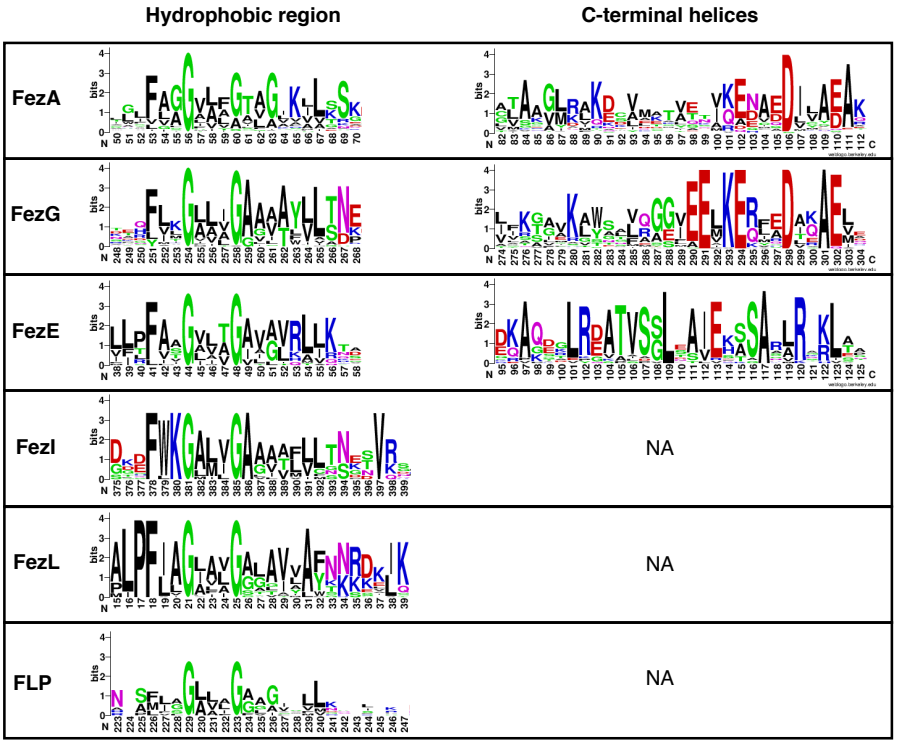

Supplementary Figure 5. GxxxG-motif containing proteins are encoded by *fez* gene clusters. Logos show the consensus sequences in the GxxxG-motif containing proteins. FezA, FezG, and FezE have hydrophobic regions with GxxxG-motifs and conserved C-terminal helices. For many of the proteins, the C-terminal conserved region is annotated as a coiled-coil domain in Uniprot. The only conserved region of FezI is the hydrophobic region with an FWKGxxxG motif. FezL has a conserved PFxxGxxxG motif in the hydrophobic region and C-terminal helices that are not highly conserved between the proteins. The ferritin-like proteins (FLP) encoded in some *fez* gene clusters have a rubrerythrin domain and a conserved C-terminal GxxxG motif.

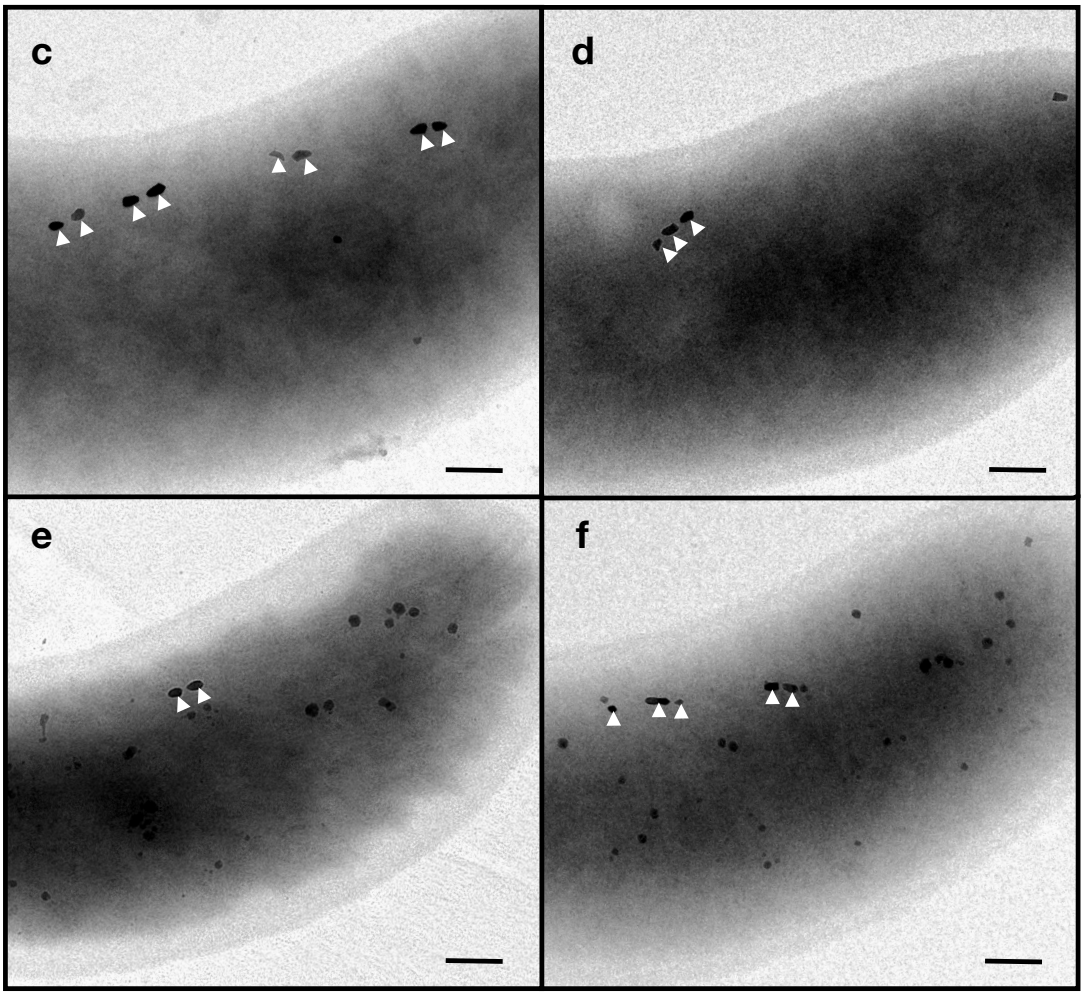

Supplementary Figure 6. WT and Δ*fezPC*$_{Dm}$ *D. magneticus* strains make ferrosomes in iron replete medium when expressing *fezAPC* in *trans*. Transmission electron micrographs of WT (a) and Δ*fezPC*$_{Dm}$ (b) strains with a control plasmid make magnetosomes (white carets) when grown in iron replete medium. When expressing *fezAPC* in *trans*, both the WT (c) and Δ*fezPC*$_{Dm}$ (d) strains make magnetosomes as well as ferrosomes when grown in iron replete medium. Scale bars, 200 nm.

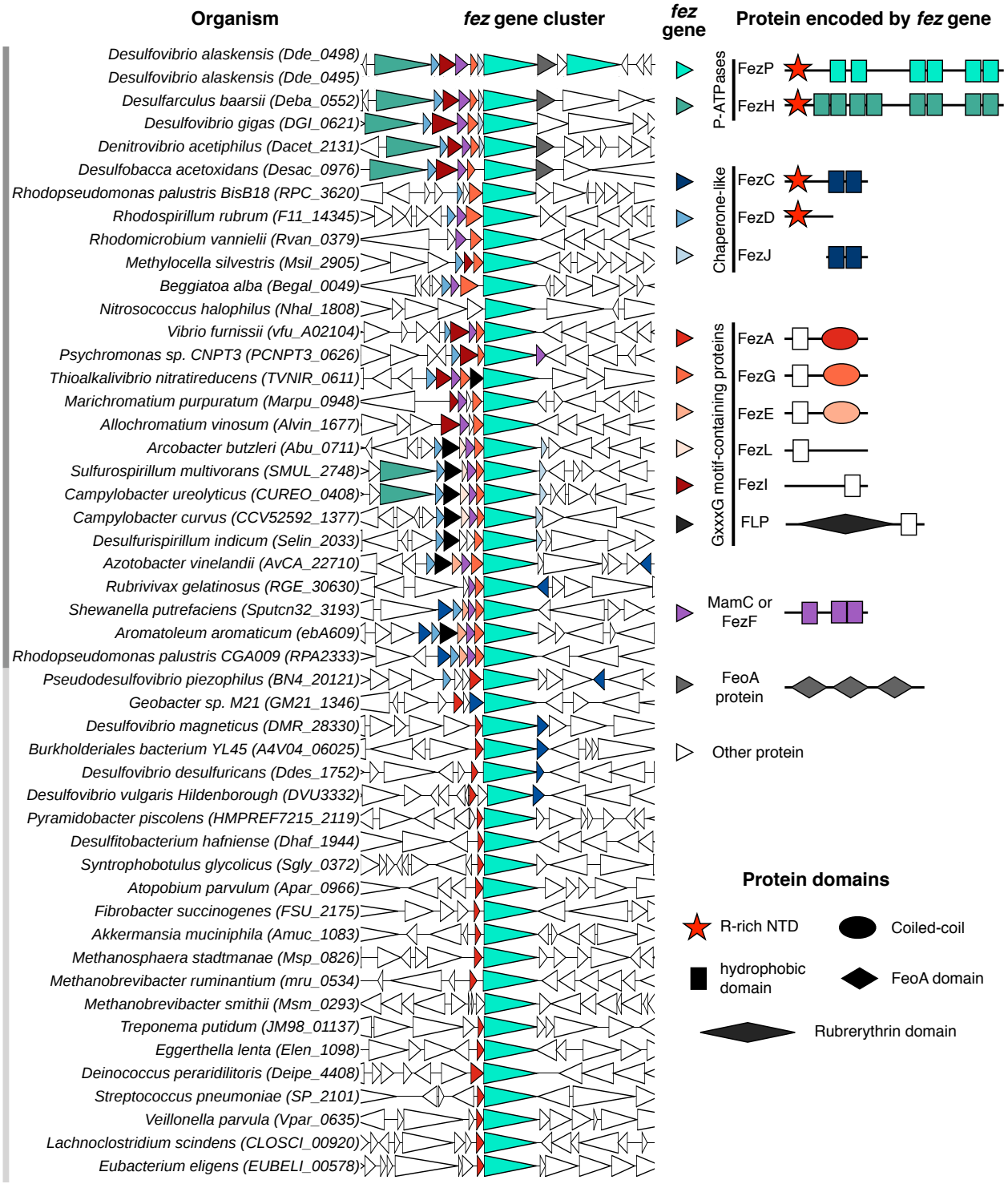

Supplementary Figure 7. Genomic regions of FezP. The genes encoding FezP are found in genomic regions with additional conserved genes which are colored. The key describes the conserved *fez* genes. Schematics of the proteins encoded by the *fez* genes show conserved domains (not to scale). Schematics of FezP and FezH are based on Supplementary Fig. 3 and Supplementary Fig. 9, respectively. Schematics of the

chaperone-like proteins are based on Supplementary Figure 4. Schematics of GxxxG motif-containing proteins are based on Supplementary Figure 5. MamC and FezF schematic based on Fig. 8. Domains found in multiple proteins are colored the same (transmembrane domain with GxxxG motif, white square; FezC and FezJ transmembrane domains, navy blue square; N-terminal domain with R-rich motif, red star). Domains specific to a protein are colored the same as the gene.

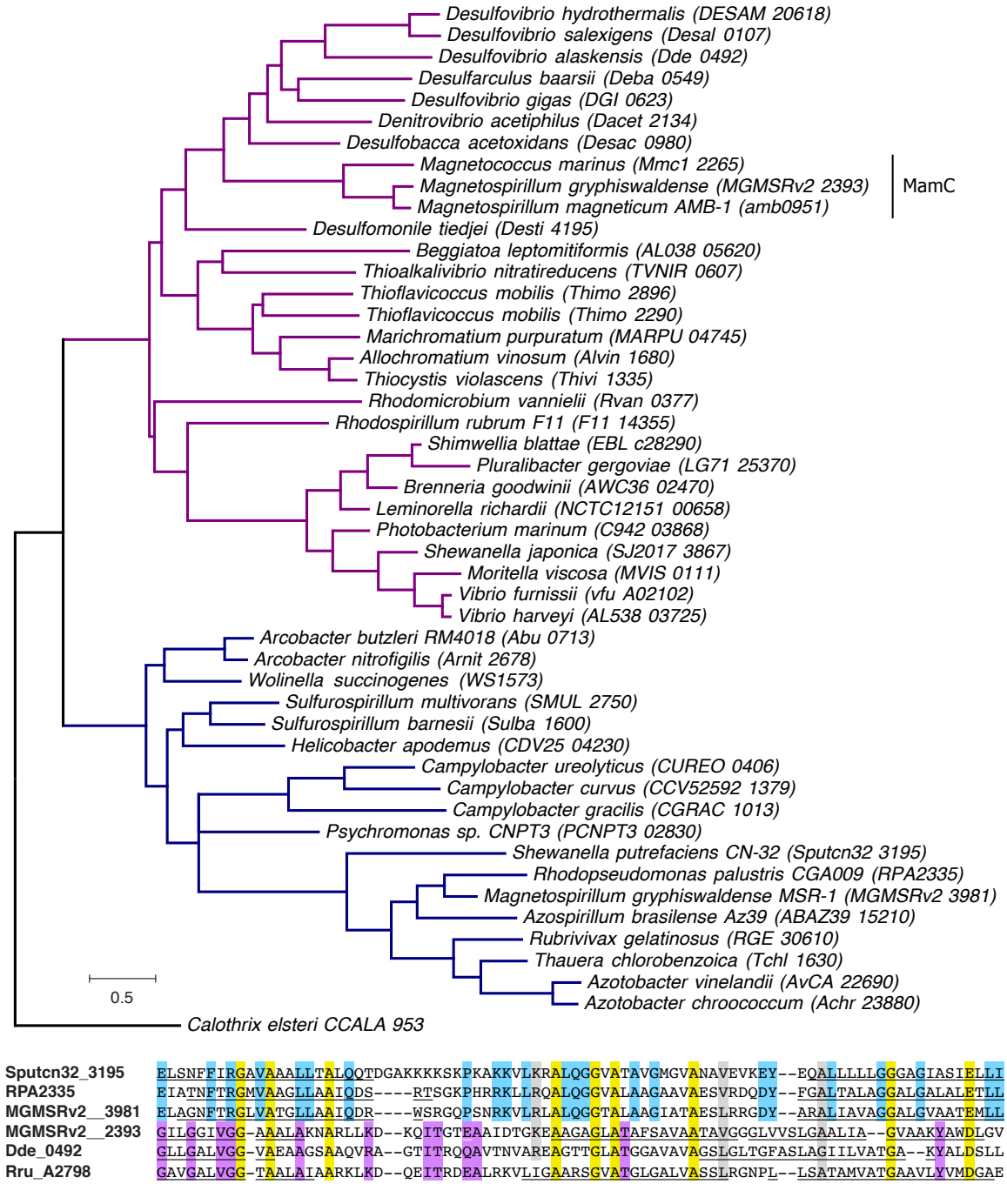

Supplementary Figure 8. Maximum likelihood tree and alignment of MamC and FezF. Two clear clades are shown in purple (MamC) and blue (FezF). Below, a multiple sequence alignment of MamC and FezF amino acid sequences. Transmembrane regions predicted with TOPCONS 1.0 are underlined. Residues conserved in all sequences are highlighted yellow. Residues conserved only in FezF are highlighted blue and those conserved only in MamC are highlighted purple. MamC groups with Dde_0492 whereas RPA2335 and Sputcn32_3195 are found in the FezF clade. A protein that was below the threshold in the JACKHMMER search was used to root the tree.

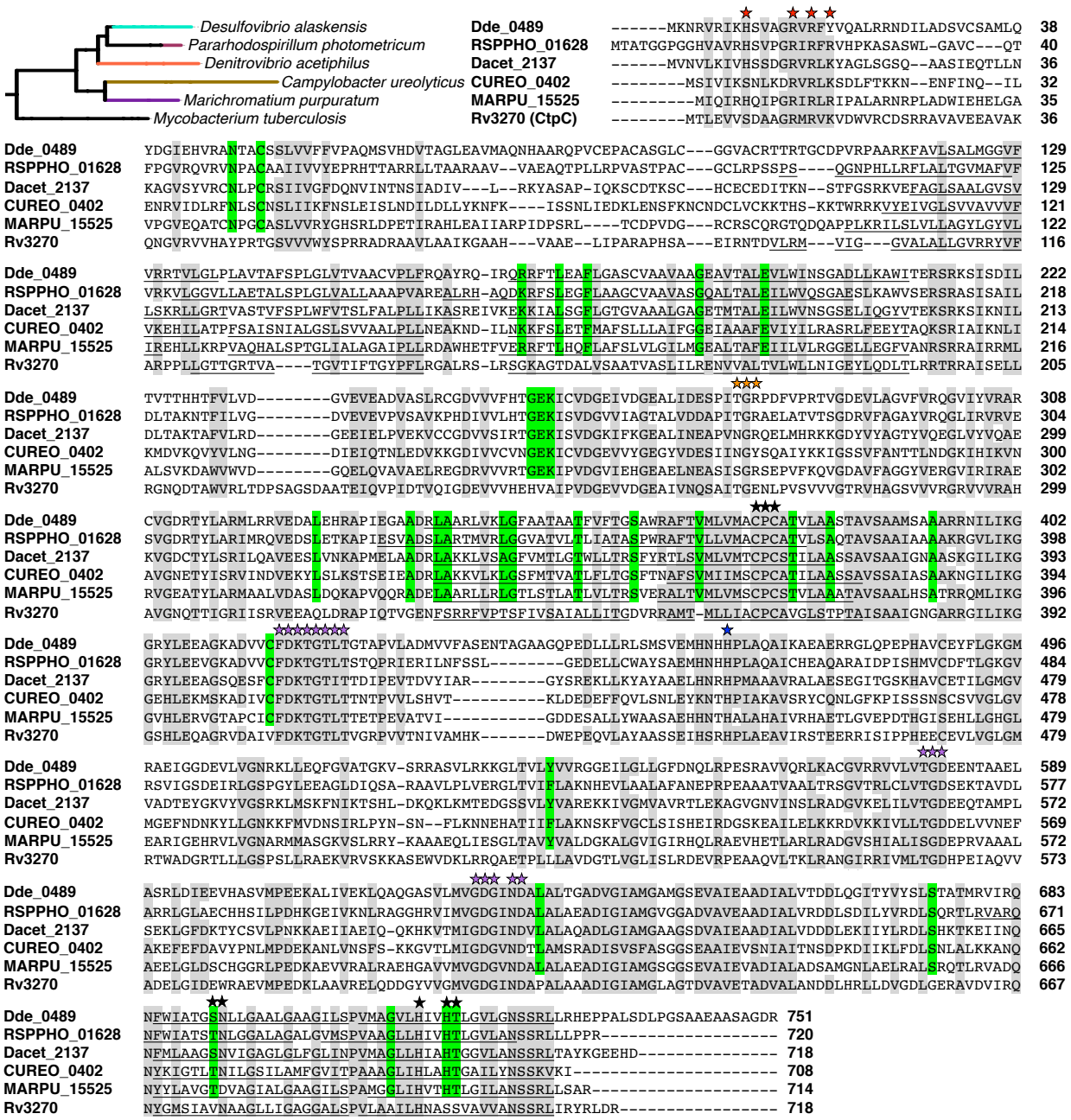

Supplementary Figure 9. Multiple sequence alignment of FezH and CtpC. The alignment is annotated as for the FezP alignment shown in Supp. Figure 3. FezH has the conserved residues in the A-, P- and N-domains, except that it lacks the glutamate in the dephosphorylation site of the A-domain. Residues found only in FezH are highlighted green. Residues found in FezH and CtpC are highlighted gray. Transmembrane regions predicted with TOPCONS 1.0 are underlined.

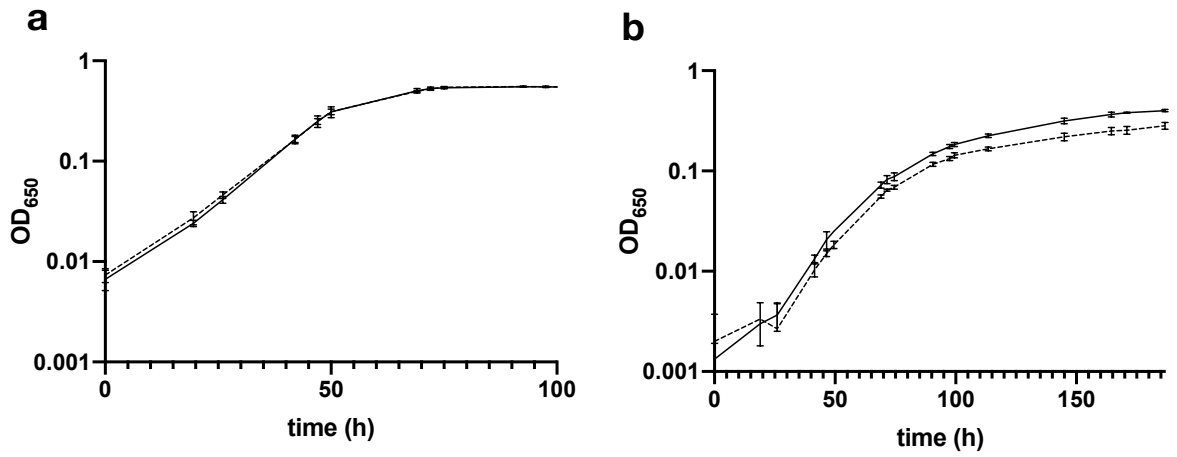

Supplementary Figure 10. Growth curves of D. magneticus WT and Δ*fezPC*$_{Dm}$ grown in iron replete medium (a) and iron-limited medium (b). WT, solid lines; Δ*fezPC*$_{Dm}$ dashed lines.

	P_{1B}-ATPase	Phobius[a]	TMHMM[b]	TMPred	TOPCONS[c]
FezP	DMR_28330	346-369 370-394 681-699 705-723	NA	33-51 196-216 350-365 370-394 531-551 685-700 708-728	137-157 187-207 341-361 364-384 678-698 701-721
	Sputcn32_3193	504-523	NA	103-120 144-167 220-240 322-337 504-519 657-678	103-123 162-182 314-334 339-359 651-671 673-693
	RPA2333	NA	NA	97-114 148-171 219-234 498-513 653-672	96-116 151-171 308-328 330-350 645-665 667-687
	Dde_0495	NA	NA	99-118 125-142 216-234 319-334 340-360 654-669 677-696	121-141 166-186 315-355 343-363 652-672 675-695
FezH	Dde_0489	114-131 137-159 344-363 369-394	134-156 176-198	47-65 113-130 137-159 175-194 347-363 365-381 632-648 693-712	117-137 139-159 168-188 190-210 340-360 362-382 685-705 707-727
CtpC	Rv3270	96-116 128-146 158-183	NA	96-117 121-142 155-180 335-353 359-381 617-632 677-696	96-116 122-142 151-171 173-193 331-351 355-375 669-689 691-711

Table 1. Transmembrane domain regions of FezP, FezH, and CtpC as predicted using prediction software [a](196); [b](197); [c](193).

Strain	Reference/Source
D. magneticus AK80	(50, 126)
D. magneticus ΔMAI	(52)
D. magneticus Δ$fezPC_{Dm}$	this work
R. palustris CGA009	(184)
R. palustris Δfez_{Rp}	this work
S. putrefaciens CN-32	Gift of Jeffrey Gralnick (UMN)
S. putrefaciens Δfez_{Sp}	this work
E. coli WM3064	lab strain
E. coli DH5α *λ-pir*	lab strain
D. alaskensis G20	(170)
D. alaskensis JK04090 (Δ*0489::tn5*)	(170)
D. alaskensis JK05437 (Δ*0495::tn5*)	(170)
D. alaskensis JK12571 (Δ*0498::tn5*)	(170)

Supplementary Table 2. Bacterial strains used in this study.

Plasmid	Description	Reference
pBMK7	Plasmid backbone for pAK1173	(157)
pAK0	Suicide vector backbone for pAK1175 and pAK1176	(19)
pAK22	Vector backbone for pAK1177 and pAK1181	(20)
pAK914	Replicative deletion plasmid backbone for targeted mutagenesis in *D. magneticus*	(163)
pAK1171	Deletion vector backbone for targeting *dmr_28330-40* in pAK914 digested with SacI/XbaI	This work
pAK1172	Deletion vector targeting *dmr_28330-40* with P_{npt}-*strAB* ligated into BamHI between upstream and downstream homology regions in pAK1171	This work
pAK1173	*dmr_28320-40* expressed under native promoter in pBMK7 backbone digested with SalI/XbaI	This work
pAK1175	Deletion vector targeting *S. putrefaciens* CN-32 *sputcn32_3193-8* in pAK31 digested with SpeI-HF	This work
pAK1176	Deletion vector targeting *R. palustris* CGA009 *rpa2333-8* in pAK31 digested with SpeI-HF	This work
pAK1177	*sputcn32_3193-8* expressed under native promoter in pAK22 digested with HindIII/SpeI	This work
pAK1181	*rpa2333-8* expressed under native promoter, digested with HindIII/SpeI	This work

Supplementary Table 3. Plasmids used in this study.

Name	Sequence from 5' end	Description
P1	CCGATATCCTATTGGCCTCTAGACCTGCAACTTCCTGGGCAG	F *dmr_28330-40* upstream for pAK1171
P2	CGGCCGGGGCGGATCCTTGAAACTCCACCCGGCAAG	R *dmr_28330-40* upstream for pAK1171 with BamHI for P_{npt}-*strAB* insertion
P3	GGAGTTTCAAGGATCCGCCCCGGCCGTCCTGCCC	F *dmr_28330-40* downstream for pAK1171 with BamHI for P_{npt}-*strAB* insertion
P4	CGACTCACTATAGGGAATTCGAGCTCGGAGGTAGGCCAGGTAGG	R *dmr_28330-40* downstream for pAK1171
P5	GGTCTCGGATCCGCCCAGGGGATAGGAGAAG	F P_{npt}-*strAB* for pAK1172
P6	GGTCTCGGATCCGTAGCTTCACGCTGCCGC	R P_{npt}-*strAB* for pAK1172
P7	GTTGTCGACGCTTCGGCCGTGCTCATCG	F P_{dmr_28320}-*dmr28320-40* for pAK1173
P8	GTTTCTAGATCAGGCCAGAAACCGCCGCC	R P_{dmr_28320}-*dmr28320-40* for pAK1173
P9	GAATTCCTGCAGCCCGGGGGATCCACTAACGGAATTGCTGCAAG	F *sput3198-3* upstream for pAK1175
P10	CGATGATATTAGGCGAACATTTATTTTAAGTGGGCC	R *sput3198-3* upstream for pAK1175
P11	CACTTAAAATAAATGTTCGCCTAATATCATCGTTAGAAAGC	F *sput3198-3* downstream for pAK1175
P12	CGGTGGCGGCCGCTCTAGAACATTAGGTTACCGATTGAC	R *sput3198-3* downstream for pAK1175
P13	CGAGGTCGACGGTATCGATAAGCTTCTTTATCCATAATTTCACC	F $P_{sput3198}$-*sput3198-3* for pAK1177
P14	GTGGCGGCCGCTCTAGAACTAGTTAAAAGCTAACACCTGTAG	R $P_{sput3198}$-*sput3198-3* for pAK1177
P15	GAATTCCTGCAGCCCGGGGGATCCATCGCGTGTAGTGCTGG	F *rpa2338-3* upstream for pAK1176
P16	CGAACGAGATGCCGACGCAGACCTTG	R *rpa2338-3* upstream for pAK1176
P17	CGTCGGCATCTCGTTCGCATCAAAGAAAC	F *rpa2338-3* downstream for pAK1176
P18	CGGTGGCGGCCGCTCTAGAATCGAAGCTGCAGCATTC	R *rpa2338-3* downstream for pAK1176
P19	CGAGGTCGACGGTATCGATAAGCTTTCTGGAAATCCTCGTTTCG	F $P_{rpa2338}$-*rpa2338-3* for pAK1181
P20	GTGGCGGCCGCTCTAGAACTAGTCTTCGTCGCCCAGTCTTC	R $P_{rpa2338}$-*rpa2338-3* for pAK1181
P21	TGAAAATAATAGCCCGCACC	F *dde_0495::tn5* (80:C2) check
P22	CCCGTAAGTTCGCTGTTCTC	F *dde_0489*::*tn5* (61:F6) check
P23	TTTCTGTACGGACTTTGCCC	F *dde_0498::tn5* (186:E2) check
P24	ACTGAGAAGCCCTTAGAGCC	R to check G20 Tn insertions (pRL27_IE_rev1)

Supplementary Table 4. List of primers used in this study.

Chapter 4

Conclusions and Future Directions

Carly R. Grant

The aim of this dissertation was to develop *Desulfovibrio magneticus* RS-1 as a model organism in order to elucidate the genetic basis for ferrosome formation and function. Surprisingly, we found that *fez* genes are necessary and sufficient for many bacteria to make ferrosomes. Now, with a fleet of genetically tractable bacteria, we can begin to understand the mechanism of ferrosome formation and function. This chapter discusses some of the exciting future research of magnetosomes and ferrosomes.

Bullet-shaped magnetosome formation

Our understanding of magnetosome formation is based mainly on two closely related bacteria—*Magnetospirillum magneticum* AMB-1 and *Magnetospirillum gryphiswaldense* MSR-1—that make cubooctahedral-shaped magnetite crystals within the magnetosome lumen (9, 159). The mechanism by which bacteria make elongated, bullet-shaped magnetite and greigite crystals is currently unknown. Now, with a system to directly manipulate the *D. magneticus* genome, described in Chapter 2, we may begin to understand and appreciate the different mechanisms of magnetosome formation (163). While a forward genetic screen successfully identified ten nonmagnetic mutants of *D. magneticus* (52), the function of the remaining 80% of the genes in the *D. magneticus* magnetosome gene island (MAI) remain unknown.

Genetic dissection of the *D. magneticus* MAI should begin with the genes conserved in the deeply branching MTB. Of particular interest are proteins that might help shape the magnetite crystal. Because the deeply-branching magnetotactic bacteria (MTB) lack the crystal shape-determining protein Mms6 of the *Magnetospirillum* spp., some *mad* genes may be the shape-determining factors for bullet-shaped crystals (198). Mad23 (DMR_40890), a protein encoded in the MAI regions of all deeply branching MTB (124), was previously suggested to have a role in forming the magnetite crystals of *D. magneticus* (199). While making a targeted mutation of *kupM*, we also attempted, unsuccessfully, to mutate *mad23* using *sacB* counterselection. By using *upp* counterselection rather than *sacB*, I recently made a targeted mutation of *mad23*. This mutant, Δ*mad23*, has a lower C_{mag} than WT. While we were expecting the crystals of the Δ*mad23* mutant to be deformed or smaller than WT, we instead found that the magnetosome chains were misaligned with normal magnetite crystal size and shape (Fig. 1). The crystal size and shape explains why this mutant wasn't isolated during the forward genetic screen and demonstrates the importance of having a method for targeted mutagenesis. Continued efforts to mutate the remaining *D. magneticus* MAI *mad* and *mam* genes is necessary to elucidate which genes are important for shaping the bullet-shaped magnetite crystal, positioning the magnetosomes in the cell, or in forming a magnetosome membrane, the presence of which is up for debate (50).

Mechanism of ferrosome formation and iron storage

The finding that ferrosome proteins have putative membrane domains supports the previous observations that ferrosomes are bound by lipid membranes (50, 106), and raises the question, how and when do ferrosome membranes form? Perhaps the answer lies in the unusual membrane topology of FezP and/or in the small Fez proteins with

hydrophobic GxxxG motif-containing domains. GxxxG motifs are common in membrane proteins and have been shown to facilitate protein-protein interactions within lipid membranes (166, 167). The protein-protein interactions facilitated by GxxxG motifs have even been shown to induce local curvature and tubulation of membranes (200). In support of an interaction hypothesis, the two *R. palustris* Fez proteins with FxxGxxxG motifs (FezG [RPA2334] and FezE [RPA2336]) were copurified and have been shown to interact in *R. palustris* (201). Future research aimed at determining if the GxxxG motif-containing Fez proteins or FezP affect membrane shape is needed.

Key in understanding the structure and function of ferrosomes is to determine the localization of the Fez proteins. Do Fez proteins localize to the cytoplasmic membrane or are they positioned on the ferrosome membrane? In addition to localization studies using microscopy, biochemical studies are needed to determine the function of Fez proteins. In a biochemical approach, ATPase activity of purified FezP and FezH can be measured *in vitro.* Using this assay, we can determine if FezP and FezH specifically transport iron or if other metals may be transported. Additionally, we can determine if FezC, FezD, and FezJ act as chaperones by improving metal specificity and increasing the rate of metal transport of FezP or FezH. Using genetics, biochemistry, and microscopy, the function of specific domains of FezP and FezH, as well as the putative chaperone-like proteins, will be key toward understanding how ferrosomes function. For example, does the R-rich motif, found in the N-terminal domain of FezP and FezH and putative chaperone-like Fez proteins, function in metal-binding or interact with lipid membranes? Are the conserved motifs in the transmembrane metal binding domains of FezP and FezH important for iron transport? The finding that proteins with domains related to iron homeostasis (e.g. the ferritin-like protein and FeoA-domain containing protein), are encoded by some *fez* gene clusters supports the hypothesis that ferrosomes are specific to iron storage. It will be interesting to determine if these proteins have a role in ferrosome formation or function. It will also be interesting if MamC and FezF bind iron within the ferrosome lumen. Finally, if ferrosomes function to store iron, then iron must be transported into and out of ferrosomes. Because P_{1B}-ATPases typically transport metals in one direction, from the cytoplasm out of the cell, it will be fascinating to learn how iron is transported into and out of ferrosomes.

Because iron storage appears to be a function of ferrosomes, we have focused on how Fez proteins may be involved in iron transport across the ferrosome membrane. However, it is likely that phosphate is also stored within ferrosomes (50, 106). The purpose of phosphate storage and the mechanism by which phosphate enters ferrosomes are important details of ferrosome research that remain unanswered.

Regulation of ferrosomes

In Chapter 3, I described the conditions under which ferrosomes are formed in diverse bacteria. In *D. magneticus*, we only observe ferrosomes when the cells are transitioning out of iron starvation. The pattern of ferrosome formation in *D. magneticus* suggests that fez_{Dm} gene expression is negatively regulated by the transcription factor Fur. As a

negative regulator, Fur, with Fe^{2+} as a cofactor, can bind to DNA and repress transcription (162). Thus, when iron is replete, many Fur-regulated genes are repressed and and when iron is limited, Fur-regulated genes are derepressed. Previous transcriptomic studies in many bacteria, including *D. vulgaris* Hildenborough which has a similar *fez* gene cluster to *D. magneticus* (172–174), have found that *fez* genes are negatively regulated by Fur. If Fur negatively regulates the *fez* genes, then in a Δ*fur* mutant, ferrosomes might be made constitutively. Recently, using *upp* counterselection, I was able to make a *D. magneticus fur* mutant by replacing the *fur* gene with a streptomycin-resistance cassette. This Δ*fur* mutant has improved growth in iron limited medium and a growth defect and lower C_{mag} in iron replete medium. Surprisingly, the Δ*fur* mutant grown in iron replete medium makes fewer magnetosomes and is instead filled with enlarged ferrosomes (Fig. 2). Although transcriptomic and proteomic analyses are needed, these results suggest that Fur regulates *fez* gene expression. It will be fascinating to determine if this phenotype repeats for other bacteria in which Fur has been shown to regulate *fez* gene expression.

Unlike *D. magneticus*, *Desulfovibrio alaskensis* G20, *Shewanella putrefaciens* CN-32, and *Rhodopseudomonas palustris* CGA009, make a smaller number of ferrosomes during anaerobic metabolism when iron is replete. This suggests that the regulation of ferrosomes may be different for these bacteria. *R. palustris* strains CGA009 and TIE-1 have nearly identical *fez* gene clusters that are positively regulated by the oxygen sensors AadR and FixK (180, 181). In addition to the *fez* genes, a gene encoding a Fur family transcriptional regulator (RPA2339, Rpal_2583) upstream of the *fez* gene cluster is also positively regulated by the oxygen sensors (180, 181). To determine if RPA2339 regulates the fez_{Rp} genes, I made a markerless deletion of *rpa2339*. Unlike *D. magneticus*, the Δ*rpa2339* looks similar to WT cells by TEM. Similarly, my undergraduate mentee, Sunaya Krishnapura, has found that a Δ*fur* mutant of *S. putrefaciens* does not appear to make ferrosomes constitutively. While further experiments are needed to untangle the network of ferrosome regulation, it is clear that the regulation of *fez* gene expression differs between these metabolically and phylogenetically diverse bacteria.

How widespread are ferrosomes?

While the bacteria found to form ferrosomes described in Chapter 3 are all isolates from the environment, many of the bacteria and the archaea with a $FezP_A$ homolog are host-associated, some of which can cause diseases in humans. Based on our finding that diverse microorganisms make ferrosomes via conserved *fez* genes, I hypothesize that host-associated microorganisms with *fez genes* also make ferrosomes. If so, ferrosomes may have an important role in maintaining iron homeostasis in these host-associated microorganisms. A previous study found that expression of the *Clostridium difficile fez* gene operon (*cd0591-2*) is regulated by Fur and is induced in iron limited conditions, including during hamster infection (172). These results suggest that *fez* genes in host-associated microorganisms are important for iron homeostasis and may be important for infection. Further research is needed to determine if *C. difficile*, and other host-associated microorganisms, make ferrosomes via the *fez* genes. Ferrosomes may prove to be an important target for drug development.

In Chapter 3, we identified FezP and FezH as two subgroups of P_{1B}-ATPases. Both FezP and FezH have membrane domains that are difficult to predict and may be important for ferrosome structure and/or function. The maximum likelihood tree of FezP described in Chapter 3, has additional clades of P_{1B}-ATPases that are closely related to FezP or FezH. One of these clades contains P_{1B}-ATPases from microorganisms of the phylum *Cyanobacteria*. The genes coding for these *Cyanobacteria* P_{1B}-ATPases are part of conserved gene clusters. Similar to the *fez* gene clusters, many of the *Cyanobacteria* clusters have additional conserved genes that code for proteins with hydrophobic GxxxG motif domains and chaperone-like proteins. Intriguingly, many of these *Cyanobacteria* make amorphous calcium carbonate granules that are bound by a membrane (182, 183), raising the possibility that ferrosomes are part of a larger class of storage organelle.

FIGURES

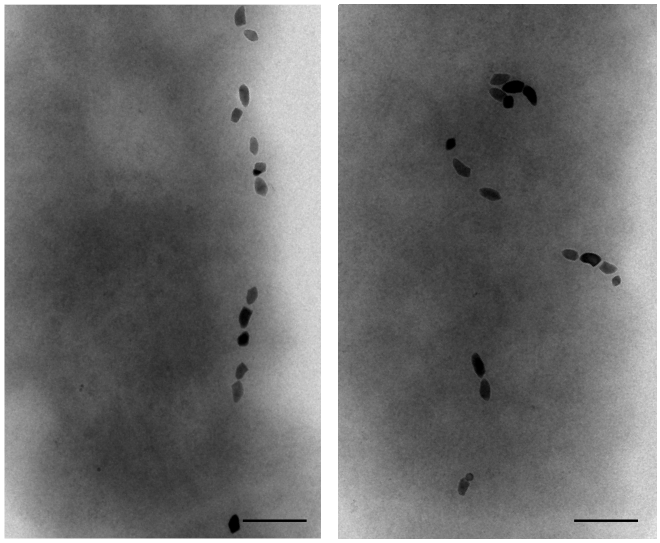

Figure 1. TEM of *D. magneticus* Δ*upp* Δ*mad23* mutant. The Δ*upp* Δ*mad23* mutant (right) has magnetosomes, similar in size and shape to the parent strain Δ*upp* (left), that are not aligned in a chain along the length of the cell. Scale bars, 200 nm.

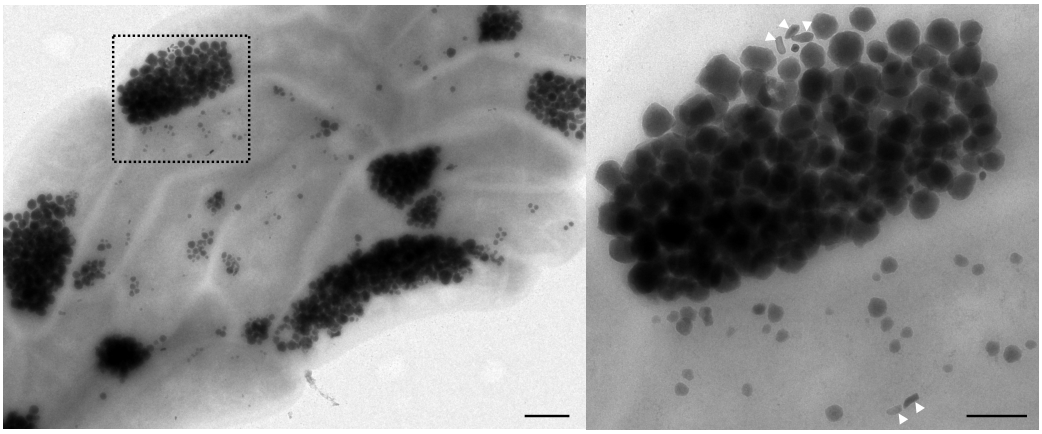

Figure 2. TEM of *D. magneticus* Δ*upp* Δ*fur* mutant. Many Δ*upp* Δ*fur* mutant mutant cells are filled with ferrosomes when grown in iron replete medium. Obvious magnetosomes are denoted with a white caret in the inset (right); however, additional magnetosomes may be masked by the ferrosomes. Scale bars, left 500 nm; right inset, 200 nm.

REFERENCES

1. Stanier RY, Van Niel CB. 1962. The concept of a bacterium. Arch Mikrobiol 42:17–35.

2. Dworkin M. 2012. Sergei Winogradsky: a founder of modern microbiology and the first microbial ecologist. FEMS Microbiol Rev 36:364–379.

3. Winogradsky, Sergei. 1887. Ueber Schwefelbacterien. Bot Zeit 45:489–610.

4. Bobik TA, Lehman BP, Yeates TO. 2015. Bacterial microcompartments: widespread prokaryotic organelles for isolation and optimization of metabolic pathways. Mol Microbiol 98:193–207.

5. Cornejo E, Abreu N, Komeili A. 2014. Compartmentalization and organelle formation in bacteria. Curr Opin Cell Biol 26:132–138.

6. Diekmann Y, Pereira-Leal JB. 2013. Evolution of intracellular compartmentalization. Biochem J 449:319–331.

7. Murat D, Byrne M, Komeili A. 2010. Cell Biology of Prokaryotic Organelles. Cold Spring Harb Perspect Biol 2:a000422.

8. Nichols RJ, Cassidy-Amstutz C, Chaijarasphong T, Savage DF. 2017. Encapsulins: molecular biology of the shell. Crit Rev Biochem Mol Biol 52:583–594.

9. Uebe R, Schüler D. 2016. Magnetosome biogenesis in magnetotactic bacteria. Nat Rev Microbiol 14:621–637.

10. Blakemore R. 1975. Magnetotactic bacteria. Science 190:377–379.

11. Frankel RB. 2009. The discovery of magnetotactic/magnetosensitive bacteria. Chin J Oceanol Limnol 27:1.

12. Simmons SL, Sievert SM, Frankel RB, Bazylinski DA, Edwards KJ. 2004. Spatiotemporal Distribution of Marine Magnetotactic Bacteria in a Seasonally Stratified Coastal Salt Pond. Appl Env Microbiol 70:6230–6239.

13. Bazylinski DA, Frankel RB. 2004. Magnetosome formation in prokaryotes. Nat Rev Microbiol 2:217–230.

14. Blakemore RP, Maratea D, Wolfe RS. 1979. Isolation and pure culture of a freshwater magnetic spirillum in chemically defined medium. J Bacteriol 140:720–729.

15. Matsunaga T, Sakaguchi T, Tadakoro F. 1991. Magnetite formation by a magnetic bacterium capable of growing aerobically. Appl Microbiol Biotechnol 35:651–655.

16. Schleifer KH, Schüler D, Spring S, Weizenegger M, Amann R, Ludwig W, Köhler M. 1991. The Genus *Magnetospirillum* gen. nov. Description of *Magnetospirillum gryphiswaldense* sp. nov. and Transfer of *Aquaspirillum magnetotacticum* to *Magnetospirillum magnetotacticum* comb. nov. Syst Appl Microbiol 14:379–385.

17. Balkwill DL, Maratea D, Blakemore RP. 1980. Ultrastructure of a magnetotactic spirillum. J Bacteriol 141:1399–1408.

18. Gorby YA, Beveridge TJ, Blakemore RP. 1988. Characterization of the bacterial magnetosome membrane. J Bacteriol 170:834–841.

19. Komeili A, Vali H, Beveridge TJ, Newman DK. 2004. Magnetosome vesicles are present before magnetite formation, and MamA is required for their activation. Proc Natl Acad Sci U S A 101:3839–3844.

20. Komeili A, Li Z, Newman DK, Jensen GJ. 2006. Magnetosomes Are Cell Membrane Invaginations Organized by the Actin-Like Protein MamK. Science 311:242–245.

21. Scheffel A, Gruska M, Faivre D, Linaroudis A, Plitzko JM, Schüler D. 2006. An acidic protein aligns magnetosomes along a filamentous structure in magnetotactic bacteria. Nature 440:110.

22. Grünberg K, Wawer C, Tebo BM, Schüler D. 2001. A Large Gene Cluster Encoding Several Magnetosome Proteins Is Conserved in Different Species of Magnetotactic Bacteria. Appl Env Microbiol 67:4573–4582.

23. Grünberg K, Müller E-C, Otto A, Reszka R, Linder D, Kube M, Reinhardt R, Schüler D. 2004. Biochemical and Proteomic Analysis of the Magnetosome Membrane in *Magnetospirillum gryphiswaldense*. Appl Env Microbiol 70:1040–1050.

24. Okuda Y, Denda K, Fukumori Y. 1996. Cloning and sequencing of a gene encoding a new member of the tetratricopeptide protein family from magnetosomes of *Magnetospirillum magnetotacticum*. Gene 171:99–102.

25. Lohße A, Ullrich S, Katzmann E, Borg S, Wanner G, Richter M, Voigt B, Schweder T, Schüler D. 2011. Functional Analysis of the Magnetosome Island in *Magnetospirillum gryphiswaldense*: The *mamAB* Operon Is Sufficient for Magnetite Biomineralization. PLOS ONE 6:e25561.

26. Murat D, Quinlan A, Vali H, Komeili A. 2010. Comprehensive genetic dissection of the magnetosome gene island reveals the step-wise assembly of a prokaryotic organelle. Proc Natl Acad Sci U S A 107:5593–5598.

27. Murat D, Falahati V, Bertinetti L, Csencsits R, Körnig A, Downing K, Faivre D, Komeili A. 2012. The magnetosome membrane protein, MmsF, is a major

regulator of magnetite biomineralization in *Magnetospirillum magneticum* AMB-1. Mol Microbiol 85:684–699.

28. Müller FD, Raschdorf O, Nudelman H, Messerer M, Katzmann E, Plitzko JM, Zarivach R, Schüler D. 2014. The FtsZ-Like Protein FtsZm of *Magnetospirillum gryphiswaldense* Likely Interacts with Its Generic Homolog and Is Required for Biomineralization under Nitrate Deprivation. J Bacteriol 196:650–659.

29. Raschdorf O, Müller FD, Pósfai M, Plitzko JM, Schüler D. 2013. The magnetosome proteins MamX, MamZ and MamH are involved in redox control of magnetite biomineralization in *Magnetospirillum gryphiswaldense.* Mol Microbiol 89:872–886.

30. Tanaka M, Mazuyama E, Arakaki A, Matsunaga T. 2011. MMS6 Protein Regulates Crystal Morphology during Nano-sized Magnetite Biomineralization in Vivo. J Biol Chem 286:6386–6392.

31. Kolinko I, Lohße A, Borg S, Raschdorf O, Jogler C, Tu Q, Pósfai M, Tompa É, Plitzko JM, Brachmann A, Wanner G, Müller R, Zhang Y, Schüler D. 2014. Biosynthesis of magnetic nanostructures in a foreign organism by transfer of bacterial magnetosome gene clusters. Nat Nanotechnol 9:193–197.

32. Alphandéry E. 2014. Applications of Magnetosomes Synthesized by Magnetotactic Bacteria in Medicine. Front Bioeng Biotechnol 2.

33. Barber-Zucker S, Zarivach R. 2017. A Look into the Biochemistry of Magnetosome Biosynthesis in Magnetotactic Bacteria. ACS Chem Biol 12:13–22.

34. Blakemore RP. 1982. Magnetotactic Bacteria. Annu Rev Microbiol 36:217–238.

35. Faivre D, Godec TU. 2015. From Bacteria to Mollusks: The Principles Underlying the Biomineralization of Iron Oxide Materials. Angew Chem Int Ed 54:4728–4747.

36. Lin W, Yongxin P, Bazylinski DA. 2017. Diversity and ecology of and biomineralization by magnetotactic bacteria. Environ Microbiol Rep 9:345–356.

37. Lefèvre CT, Bazylinski DA. 2013. Ecology, Diversity, and Evolution of Magnetotactic Bacteria. Microbiol Mol Biol Rev 77:497–526.

38. Raschdorf O, Forstner Y, Kolinko I, Uebe R, Plitzko JM, Schüler D. 2016. Genetic and Ultrastructural Analysis Reveals the Key Players and Initial Steps of Bacterial Magnetosome Membrane Biogenesis. PLOS Genet 12:e1006101.

39. Uebe R, Keren-Khadmy N, Zeytuni N, Katzmann E, Navon Y, Davidov G, Bitton R, Plitzko JM, Schüler D, Zarivach R. 2018. The dual role of MamB in magnetosome

membrane assembly and magnetite biomineralization. Mol Microbiol 107:542–557.

40. Hershey DM, Browne PJ, Iavarone AT, Teyra J, Lee EH, Sidhu SS, Komeili A. 2016. Magnetite Biomineralization in *Magnetospirillum magneticum* Is Regulated by a Switch-like Behavior in the HtrA Protease MamE. J Biol Chem 291:17941–17952.

41. Hershey DM, Ren X, Melnyk RA, Browne PJ, Ozyamak E, Jones SR, Chang MCY, Hurley JH, Komeili A. 2016. MamO Is a Repurposed Serine Protease that Promotes Magnetite Biomineralization through Direct Transition Metal Binding in Magnetotactic Bacteria. PLOS Biol 14:e1002402.

42. Quinlan A, Murat D, Vali H, Komeili A. 2011. The HtrA/DegP family protease MamE is a bifunctional protein with roles in magnetosome protein localization and magnetite biomineralization. Mol Microbiol 80:1075–1087.

43. Uebe R, Junge K, Henn V, Poxleitner G, Katzmann E, Plitzko JM, Zarivach R, Kasama T, Wanner G, Pósfai M, Böttger L, Matzanke B, Schüler D. 2011. The cation diffusion facilitator proteins MamB and MamM of M*agnetospirillum gryphiswaldense* have distinct and complex functions, and are involved in magnetite biomineralization and magnetosome membrane assembly. Mol Microbiol 82:818–835.

44. Stachowiak JC, Schmid EM, Ryan CJ, Ann HS, Sasaki DY, Sherman MB, Geissler PL, Fletcher DA, Hayden CC. 2012. Membrane bending by protein–protein crowding. Nat Cell Biol 14:944–949.

45. Cornejo E, Subramanian P, Li Z, Jensen GJ, Komeili A. 2016. Dynamic Remodeling of the Magnetosome Membrane Is Triggered by the Initiation of Biomineralization. mBio 7:e01898-15.

46. Arakaki A, Kikuchi D, Tanaka M, Yamagishi A, Yoda T, Matsunaga T. 2016. Comparative Subcellular Localization Analysis of Magnetosome Proteins Reveals a Unique Localization Behavior of Mms6 Protein onto Magnetite Crystals. J Bacteriol 198:2794–2802.

47. Tanaka M, Arakaki A, Matsunaga T. 2010. Identification and functional characterization of liposome tubulation protein from magnetotactic bacteria. Mol Microbiol 76:480–488.

48. Yamamoto D, Taoka A, Uchihashi T, Sasaki H, Watanabe H, Ando T, Fukumori Y. 2010. Visualization and structural analysis of the bacterial magnetic organelle magnetosome using atomic force microscopy. Proc Natl Acad Sci 107:9382–9387.

49. Zeytuni N, Ozyamak E, Ben-Harush K, Davidov G, Levin M, Gat Y, Moyal T, Brik A, Komeili A, Zarivach R. 2011. Self-recognition mechanism of MamA, a magnetosome-associated TPR-containing protein, promotes complex assembly. Proc Natl Acad Sci 108:E480–E487.

50. Byrne ME, Ball DA, Guerquin-Kern J-L, Rouiller I, Wu T-D, Downing KH, Vali H, Komeili A. 2010. *Desulfovibrio magneticus* RS-1 contains an iron- and phosphorus-rich organelle distinct from its bullet-shaped magnetosomes. Proc Natl Acad Sci U S A 107:12263–12268.

51. Lefèvre CT, Trubitsyn D, Abreu F, Kolinko S, Jogler C, de Almeida LGP, de Vasconcelos ATR, Kube M, Reinhardt R, Lins U, Pignol D, Schüler D, Bazylinski DA, Ginet N. 2013. Comparative genomic analysis of magnetotactic bacteria from the *Deltaproteobacteria* provides new insights into magnetite and greigite magnetosome genes required for magnetotaxis. Environ Microbiol 15:2712–2735.

52. Rahn-Lee L, Byrne ME, Zhang M, Sage DL, Glenn DR, Milbourne T, Walsworth RL, Vali H, Komeili A. 2015. A Genetic Strategy for Probing the Functional Diversity of Magnetosome Formation. PLOS Genet 11:e1004811.

53. Katzmann E, Scheffel A, Gruska M, Plitzko JM, Schüler D. 2010. Loss of the actin-like protein MamK has pleiotropic effects on magnetosome formation and chain assembly in *Magnetospirillum gryphiswaldense*. Mol Microbiol 77:208–224.

54. Ozyamak E, Kollman JM, Komeili A. 2013. Bacterial Actins and Their Diversity. Biochemistry 52:6928–6939.

55. Katzmann E, Müller FD, Lang C, Messerer M, Winklhofer M, Plitzko JM, Schüler D. 2011. Magnetosome chains are recruited to cellular division sites and split by asymmetric septation: Segregation of magnetosome chains during cytokinesis. Mol Microbiol 82:1316–1329.

56. Ozyamak E, Kollman J, Agard DA, Komeili A. 2013. The Bacterial Actin MamK: in vitro assembly behavior and filament architecture. J Biol Chem 288:4265–4277.

57. Löwe J, He S, Scheres SHW, Savva CG. 2016. X-ray and cryo-EM structures of monomeric and filamentous actin-like protein MamK reveal changes associated with polymerization. Proc Natl Acad Sci 113:13396–13401.

58. Bergeron JRC, Hutto R, Ozyamak E, Hom N, Hansen J, Draper O, Byrne ME, Keyhani S, Komeili A, Kollman JM. 2017. Structure of the magnetosome-associated actin-like MamK filament at subnanometer resolution. Protein Sci 26:93–102.

59. Toro-Nahuelpan M, Müller FD, Klumpp S, Plitzko JM, Bramkamp M, Schüler D. 2016. Segregation of prokaryotic magnetosomes organelles is driven by treadmilling of a dynamic actin-like MamK filament. BMC Biol 14:88.

60. Taoka A, Kiyokawa A, Uesugi C, Kikuchi Y, Oestreicher Z, Morii K, Eguchi Y, Fukumori Y. 2017. Tethered Magnets Are the Key to Magnetotaxis: Direct Observations of *Magnetospirillum magneticum* AMB-1 Show that MamK Distributes Magnetosome Organelles Equally to Daughter Cells. mBio 8:e00679-17.

61. Draper O, Byrne ME, Li Z, Keyhani S, Barrozo JC, Jensen G, Komeili A. 2011. MamK, a bacterial actin, forms dynamic filaments in vivo that are regulated by the acidic proteins MamJ and LimJ. Mol Microbiol 82:342–354.

62. Scheffel A, Schüler D. 2007. The Acidic Repetitive Domain of the *Magnetospirillum gryphiswaldense* MamJ Protein Displays Hypervariability but Is Not Required for Magnetosome Chain Assembly. J Bacteriol 189:6437–6446.

63. Rioux J-B, Philippe N, Pereira S, Pignol D, Wu L-F, Ginet N. 2010. A Second Actin-Like MamK Protein in *Magnetospirillum magneticum* AMB-1 Encoded Outside the Genomic Magnetosome Island. PLOS ONE 5:e9151.

64. Abreu N, Mannoubi S, Ozyamak E, Pignol D, Ginet N, Komeili A. 2014. Interplay between Two Bacterial Actin Homologs, MamK and MamK-Like, Is Required for the Alignment of Magnetosome Organelles in *Magnetospirillum magneticum* AMB-1. J Bacteriol 196:3111–3121.

65. Lindsay M, Webb R, Strous M, Jetten M, Butler M, Forde R, Fuerst J. 2001. Cell compartmentalisation in planctomycetes: novel types of structural organisation for the bacterial cell. Arch Microbiol 175:413–429.

66. Santarella-Mellwig R, Franke J, Jaedicke A, Gorjanacz M, Bauer U, Budd A, Mattaj IW, Devos DP. 2010. The Compartmentalized Bacteria of the Planctomycetes-Verrucomicrobia-Chlamydiae Superphylum Have Membrane Coat-Like Proteins. PLOS Biol 8:e1000281.

67. Lonhienne TGA, Sagulenko E, Webb RI, Lee K-C, Franke J, Devos DP, Nouwens A, Carroll BJ, Fuerst JA. 2010. Endocytosis-like protein uptake in the bacterium *Gemmata obscuriglobus*. Proc Natl Acad Sci 107:12883–12888.

68. Fuerst JA, Webb RI. 1991. Membrane-bounded nucleoid in the eubacterium *Gemmatata obscuriglobus*. Proc Natl Acad Sci U S A 88:8184–8188.

69. Sagulenko E, Nouwens A, Webb RI, Green K, Yee B, Morgan G, Leis A, Lee K-C, Butler MK, Chia N, Pham UTP, Lindgreen S, Catchpole R, Poole AM, Fuerst JA.

2017. Nuclear Pore-Like Structures in a Compartmentalized Bacterium. PLOS ONE 12:e0169432.

70. Boedeker C, Schüler M, Reintjes G, Jeske O, van Teeseling MCF, Jogler M, Rast P, Borchert D, Devos DP, Kucklick M, Schaffer M, Kolter R, van Niftrik L, Engelmann S, Amann R, Rohde M, Engelhardt H, Jogler C. 2017. Determining the bacterial cell biology of Planctomycetes. Nat Commun 8.

71. Lieber A, Leis A, Kushmaro A, Minsky A, Medalia O. 2009. Chromatin Organization and Radio Resistance in the Bacterium *Gemmata obscuriglobus*. J Bacteriol 191:1439–1445.

72. Jeske O, Schüler M, Schumann P, Schneider A, Boedeker C, Jogler M, Bollschweiler D, Rohde M, Mayer C, Engelhardt H, Spring S, Jogler C. 2015. Planctomycetes do possess a peptidoglycan cell wall. Nat Commun 6:ncomms8116.

73. Mahat R, Seebart C, Basile F, Ward NL. 2016. Global and Targeted Lipid Analysis of *Gemmata obscuriglobus* Reveals the Presence of Lipopolysaccharide, a Signature of the Classical Gram-Negative Outer Membrane. J Bacteriol 198:221–236.

74. Speth DR, van Teeseling MCF, Jetten MSM. 2012. Genomic Analysis Indicates the Presence of an Asymmetric Bilayer Outer Membrane in Planctomycetes and Verrucomicrobia. Front Microbiol 3.

75. van Teeseling MCF, Mesman RJ, Kuru E, Espaillat A, Cava F, Brun YV, VanNieuwenhze MS, Kartal B, van Niftrik L. 2015. Anammox Planctomycetes have a peptidoglycan cell wall. Nat Commun 6.

76. Santarella-Mellwig R, Pruggnaller S, Roos N, Mattaj IW, Devos DP. 2013. Three-Dimensional Reconstruction of Bacteria with a Complex Endomembrane System. PLOS Biol 11:e1001565.

77. Erbilgin O, McDonald KL, Kerfeld CA. 2014. Characterization of a Planctomycetal Organelle: a Novel Bacterial Microcompartment for the Aerobic Degradation of Plant Saccharides. Appl Env Microbiol 80:2193–2205.

78. Jogler C, Glöckner FO, Kolter R. 2011. Characterization of *Planctomyces limnophilus* and Development of Genetic Tools for Its Manipulation Establish It as a Model Species for the Phylum Planctomycetes. Appl Environ Microbiol 77:5826–5829.

79. Rivas-Marín E, Canosa I, Santero E, Devos DP. 2016. Development of Genetic Tools for the Manipulation of the Planctomycetes. Front Microbiol 7.

80. Kartal B, van Niftrik L, Keltjens JT, Op den Camp HJM, Jetten MSM. 2012. Anammox—Growth Physiology, Cell Biology, and Metabolism, p. 211–262. *In* Poole, RK (ed.), Advances in Microbial Physiology. Academic Press.

81. van Niftrik L, Geerts WJC, van Donselaar EG, Humbel BM, Yakushevska A, Verkleij AJ, Jetten MSM, Strous M. 2008. Combined structural and chemical analysis of the anammoxosome: A membrane-bounded intracytoplasmic compartment in anammox bacteria. J Struct Biol 161:401–410.

82. Sinninghe Damsté JS, Strous M, Rijpstra WIC, Hopmans EC, Geenevasen JAJ, van Duin ACT, van Niftrik L, Jetten MSM. 2002. Linearly concatenated cyclobutane lipids form a dense bacterial membrane. Nature 419:708–712.

83. Neumann S, Wessels HJCT, Rijpstra WIC, Sinninghe Damsté JS, Kartal B, Jetten MSM, van Niftrik L. 2014. Isolation and characterization of a prokaryotic cell organelle from the anammox bacterium *Kuenenia stuttgartiensis*. Mol Microbiol 94:794–802.

84. Almeida NM de, Neumann S, Mesman RJ, Ferousi C, Keltjens JT, Jetten MSM, Kartal B, van Niftrik L. 2015. Immunogold Localization of Key Metabolic Enzymes in the Anammoxosome and on the Tubule-Like Structures of *Kuenenia stuttgartiensis*. J Bacteriol 197:2432–2441.

85. Kartal B, Maalcke WJ, de Almeida NM, Cirpus I, Gloerich J, Geerts W, Op den Camp HJM, Harhangi HR, Janssen-Megens EM, Francoijs K-J, Stunnenberg HG, Keltjens JT, Jetten MSM, Strous M. 2011. Molecular mechanism of anaerobic ammonium oxidation. Nature 479:127–130.

86. Strous M, Pelletier E, Mangenot S, Rattei T, Lehner A, Taylor MW, Horn M, Daims H, Bartol-Mavel D, Wincker P, Barbe V, Fonknechten N, Vallenet D, Segurens B, Schenowitz-Truong C, Médigue C, Collingro A, Snel B, Dutilh BE, Op den Camp HJM, van der Drift C, Cirpus I, van de Pas-Schoonen KT, Harhangi HR, van Niftrik L, Schmid M, Keltjens J, van de Vossenberg J, Kartal B, Meier H, Frishman D, Huynen MA, Mewes H-W, Weissenbach J, Jetten MSM, Wagner M, Le Paslier D. 2006. Deciphering the evolution and metabolism of an anammox bacterium from a community genome. Nature 440:790–794.

87. Kartal B, Almeida D, M N, Maalcke WJ, Camp O den, J.m H, Jetten MSM, Keltjens JT. 2013. How to make a living from anaerobic ammonium oxidation. FEMS Microbiol Rev 37:428–461.

88. van Niftrik L, Geerts WJC, Donselaar EG van, Humbel BM, Webb RI, Fuerst JA, Verkleij AJ, Jetten MSM, Strous M. 2008. Linking Ultrastructure and Function in Four Genera of Anaerobic Ammonium-Oxidizing Bacteria: Cell Plan, Glycogen Storage, and Localization of Cytochrome c Proteins. J Bacteriol 190:708–717.

89. Karlsson R, Karlsson A, Bäckman O, Johansson BR, Hulth S. 2014. Subcellular localization of an ATPase in anammox bacteria using proteomics and immunogold electron microscopy. FEMS Microbiol Lett 354:10–18.

90. van Niftrik L, Van Helden M, Kirchen S, Van Donselaar EG, Harhangi HR, Webb RI, Fuerst JA, Op den Camp HJM, Jetten MSM, Strous M. 2010. Intracellular localization of membrane-bound ATPases in the compartmentalized anammox bacterium '*Candidatus* Kuenenia stuttgartiensis.' Mol Microbiol 77:701–715.

91. Schouten S, Strous M, Kuypers MMM, Rijpstra WIC, Baas M, Schubert CJ, Jetten MSM, Damsté JSS. 2004. Stable Carbon Isotopic Fractionations Associated with Inorganic Carbon Fixation by Anaerobic Ammonium-Oxidizing Bacteria. Appl Environ Microbiol 70:3785–3788.

92. van de Graaf AA, de Bruijn P, Robertson LA, Jetten MSM, Kuenen JG. 1997. Metabolic pathway of anaerobic ammonium oxidation on the basis of 15N studies in a fluidized bed reactor. Microbiology 143:2415–2421.

93. McHugh CA, Fontana J, Nemecek D, Cheng N, Aksyuk AA, Heymann JB, Winkler DC, Lam AS, Wall JS, Steven AC, Hoiczyk E. 2014. A virus capsid-like nanocompartment that stores iron and protects bacteria from oxidative stress. EMBO J 33:1896–1911.

94. He D, Hughes S, Vanden-Hehir S, Georgiev A, Altenbach K, Tarrant E, Mackay CL, Waldron KJ, Clarke DJ, Marles-Wright J. 2016. Structural characterization of encapsulated ferritin provides insight into iron storage in bacterial nanocompartments. eLife 5:e18972.

95. Sutter M, Boehringer D, Gutmann S, Günther S, Prangishvili D, Loessner MJ, Stetter KO, Weber-Ban E, Ban N. 2008. Structural basis of enzyme encapsulation into a bacterial nanocompartment. Nat Struct Mol Biol 15:939–947.

96. Ferousi C, Lindhoud S, Baymann F, Kartal B, Jetten MS, Reimann J. 2017. Iron assimilation and utilization in anaerobic ammonium oxidizing bacteria. Curr Opin Chem Biol 37:129–136.

97. Giessen TW, Silver PA. 2017. Widespread distribution of encapsulin nanocompartments reveals functional diversity. Nat Microbiol 2:nmicrobiol201729.

98. van Niftrik L, Geerts WJC, Van Donselaar EG, Humbel BM, Webb RI, Harhangi HR, Camp HJMO den, Fuerst JA, Verkleij AJ, Jetten MSM, Strous M. 2009. Cell division ring, a new cell division protein and vertical inheritance of a bacterial organelle in anammox planctomycetes. Mol Microbiol 73:1009–1019.

99. Güven D, Dapena A, Kartal B, Schmid MC, Maas B, Pas-Schoonen K van de, Sozen S, Mendez R, Camp HJMO den, Jetten MSM, Strous M, Schmidt I. 2005.

Propionate Oxidation by and Methanol Inhibition of Anaerobic Ammonium-Oxidizing Bacteria. Appl Environ Microbiol 71:1066–1071.

100. Docampo R, Scott DA, Vercesi AE, Moreno SNJ. 1995. Intracellular Ca2+ storage in acidocalcisomes of *Trypanosoma cruzi.* Biochem J 310:1005–1012.

101. Vercesi AE, Moreno SN, Docampo R. 1994. Ca2+/H+ exchange in acidic vacuoles of *Trypanosoma brucei*. Biochem J 304:227–233.

102. Docampo R, Souza W de, Miranda K, Rohloff P, Moreno SNJ. 2005. Acidocalcisomes ? conserved from bacteria to man. Nat Rev Microbiol 3:nrmicro1097.

103. Seufferheld M, Vieira MCF, Ruiz FA, Rodrigues CO, Moreno SNJ, Docampo R. 2003. Identification of Organelles in Bacteria Similar to Acidocalcisomes of Unicellular Eukaryotes. J Biol Chem 278:29971–29978.

104. Seufferheld M, Lea CR, Vieira M, Oldfield E, Docampo R. 2004. The H+-pyrophosphatase of *Rhodospirillum rubrum* Is Predominantly Located in Polyphosphate-rich Acidocalcisomes. J Biol Chem 279:51193–51202.

105. López-Marqués RL, Pérez-Castiñeira JR, Losada M, Serrano A. 2004. Differential Regulation of Soluble and Membrane-Bound Inorganic Pyrophosphatases in the Photosynthetic Bacterium *Rhodospirillum rubrum* Provides Insights into Pyrophosphate-Based Stress Bioenergetics. J Bacteriol 186:5418–5426.

106. Glasauer S, Langley S, Beveridge TJ. 2002. Intracellular Iron Minerals in a Dissimilatory Iron-Reducing Bacterium. Science 295:117–119.

107. Glasauer S, Langley S, Boyanov M, Lai B, Kemner K, Beveridge TJ. 2007. Mixed-Valence Cytoplasmic Iron Granules Are Linked to Anaerobic Respiration. Appl Environ Microbiol 73:993–996.

108. Huber H, Burggraf S, Mayer T, Wyschkony I, Rachel R, Stetter KO. 2000. *Ignicoccus* gen. nov., a novel genus of hyperthermophilic, chemolithoautotrophic *Archaea*, represented by two new species, *Ignicoccus islandicus* sp nov and *Ignicoccus pacificus* sp nov. and *Ignicoccus pacificus* sp. nov. Int J Syst Evol Microbiol 50:2093–2100.

109. Rachel R, Wyschkony I, Riehl S, Huber H. 2002. The ultrastructure of *Ignicoccus*: Evidence for a novel outer membrane and for intracellular vesicle budding in an archaeon. Archaea 1:9–18.

110. Huber H, Hohn MJ, Rachel R, Fuchs T, Wimmer VC, Stetter KO. 2002. A new phylum of Archaea represented by a nanosized hyperthermophilic symbiont. Nature 417:63–67.

111. Paper W, Jahn U, Hohn MJ, Kronner M, Näther DJ, Burghardt T, Rachel R, Stetter KO, Huber H. 2007. *Ignicoccus hospitalis* sp. nov., the host of '*Nanoarchaeum equitans*.' Int J Syst Evol Microbiol 57:803–808.

112. Küper U, Meyer C, Müller V, Rachel R, Huber H. 2010. Energized outer membrane and spatial separation of metabolic processes in the hyperthermophilic Archaeon *Ignicoccus hospitalis*. Proc Natl Acad Sci 107:3152–3156.

113. Mayer F, Küper U, Meyer C, Daxer S, Müller V, Rachel R, Huber H. 2012. AMP-Forming Acetyl Coenzyme A Synthetase in the Outermost Membrane of the Hyperthermophilic Crenarchaeon *Ignicoccus hospitalis.* J Bacteriol 194:1572–1581.

114. Heimerl T, Flechsler J, Pickl C, Heinz V, Salecker B, Zweck J, Wanner G, Geimer S, Samson RY, Bell SD, Huber H, Wirth R, Wurch L, Podar M, Rachel R. 2017. A Complex Endomembrane System in the Archaeon *Ignicoccus hospitalis* Tapped by *Nanoarchaeum equitans*. Front Microbiol 8.

115. Zaremba-Niedzwiedzka K, Caceres EF, Saw JH, Bäckström D, Juzokaite L, Vancaester E, Seitz KW, Anantharaman K, Starnawski P, Kjeldsen KU, Stott MB, Nunoura T, Banfield JF, Schramm A, Baker BJ, Spang A, Ettema TJG. 2017. Asgard archaea illuminate the origin of eukaryotic cellular complexity. Nature 541:353–358.

116. Dobro MJ, Oikonomou CM, Piper A, Cohen J, Guo K, Jensen T, Tadayon J, Donermeyer J, Park Y, Solis BA, Kjær A, Jewett AI, McDowall AW, Chen S, Chang Y-W, Shi J, Subramanian P, Iancu CV, Li Z, Briegel A, Tocheva EI, Pilhofer M, Jensen GJ. 2017. Uncharacterized Bacterial Structures Revealed by Electron Cryotomography. J Bacteriol 199:e00100-17.

117. Fenchel T, Thar R. 2004. "*Candidatus* Ovobacter propellens": a large conspicuous prokaryote with an unusual motility behaviour. FEMS Microbiol Ecol 48:231–238.

118. Felfoul O, Mohammadi M, Taherkhani S, de Lanauze D, Zhong Xu Y, Loghin D, Essa S, Jancik S, Houle D, Lafleur M, Gaboury L, Tabrizian M, Kaou N, Atkin M, Vuong T, Batist G, Beauchemin N, Radzioch D, Martel S. 2016. Magneto-aerotactic bacteria deliver drug-containing nanoliposomes to tumour hypoxic regions. Nat Nanotechnol 11:941–947.

119. Bellini S. 2009. On a unique behavior of freshwater bacteria. Chin J Oceanol Limnol 27:3.

120. Bazylinski DA, Frankel RB, Jannasch HW. 1988. Anaerobic magnetite production by a marine, magnetotactic bacterium. Nature 334:518–519.

121. Schüler D, Köhler M. 1992. The isolation of a new magnetic spirillum. Zentralblatt Für Mikrobiol 147:150–151.

122. Komeili A. 2012. Molecular mechanisms of compartmentalization and biomineralization in magnetotactic bacteria. FEMS Microbiol Rev 36:232–255.

123. Pósfai M, Lefèvre C, Trubitsyn D, Bazylinski DA, Frankel R. 2013. Phylogenetic significance of composition and crystal morphology of magnetosome minerals. Front Microbiol 4.

124. Lin W, Zhang W, Zhao X, Roberts AP, Paterson GA, Bazylinski DA, Pan Y. 2018. Genomic expansion of magnetotactic bacteria reveals an early common origin of magnetotaxis with lineage-specific evolution. ISME J 12:1508–1519.

125. Lin W, Deng A, Wang Z, Li Y, Wen T, Wu L-F, Wu M, Pan Y. 2014. Genomic insights into the uncultured genus '*Candidatus* Magnetobacterium' in the phylum *Nitrospirae*. ISME J 8:2463–2477.

126. Sakaguchi T, Arakaki A, Matsunaga T. 2002. *Desulfovibrio magneticus* sp. nov., a novel sulfate-reducing bacterium that produces intracellular single-domain-sized magnetite particles. Int J Syst Evol Microbiol 52:215–221.

127. Sakaguchi T, Burgess JG, Matsunaga T. 1993. Magnetite formation by a sulphate-reducing bacterium. Nature 365:47–49.

128. Nakazawa H, Arakaki A, Narita-Yamada S, Yashiro I, Jinno K, Aoki N, Tsuruyama A, Okamura Y, Tanikawa S, Fujita N, Takeyama H, Matsunaga T. 2009. Whole genome sequence of *Desulfovibrio magneticus* strain RS-1 revealed common gene clusters in magnetotactic bacteria. Genome Res 19:1801–1808.

129. Barton LL, Fauque GD. 2009. Chapter 2 Biochemistry, Physiology and Biotechnology of Sulfate-Reducing Bacteria, p. 41–98. *In* Advances in Applied Microbiology. Academic Press.

130. Heidelberg JF, Seshadri R, Haveman SA, Hemme CL, Paulsen IT, Kolonay JF, Eisen JA, Ward N, Methe B, Brinkac LM, Daugherty SC, Deboy RT, Dodson RJ, Durkin AS, Madupu R, Nelson WC, Sullivan SA, Fouts D, Haft DH, Selengut J, Peterson JD, Davidsen TM, Zafar N, Zhou L, Radune D, Dimitrov G, Hance M, Tran K, Khouri H, Gill J, Utterback TR, Feldblyum TV, Wall JD, Voordouw G, Fraser CM. 2004. The genome sequence of the anaerobic, sulfate-reducing bacterium *Desulfovibrio vulgaris* Hildenborough. Nat Biotechnol 22:554–559.

131. Keller KL, Wall JD. 2011. Genetics and Molecular Biology of the Electron Flow for Sulfate Respiration in *Desulfovibrio*. Front Microbiol 2.

132. Wall JD, Hemme CL, Rapp-Giles B, Ringbauer JA, Casalot L, Giblin T. 2003. Genes and Genetic Manipulations of *Desulfovibrio*, p. 85–98. *In* Biochemistry and Physiology of Anaerobic Bacteria. Springer, New York, NY.

133. Broco Manuela, Rousset Marc, Oliveira Solange, Rodrigues-Pousada Claudina. 2005. Deletion of flavoredoxin gene in *Desulfovibrio gigas* reveals its participation in thiosulfate reduction. FEBS Lett 579:4803–4807.

134. Parks JM, Johs A, Podar M, Bridou R, Hurt RA, Smith SD, Tomanicek SJ, Qian Y, Brown SD, Brandt CC, Palumbo AV, Smith JC, Wall JD, Elias DA, Liang L. 2013. The Genetic Basis for Bacterial Mercury Methylation. Science 339:1332–1335.

135. Rousset M, Dermoun Z, Chippaux M, Bélaich JP. 1991. Marker exchange mutagenesis of the *hydN* genes in *Desulfovibrio fructosovorans*. Mol Microbiol 5:1735–1740.

136. Fu R, Voordouw G. 1997. Targeted gene-replacement mutagenesis of *dcrA*, encoding an oxygen sensor of the sulfate-reducing bacterium *Desulfovibrio vulgaris* Hildenborough. Microbiology 143:1815–1826.

137. Keller KL, Bender KS, Wall JD. 2009. Development of a Markerless Genetic Exchange System for *Desulfovibrio vulgaris* Hildenborough and Its Use in Generating a Strain with Increased Transformation Efficiency. Appl Environ Microbiol 75:7682–7691.

138. Gay P, Coq DL, Steinmetz M, Ferrari E, Hoch JA. 1983. Cloning structural gene *sacB*, which codes for exoenzyme levansucrase of *Bacillus subtilis*: expression of the gene in *Escherichia coli*. J Bacteriol 153:1424–1431.

139. Ried JL, Collmer A. 1987. An *nptI-sacB-sacR* cartridge for constructing directed, unmarked mutations in Gram-negative bacteria by marker exchange-eviction mutagenesis. Gene 57:239–246.

140. Neuhard J. 1983. Utilization of preformed pyrimidine bases and nucleosides / Utilization of preformed pyrimidine bases and nucleosides, p. 95–148. *In* Metabolism of nucleotides, nucleosides and nucleobases in microorganisms / edited by A. Munch-PetersenA. Munch-Petersen. Academic Press, New York, NY.

141. Singh V, Brecik M, Mukherjee R, Evans JC, Svetlíková Z, Blaško J, Surade S, Blackburn J, Warner DF, Mikušová K, Mizrahi V. 2015. The Complex Mechanism of Antimycobacterial Action of 5-Fluorouracil. Chem Biol 22:63–75.

142. Cohen SS, Flaks JG, Barner HD, Loeb MR, Lichtenstein J. 1958. The mode of action of 5-fluorouracil and its derivatives. Proc Natl Acad Sci U S A 44:1004–1012.

143. Bender KS, Cheyen H, Wall JD. 2006. Analysing the Metabolic Capabilities of *Desulfovibrio* Species through Genetic Manipulation. Biotechnol Genet Eng Rev 23:157–174.

144. Ruvkun GB, Ausubel FM. 1981. A general method for site-directed mutagenesis in prokaryotes. Nature 289:85–88.

145. Bloor AE, Cranenburgh RM. 2006. An Efficient Method of Selectable Marker Gene Excision by Xer Recombination for Gene Replacement in Bacterial Chromosomes. Appl Environ Microbiol 72:2520–2525.

146. Cai YP, Wolk CP. 1990. Use of a conditionally lethal gene in *Anabaena* sp. strain PCC 7120 to select for double recombinants and to entrap insertion sequences. J Bacteriol 172:3138–3145.

147. Kaniga K, Delor I, Cornelis GR. 1991. A wide-host-range suicide vector for improving reverse genetics in Gram-negative bacteria: inactivation of the *blaA* gene of *Yersinia enterocolitica*. Gene 109:137–141.

148. Ma W, Wang X, Mao Y, Wang Z, Chen T, Zhao X. 2015. Development of a markerless gene replacement system in *Corynebacterium glutamicum* using *upp* as a counter-selection marker. Biotechnol Lett 37:609–617.

149. Graf N, Altenbuchner J. 2011. Development of a Method for Markerless Gene Deletion in *Pseudomonas putida*. Appl Environ Microbiol 77:5549–5552.

150. Wang Y, Zhang C, Gong T, Zuo Z, Zhao F, Fan X, Yang C, Song C. 2015. An *upp*-based markerless gene replacement method for genome reduction and metabolic pathway engineering in *Pseudomonas mendocina* NK-01 and *Pseudomonas putida* KT2440. J Microbiol Methods 113:27–33.

151. Fabret C, Dusko Ehrlich S, Noirot P. 2002. A new mutation delivery system for genome-scale approaches in *Bacillus subtilis*. Mol Microbiol 46:25–36.

152. Huang LC, Wood EA, Cox MM. 1997. Convenient and reversible site-specific targeting of exogenous DNA into a bacterial chromosome by use of the FLP recombinase: the FLIRT system. J Bacteriol 179:6076–6083.

153. Chen AP, Berounsky VM, Chan MK, Blackford MG, Cady C, Moskowitz BM, Kraal P, Lima EA, Kopp RE, Lumpkin GR, Weiss BP, Hesse P, Vella NGF. 2014. Magnetic properties of uncultivated magnetotactic bacteria and their contribution to a stratified estuary iron cycle. Nat Commun 5:4797.

154. Lin W, Bazylinski DA, Xiao T, Wu L-F, Pan Y. 2014. Life with compass: diversity and biogeography of magnetotactic bacteria. Environ Microbiol 16:2646–2658.

155. Arakaki A, Takeyama H, Tanaka T, Matsunaga T. 2002. Cadmium recovery by a sulfate-reducing magnetotactic bacterium, *Desulfovibrio magneticus* RS-1, using magnetic separation. Appl Biochem Biotechnol 98–100:833–840.

156. Gibson DG, Young L, Chuang R-Y, Venter JC, Hutchison Iii CA, Smith HO. 2009. Enzymatic assembly of DNA molecules up to several hundred kilobases. Nat Methods 6:343–345.

157. Rousset M, Casalot L, Rapp-Giles BJ, Dermoun Z, de Philip P, Bélaich J-P, Wall JD. 1998. New Shuttle Vectors for the Introduction of Cloned DNA in *Desulfovibrio*. Plasmid 39:114–122.

158. Rae BD, Long BM, Badger MR, Price GD. 2013. Functions, Compositions, and Evolution of the Two Types of Carboxysomes: Polyhedral Microcompartments That Facilitate CO2 Fixation in Cyanobacteria and Some Proteobacteria. Microbiol Mol Biol Rev 77:357–379.

159. Grant CR, Wan J, Komeili A. 2018. Organelle Formation in Bacteria and Archaea. Annu Rev Cell Dev Biol 34:217–238.

160. Andrews SC. 1998. Iron Storage in Bacteria, p. 281–351. *In* Poole, RK (ed.), Advances in Microbial Physiology. Academic Press.

161. Touati D. 2000. Iron and Oxidative Stress in Bacteria. Arch Biochem Biophys 373:1–6.

162. Andrews SC, Robinson AK, Rodríguez-Quiñones F. 2003. Bacterial iron homeostasis. FEMS Microbiol Rev 27:215–237.

163. Grant CR, Rahn-Lee L, LeGault KN, Komeili A. 2018. Genome Editing Method for the Anaerobic Magnetotactic Bacterium *Desulfovibrio magneticus* RS-1. Appl Env Microbiol 84:e01724-18.

164. Smith AT, Smith KP, Rosenzweig AC. 2014. Diversity of the metal-transporting P_{1B}-type ATPases. J Biol Inorg Chem JBIC Publ Soc Biol Inorg Chem 19:947–960.

165. Argüello JM, González-Guerrero M, Raimunda D. 2011. Bacterial Transition Metal P_{1B}-ATPases, Transport Mechanism and Roles in Virulence. Biochemistry 50:9940–9949.

166. Russ WP, Engelman DM. 2000. The GxxxG motif: a framework for transmembrane helix-helix association. J Mol Biol 296:911–919.

167. Unterreitmeier S, Fuchs A, Schäffler T, Heym RG, Frishman D, Langosch D. 2007. Phenylalanine promotes interaction of transmembrane domains via GxxxG motifs. J Mol Biol 374:705–718.

168. Nudelman H, Lee Y-Z, Hung Y-L, Kolusheva S, Upcher A, Chen Y-C, Chen J-Y, Sue S-C, Zarivach R. 2018. Understanding the Biomineralization Role of Magnetite-Interacting Components (MICs) From Magnetotactic Bacteria. Front Microbiol 9.

169. VerBerkmoes NC, Shah MB, Lankford PK, Pelletier DA, Strader MB, Tabb DL, McDonald WH, Barton JW, Hurst GB, Hauser L, Davison BH, Beatty JT, Harwood CS, Tabita FR, Hettich RL, Larimer FW. 2006. Determination and Comparison of the Baseline Proteomes of the Versatile Microbe *Rhodopseudomonas palustris* under Its Major Metabolic States. J Proteome Res 5:287–298.

170. Kuehl JV, Price MN, Ray J, Wetmore KM, Esquivel Z, Kazakov AE, Nguyen M, Kuehn R, Davis RW, Hazen TC, Arkin AP, Deutschbauer A. 2014. Functional Genomics with a Comprehensive Library of Transposon Mutants for the Sulfate-Reducing Bacterium *Desulfovibrio alaskensis* G20. mBio 5:e01041-14.

171. Abdul-Tehrani H, Hudson AJ, Chang Y-S, Timms AR, Hawkins C, Williams JM, Harrison PM, Guest JR, Andrews SC. 1999. Ferritin Mutants of *Escherichia coli* Are Iron Deficient and Growth Impaired, and fur Mutants are Iron Deficient. J Bacteriol 181:1415–1428.

172. Ho TD, Ellermeier CD. 2015. Ferric Uptake Regulator Fur Control of Putative Iron Acquisition Systems in *Clostridium difficile*. J Bacteriol 197:2930–2940.

173. Bender KS, Yen H-CB, Hemme CL, Yang Z, He Z, He Q, Zhou J, Huang KH, Alm EJ, Hazen TC, Arkin AP, Wall JD. 2007. Analysis of a Ferric Uptake Regulator (Fur) Mutant of *Desulfovibrio vulgaris* Hildenborough. Appl Environ Microbiol 73:5389–5400.

174. Uebe R, Voigt B, Schweder T, Albrecht D, Katzmann E, Lang C, Böttger L, Matzanke B, Schüler D. 2010. Deletion of a fur-Like Gene Affects Iron Homeostasis and Magnetosome Formation in *Magnetospirillum gryphiswaldense*. J Bacteriol 192:4192–4204.

175. Wang Q, Wang X, Zhang W, Li X, Zhou Y, Li D, Wang Y, Tian J, Jiang W, Zhang Z, Peng Y, Wang L, Li Y, Li J. 2017. Physiological characteristics of *Magnetospirillum gryphiswaldense* MSR-1 that control cell growth under high-iron and low-oxygen conditions. Sci Rep 7:2800.

176. Pereira PM, He Q, Xavier AV, Zhou J, Pereira IAC, Louro RO. 2008. Transcriptional response of *Desulfovibrio vulgaris* Hildenborough to oxidative stress mimicking environmental conditions. Arch Microbiol 189:451–461.

177. Zhou A, He Z, Redding-Johanson AM, Mukhopadhyay A, Hemme CL, Joachimiak MP, Luo F, Deng Y, Bender KS, He Q, Keasling JD, Stahl DA, Fields MW, Hazen TC, Arkin AP, Wall JD, Zhou J. 2010. Hydrogen peroxide-induced oxidative stress responses in *Desulfovibrio vulgaris* Hildenborough. Environ Microbiol 12:2645–2657.

178. Caffrey SM, Voordouw G. 2010. Effect of sulfide on growth physiology and gene expression of *Desulfovibrio vulgaris* Hildenborough. Antonie Van Leeuwenhoek 97:11.

179. Luo Q, Groh JL, Ballard JD, Krumholz LR. 2007. Identification of Genes That Confer Sediment Fitness to *Desulfovibrio desulfuricans* G20. Appl Environ Microbiol 73:6305–6312.

180. Rey FE, Harwood CS. 2010. FixK, a global regulator of microaerobic growth, controls photosynthesis in *Rhodopseudomonas palustris*. Mol Microbiol 75:1007–1020.

181. Bose A, Newman DK. 2011. Regulation of the phototrophic iron oxidation (pio) genes in *Rhodopseudomonas palustris* TIE-1 is mediated by the global regulator, FixK. Mol Microbiol 79:63–75.

182. Blondeau M, Sachse M, Boulogne C, Gillet C, Guigner J-M, Skouri-Panet F, Poinsot M, Ferard C, Miot J, Benzerara K. 2018. Amorphous Calcium Carbonate Granules Form Within an Intracellular Compartment in Calcifying Cyanobacteria. Front Microbiol 9.

183. Benzerara K, Skouri-Panet F, Li J, Férard C, Gugger M, Laurent T, Couradeau E, Ragon M, Cosmidis J, Menguy N, Margaret-Oliver I, Tavera R, López-García P, Moreira D. 2014. Intracellular Ca-carbonate biomineralization is widespread in cyanobacteria. Proc Natl Acad Sci 111:10933–10938.

184. Kim M-K, Harwood CS. 1991. Regulation of benzoate-CoA ligase in *Rhodopseudomonas palustris*. FEMS Microbiol Lett 83:199–203.

185. Zane GM, Yen HB, Wall JD. 2010. Effect of the Deletion of *qmoABC* and the Promoter-Distal Gene Encoding a Hypothetical Protein on Sulfate Reduction in *Desulfovibrio vulgaris* Hildenborough. Appl Environ Microbiol 76:5500–5509.

186. Castresana J. 2000. Selection of conserved blocks from multiple alignments for their use in phylogenetic analysis. Mol Biol Evol 17:540–552.

187. Stamatakis A. 2014. RAxML version 8: a tool for phylogenetic analysis and post-analysis of large phylogenies. Bioinformatics 30:1312–1313.

188. Lefort V, Longueville J-E, Gascuel O. 2017. SMS: Smart Model Selection in PhyML. Mol Biol Evol 34:2422–2424.

189. Letunic I, Bork P. Interactive Tree Of Life (iTOL) v4: recent updates and new developments. Nucleic Acids Res.

190. Finn RD, Clements J, Eddy SR. 2011. HMMER web server: interactive sequence similarity searching. Nucleic Acids Res 39:W29–W37.

191. Eddy SR. 2011. Accelerated Profile HMM Searches. PLOS Comput Biol 7:e1002195.

192. Garcia PS, Jauffrit F, Grangeasse C, Brochier-Armanet C. 2019. GeneSpy, a user-friendly and flexible genomic context visualizer. Bioinforma Oxf Engl 35:329–331.

193. Bernsel A, Viklund H, Hennerdal A, Elofsson A. 2009. TOPCONS: consensus prediction of membrane protein topology. Nucleic Acids Res 37:W465-468.

194. Crooks GE. 2004. WebLogo: A Sequence Logo Generator. Genome Res 14:1188–1190.

195. Kumar S, Nei M, Dudley J, Tamura K. 2008. MEGA: A biologist-centric software for evolutionary analysis of DNA and protein sequences. Brief Bioinform 9:299–306.

196. Käll L, Krogh A, Sonnhammer ELL. 2004. A combined transmembrane topology and signal peptide prediction method. J Mol Biol 338:1027–1036.

197. Krogh A, Larsson B, von Heijne G, Sonnhammer EL. 2001. Predicting transmembrane protein topology with a hidden Markov model: application to complete genomes. J Mol Biol 305:567–580.

198. Rahn-Lee L, Komeili A. 2013. The magnetosome model: insights into the mechanisms of bacterial biomineralization. Front Microbiol 4.

199. Matsunaga T, Nemoto M, Arakaki A, Tanaka M. 2009. Proteomic analysis of irregular, bullet-shaped magnetosomes in the sulphate-reducing magnetotactic bacterium *Desulfovibrio magneticus* RS-1. Proteomics 9:3341–3352.

200. Jarsch IK, Daste F, Gallop JL. 2016. Membrane curvature in cell biology: An integration of molecular mechanisms. J Cell Biol 214:375–387.

201. Edwards AN, Fowlkes JD, Owens ET, Standaert RF, Pelletier DA, Hurst GB, Doktycz MJ, Morrell-Falvey JL. 2009. An *in vivo* imaging-based assay for detecting protein interactions over a wide range of binding affinities. Anal Biochem 395:166–177.